universität
wien

# DISSERTATION

Titel der Dissertation

## „Dynamic Processes on Rhodium Surfaces“

Verfasser

Mag. Thomas Franz

angestrebter akademischer Grad

Doktor der Naturwissenschaften (Dr. rer. nat.)

Wien, 2013

| | |
|---|---|
| Studienkennzahl lt. Studienblatt: | A 091 411 |
| Dissertationsgebiet lt. Studienblatt: | Physik |
| Betreuerin / Betreuer: | Univ.-Prof. Dipl.-Ing. Dr. Georg Kresse |

# Acknowledgements

I wish to thank Dr. Florian Mittendorfer for his supervision of my thesis.

I also thank Univ.-Prof. Dr. Georg Kresse for being very patient with me and allowing me to work in the Computational Materials Physics group for quite a long time.

I would like to give my special thanks to Michael Pöltl, who taught me a lot about working with Linux and Python programming. These skills became very valuable for my work.

Thanks must also go to Roman Wahl for teaching me a lot about the visualization of data with Xmgrace, which enabled me to create most of the diagrams in the present thesis. Furthermore, he helped me very much with his deep knowledge of LaTeX.

Concerning the chapter ”Free Energy Calculations for O/Rh(111)”, I am greatly indebted to Dr. Tomáš Bučko (Comenius University, Bratislava). Not only did he implement the algorithms necessary for the constrained Molecular Dynamics and metadynamics simulations in VASP, but he also explained the theoretical foundations to me very patiently and spent a lot of time answering my numerous questions.

Finally, I would like to thank all members of the Computational Materials Physics group who helped me with VASP-related or other issues.

# Abstract

In the framework of this thesis, the static and dynamic aspects of the interaction of metallic surfaces with simple adsorbates are investigated using complementary computational approaches. The simulations are performed on the basis of density functional theory (DFT) calculations using the Vienna Ab-initio Simulation Package (VASP).

In the first part of the thesis, we investigate the structure of a NiO surface oxide formed on Rh(111). Simulated annealing approaches allow to determine the complex structure, and to identify a $Ni_5O_5$ stoichiometry. The structure is verified using STM simulations performed in the Tersoff-Hamann approximation, which are compared with experimental STM images. The thermodynamic stability of the $Ni_5O_5$ structure is evaluated by calculating the Gibbs free energies of several competing phases.

In the following part, we investigate the catalytic activity of quasi-one-dimensional nickel oxide nanowires, which can be grown at the step edges of the Rh(553) surface, with respect to the oxidation of carbon monoxide and the subsequent desorption of carbon dioxide. We apply the nudged elastic band method, the dimer method, and quasi-Newton algorithms in order to identify reaction paths. Furthermore, we calculate prefactors and reaction rate constants in the framework of transition state theory.

The next chapter is dedicated to the implementation of kinetic Monte Carlo algorithms on the basis of DFT calculations. We evaluate temperature programmed desorption (TPD) spectra of oxygen on Rh(111) and thereby simulate the time evolution of a system with multiple competing reactions on a macroscopic timescale. A multi-site lattice gas model is used, and cross validation is applied to construct an effective Hamiltonian for the lateral interactions. The calculated TPD spectra are compared with experimental spectra.

The last part of the thesis discusses the explicit evaluation of the entropic effects for surface reactions. We use thermodynamic integration of free energy gradients to compute the free energy differences of diffusion and of desorption of O/Rh(111), where the gradients are determined via constrained Molecular Dynamics simulations. Free energy perturbation is applied in order to enhance the numerical accuracy of the results. These results are compared with free energy differences obtained from a simple harmonic ap-

proximation.

# Zusammenfassung

Im Rahmen dieser Dissertation werden die statischen und dynamischen Aspekte der Wechselwirkungen zwischen Metalloberflächen und einfachen Adsorbaten untersucht, wobei mehrere komplementäre Methoden verwendet werden. Die Simulationen werden auf Basis der Dichtefunktionaltheorie mit Hilfe des Vienna Ab-initio Simulation Package (VASP) durchgeführt.

Im ersten Teil dieser Arbeit untersuchen wir die Struktur eines NiO Oberflächenoxids auf Rh(111). Mittels Simulated Annealing wird die komplexe Struktur bestimmt, deren Stöchiometrie sich als $Ni_5O_5$ herausstellt. Durch Vergleich von STM-Simulationen im Tersoff-Hamann-Ansatz mit experimentellen STM-Bildern wird die gefundene Struktur bestätigt. Die thermodynamische Stabilität dieser $Ni_5O_5$-Phase wird durch Berechnung der Gibbsschen freien Energie verschiedener konkurrierender Phasen ermittelt.

Im darauf folgenden Teil beschäftigen wir uns mit der katalytischen Aktivität von quasi-eindimensionalen Nickel-Oxid-Nanostreifen, die an den Stufen der Rh(553)-Oberfläche erzeugt werden können, bezüglich der Oxidation von Kohlenmonoxid und der anschließenden Desorption von Kohlendioxid. Wir verwenden die Nudged Elastic Band-Methode, die Dimer-Methode, sowie Quasi-Newton-Algorithmen, um Reaktionspfade zu bestimmen. Weiters werden Präfaktoren und Reaktionsraten im Rahmen der Transition State Theory berechnet.

Das nächste Kapitel widmet sich der Implementierung von Kinetic Monte Carlo-Algorithmen. Wir berechnen Temperatur-programmierte Desorptionsspektren (TPD-Spektren) von Sauerstoff auf Rh(111) und simulieren damit die Zeitentwicklung eines Systems mit vielen konkurrierenden Reaktionen auf einer makroskopischen Zeitskala. Ein Gittergasmodell wird verwendet, wobei mit Hilfe von Cross Validation ein effektiver Hamilton-Operator bestimmt wird. Die simulierten TPD-Spektren werden mit experimentellen Spektren verglichen.

Im letzten Teil dieser Dissertation wird die explizite Berücksichtigung von entropischen Effekten für Oberflächenreaktionen behandelt. Wir verwenden thermodynamische Integration von Gradienten der freien Energie, um Freie-Energie-Differenzen für die Diffusion und die Desorption von Sauerstoff auf Rh(111) zu berechnen. Die Gradienten werden dabei mittels Molekulardynamik mit Zwangsbedingungen ermittelt. Durch eine störungstheoretische

Behandlung wird die numerische Genauigkeit der Ergebnisse verbessert. Diese Ergebnisse werden mit Freie-Energie-Differenzen, die aus einem einfachen harmonischen Ansatz resultieren, verglichen.

# Contents

**1 Density Functional Theory 1**

1.1 Overview . . . . . 1
1.2 Hohenberg-Kohn Theorem . . . . . 3
1.3 Kohn-Sham Equations . . . . . 4
1.4 Self-Consistency Cycle . . . . . 5
1.5 Local Density Approximation . . . . . 5
1.6 Generalized Gradient Approximations . . . . . 5
1.7 Calculation of Forces acting on Ions . . . . . 6

**2 NiO on Rh(111) 7**

2.1 Introduction . . . . . 7
2.2 Structure Search and STM Simulation . . . . . 8
2.3 Vibrational Spectrum . . . . . 11
2.4 Thermodynamic Stability . . . . . 11
2.5 Summary . . . . . 15

**3 CO on $NiO_2$-Rh(553) 17**

3.1 Introduction . . . . . 17
3.2 Methods . . . . . 18
  3.2.1 Rare Events and Transition States . . . . . 18
  3.2.2 Nudged Elastic Band . . . . . 19
  3.2.3 Dimer Method . . . . . 21
  3.2.4 Quasi-Newton Algorithms . . . . . 21
  3.2.5 Verification of Transition States . . . . . 22
  3.2.6 Transition State Theory . . . . . 23
3.3 Results . . . . . 27
  3.3.1 Computational Setup . . . . . 27
  3.3.2 Reference Structures . . . . . 28
  3.3.3 Oxidation of CO on Rh(111) . . . . . 29
  3.3.4 Oxidation of CO on $NiO_2$/Rh(553) . . . . . 29
  3.3.5 Oxidation of CO on bare Rh(553) . . . . . 37
  3.3.6 Reaction Rate Constants . . . . . 39
3.4 Summary . . . . . 42

**4 Kinetic Monte Carlo Simulations of Temperature Programed Desorption of O/Rh(111) 45**
4.1 Introduction . . . . . . . . . . . . . . . . . . . . . . . . . . . . 45
4.2 Kinetic Monte Carlo . . . . . . . . . . . . . . . . . . . . . . . 46
4.3 Desorption Processes of Oxygen on Rh(111) . . . . . . . . . . 47
4.4 Diffusion Events . . . . . . . . . . . . . . . . . . . . . . . . . 51
4.5 Lattice Gas Model . . . . . . . . . . . . . . . . . . . . . . . . 52
4.6 Parametrization . . . . . . . . . . . . . . . . . . . . . . . . . . 54
  4.6.1 Lattice Gas Hamiltonian . . . . . . . . . . . . . . . . . 54
  4.6.2 Cross Validation . . . . . . . . . . . . . . . . . . . . . . 57
  4.6.3 Inclusion of Unoccupied Sites . . . . . . . . . . . . . . 59
  4.6.4 Parametrization with Pair Interactions only . . . . . . 63
4.7 TPD Spectra . . . . . . . . . . . . . . . . . . . . . . . . . . . 63
4.8 Summary . . . . . . . . . . . . . . . . . . . . . . . . . . . . . 70

**5 Free Energy Calculations for O/Rh(111) 73**
5.1 Introduction . . . . . . . . . . . . . . . . . . . . . . . . . . . . 73
5.2 Thermodynamic Integration . . . . . . . . . . . . . . . . . . . 74
5.3 Diffusion of Oxygen on Rh(111) . . . . . . . . . . . . . . . . . 79
  5.3.1 Free Energy Differences of Diffusion from Thermodynamic Integration . . . . . . . . . . . . . . . . . . . . 79
  5.3.2 Free Energy Differences of Diffusion from a Harmonic Approximation . . . . . . . . . . . . . . . . . . . . . . 86
5.4 Desorption of Oxygen from Rh(111) . . . . . . . . . . . . . . 88
  5.4.1 Free Energy Differences of Desorption from Thermodynamic Integration . . . . . . . . . . . . . . . . . . . 88
  5.4.2 Corrections from Free Energy Perturbation . . . . . . 97
  5.4.3 Free Energy Differences of Desorption from a Harmonic Approximation . . . . . . . . . . . . . . . . . . 101
5.5 Summary . . . . . . . . . . . . . . . . . . . . . . . . . . . . . 102

**6 Summary 105**

**A Proofs of Density Functional Theory 107**
A.1 Hohenberg-Kohn Theorem . . . . . . . . . . . . . . . . . . . . 107
A.2 Derivation of the Kohn-Sham Equations . . . . . . . . . . . . 108
A.3 Total Energy in DFT . . . . . . . . . . . . . . . . . . . . . . . 111
A.4 Hellmann-Feynman Theorem . . . . . . . . . . . . . . . . . . . 113

**B Cross Validation: Input and Output 115**
B.1 Input Configurations . . . . . . . . . . . . . . . . . . . . . . . 115
  B.1.1 $(1 \times 1)$ Surface Cells . . . . . . . . . . . . . . . . . . 115
  B.1.2 $(2 \times 2)$ Surface Cells . . . . . . . . . . . . . . . . . . 116
  B.1.3 $(3 \times 3)$ Surface Cells . . . . . . . . . . . . . . . . . . 116

B.1.4 $(4 \times 4)$ Surface Cells . . . . . . . . . . . . . . . . . . . 117
B.1.5 $(6 \times 6)$ Surface Cells . . . . . . . . . . . . . . . . . . . 118
B.1.6 $(8 \times 8)$ Surface Cells . . . . . . . . . . . . . . . . . . . 120
B.2 Output: Effective Interaction Parameters . . . . . . . . . . . 121
B.2.1 Two-body Figures . . . . . . . . . . . . . . . . . . . . 121
B.2.2 Three-body Figures . . . . . . . . . . . . . . . . . . . 122
B.2.3 Four-body Figures . . . . . . . . . . . . . . . . . . . . 123
B.2.4 Figures including Unoccupied Sites . . . . . . . . . . . 123

**List of publications** **133**

**Talks** **135**

**Poster presentations** **137**

**Curriculum vitae** **139**

# Chapter 1

# Density Functional Theory

In the framework of this thesis the simulations were performed on the basis of density functional theory (DFT) calculations using the Vienna Ab-initio Simulation Package (VASP) [1, 2]. For this reason, a basic introduction to DFT is given in this chapter. Selected proofs can be found in Appendix A. For more detailed introductions see, for example, [3, 4, 5, 6, 7].

## 1.1 Overview

In solid state physics, one is often interested in calculating the energy of a system consisting of $M$ nuclei and $N$ electrons in the quantum mechanical ground state. To obtain this energy, the solution of the Schrödinger equation for the wave function

$$\psi = \psi(\mathbf{R}_1, \ldots, \mathbf{R}_M, \mathbf{r}_1, \ldots, \mathbf{r}_N)\,, \tag{1.1}$$

is required, where $\mathbf{R}_1, \ldots, \mathbf{R}_M$ and $\mathbf{r}_1, \ldots, \mathbf{r}_N$ are respectively the coordinates of the nuclei and the electrons. However, with an exact many-particle Hamiltonian the Schrödinger equation for this wave function is not solvable exactly for systems that are of interest in solid state physics, and approximations are inevitable.

Energy calculations of systems comprising nuclei as well as electrons are usually carried out in the Born-Oppenheimer approximation, which is based on the assumption that the electrons move much faster than the nuclei and follow any movement of the latter instantaneously. This assumption is justified if the mass of a nucleus is much larger than the mass of an electron. The wave function of the overall system can then be written as a product of a nuclear and an electronic wave function,

$$\psi(\mathbf{R}_1, \ldots, \mathbf{R}_M, \mathbf{r}_1, \ldots, \mathbf{r}_N) = \varphi(\mathbf{r}_1, \ldots, \mathbf{r}_N | \mathbf{R}_1, \ldots, \mathbf{R}_M)\, \chi(\mathbf{R}_1, \ldots, \mathbf{R}_M)\,,$$

where $\varphi(\mathbf{r}_1, \ldots, \mathbf{r}_N | \mathbf{R}_1, \ldots, \mathbf{R}_M)$ is the electronic wave function at fixed nuclear coordinates $\mathbf{R}_1, \ldots, \mathbf{R}_M$, and $\chi(\mathbf{R}_1, \ldots, \mathbf{R}_M)$ is the nuclear wave function.

The quantum mechanical calculations for the electrons are performed for a fixed geometry of the nuclei. Furthermore the nuclei, due to their comparatively large mass, can be treated as classical particles. For the respective nuclear geometry, the electronic wave function needs to be determined from a Schrödinger equation for the electronic subsystem, where the Coulomb potential resulting from the nuclear coordinates enters the Hamiltonian as an external potential. In atomic units, this Hamiltonian for the electronic subsystem is

$$H = -\sum_{i=1}^{N} \frac{1}{2} \Delta_{\mathbf{r}_i} + \sum_{i<j}^{N} \frac{1}{|\mathbf{r}_i - \mathbf{r}_j|} - \sum_{i=1}^{N} \sum_{k=1}^{M} \frac{Z_k}{|\mathbf{r}_i - \mathbf{R}_k|}\,, \tag{1.2}$$

where the left term describes the kinetic energy of the electrons, the middle term describes the Coulomb interaction between the electrons, and the term on the right hand side represents the Coulomb interaction between electrons and nuclei, where $Z_k$ is the atomic number of nucleus $k$.

Any change in the nuclear geometry requires a reevaluation of the electronic Schrödinger equation. However, even if only the electrons are treated in the framework of quantum mechanics, the Schrödinger equation can in general not be solved exactly. The great importance of DFT is based on the fact that in this theory it is not necessary to solve the exact many-electron Schrödinger equation for the wave function $\varphi(\mathbf{r}_1, \ldots, \mathbf{r}_N | \mathbf{R}_1, \ldots, \mathbf{R}_M)$. In DFT, the problem is reduced to the determination of one-electron wave functions (orbitals), which are all solutions of the same one-electron Schrödinger equation.

DFT is based on the Hohenberg-Kohn theorem (section 1.2), from which it follows that the electron density of a many-electron system uniquely defines the wave function, the Hamiltonian and the ground state energy. Accordingly the electron density $n(\mathbf{r})$ is evaluated in the ground state. This allows for the subsequent calculation of the energy of the electronic system. Introducing one-electron wave functions $\{\phi_i\}$ and the so-called exchange-correlation energy $E_{xc}$, it is possible to calculate $n(\mathbf{r})$ by solving self-consistently the Kohn-Sham equations (section 1.3), where every orbital $\phi_i$ is an eigenfunction of the Hamiltonian with eigenvalue $\varepsilon_i$. With $n(\mathbf{r})$ and the Kohn-Sham eigenvalues $\{\varepsilon_i\}$ the total energy of the electronic system is calculated as

$$\begin{aligned} E_{\mathrm{DFT}} &= \sum_{i=1}^{N} \varepsilon_i - \frac{1}{2} \int\!\!\int \frac{n(\mathbf{r})\, n(\mathbf{r}')}{|\mathbf{r} - \mathbf{r}'|}\, \mathrm{d}\mathbf{r}\, \mathrm{d}\mathbf{r}' \\ &\quad - \int V_{xc}(\mathbf{r})\, n(\mathbf{r})\, \mathrm{d}\mathbf{r} + \int \varepsilon_{xc}(n(\mathbf{r}))\, n(\mathbf{r})\, \mathrm{d}\mathbf{r}\,. \end{aligned} \tag{1.3}$$

$V_{xc}(\mathbf{r})$ designates the exchange-correlation potential and $\varepsilon_{xc}(n(\mathbf{r}))$ is the exchange-correlation energy per electron in a homogeneous electron gas. In

Appendix A.3 it is shown why the total energy is not simply the sum of the Kohn-Sham eigenvalues but is of the form (1.3).

The exact form of the energy as a function of the electron density is unknown. The necessary approximations are restricted to the exchange-correlation energy $E_{xc}$. The simplest approximation is the so-called local density approximation (section 1.5). In the following sections, DFT is presented in more detail.

## 1.2 Hohenberg-Kohn Theorem

The Hohenberg-Kohn theorem [3] states that in the ground state of a many-electron system there exists exactly one external potential $V_{\mathrm{ext}}(\mathbf{r})$ that results in the exact many-electron density $n(\mathbf{r})$. Consequently, if $n(\mathbf{r})$ of the ground state is known, one can uniquely deduce $V_{\mathrm{ext}}(\mathbf{r})$. Thereby $n(\mathbf{r})$ also uniquely determines the many-electron Hamiltonian and the many-electron wave function. Hence the wave function $\psi_G$ of a many-electron system in its ground state is a functional $\psi_G[n(\mathbf{r})]$ of the electron density $n(\mathbf{r})$.

The energy of the system is a functional of the wave function. If this wave function is normalized, the energy is calculated as

$$E[\psi] = \langle\psi|H|\psi\rangle \,.$$

This functional has a minimum for the wave function of the ground state $\psi_G$, where it takes the value of the ground state energy $E_G$:

$$E_G = E[\psi_G] = \langle\psi_G|H|\psi_G\rangle < \langle\psi|H|\psi\rangle \quad \text{for } \psi \neq \psi_G \,. \tag{1.4}$$

Since the electron density $n(\mathbf{r})$ is related to exactly one wave function $\psi[n(\mathbf{r})]$, the energy can also be written as a functional of $n(\mathbf{r})$:

$$E[n(\mathbf{r})] = \langle\psi[n(\mathbf{r})]|H|\psi[n(\mathbf{r})]\rangle \,.$$

The functional $E[n(\mathbf{r})]$ is minimal for the electron density of the ground state $n_G(\mathbf{r})$, because the latter originates the wave function of the ground state $\psi_G$ for which equation (1.4) holds. This means that if the functional $E[n(\mathbf{r})]$ were known, wave functions would no longer be needed for the calculation of energies of many-electron systems, but one could compute the ground state energy (and in principle all other properties of the ground state) from the electron density $n(\mathbf{r})$ alone. Unfortunately the exact form of this functional is unknown. Hence one tries to find good approximations for $E[n(\mathbf{r})]$.

## 1.3 Kohn-Sham Equations

Kohn and Sham suggested for the energy functional the form [4]

$$\begin{aligned} E[\{\phi_i\}] \;&=\; -\sum_i \int \phi_i^*(\mathbf{r})\,\frac{1}{2}\Delta\;\phi_i(\mathbf{r})\;\mathrm{d}\mathbf{r} + \int V_{\mathrm{ext}}(\mathbf{r})\,n(\mathbf{r})\,\mathrm{d}\mathbf{r} \\ &\quad + \frac{1}{2}\int\!\!\int \frac{n(\mathbf{r})\,n(\mathbf{r}')}{|\mathbf{r}-\mathbf{r}'|}\,\mathrm{d}\mathbf{r}\,\mathrm{d}\mathbf{r}' + E_{xc}[n]\,, \end{aligned} \tag{1.5}$$

where the $\{\phi_i\}$ are one-electron wave functions of non interacting electrons. The energy is now a functional of these wave functions. The electron density at $\mathbf{r}$ is calculated from the lowest $N$ one-electron wave functions as

$$n(\mathbf{r}) \;=\; \sum_{i=1}^{N} \phi_i^*(\mathbf{r})\,\phi_i(\mathbf{r})\,. \tag{1.6}$$

Minimization of the Kohn-Sham energy functional $E[\{\phi_i\}]$ with respect to the one-electron wave functions $\phi_i^*$, with the constraint of all wave functions to be normalized, yields the Kohn-Sham equations

$$\left\{-\frac{1}{2}\Delta + V_{\mathrm{ext}}(\mathbf{r}) + \int \frac{n(\mathbf{r}')}{|\mathbf{r}-\mathbf{r}'|}\,\mathrm{d}\mathbf{r}' + V_{xc}(\mathbf{r})\right\}\phi_j(\mathbf{r}) \;=\; \varepsilon_j\,\phi_j(\mathbf{r})\,. \tag{1.7}$$

The derivation of these equations is shown in Appendix A.2. For the exchange-correlation potential we have

$$V_{xc}(\mathbf{r}) \;=\; \frac{\delta E_{xc}[n(\mathbf{r})]}{\delta n(\mathbf{r})}\,. \tag{1.8}$$

In the framework of DFT, it is attempted to find good approximations for the exchange-correlation energy $E_{xc}[n]$. This functional contains corrections for the total kinetic energy as well as for the energy due to the electrostatic interaction of the electrons. However, the functional $E_{xc}[n]$ is unknown. Still equation (1.5) is of practical use, since $E_{xc}[n]$ is in general much smaller than the other energy contributions [7]. Therefore it is possible to obtain useful results for $E[\{\phi_i\}]$ by applying relatively simple approximations. If $E_{xc}[n]$ were known exactly, the functional derivative (1.8) would yield a potential which would include all effects of exchange and correlation in an exact way. The averaged electrostatic repulsion between the electrons is in (1.7) described by the Hartree potential

$$V_H(\mathbf{r}) \;=\; \int \frac{n(\mathbf{r}')}{|\mathbf{r}-\mathbf{r}'|}\,\mathrm{d}\mathbf{r}'.$$

The Kohn-Sham equations represent a mapping of a system of interacting electrons onto a system of non interacting electrons, where each electron moves in an effective potential

$$V_{\mathrm{eff}}(\mathbf{r}) \;=\; V_{\mathrm{ext}}(\mathbf{r}) + \int \frac{n(\mathbf{r}')}{|\mathbf{r}-\mathbf{r}'|}\,\mathrm{d}\mathbf{r}' + V_{xc}(\mathbf{r}), \tag{1.9}$$

which is generated by all the other electrons and the ions.

## 1.4 Self-Consistency Cycle

The electron density $n(\mathbf{r})$ is calculated from the solutions $\{\phi_i\}$ of the Kohn-Sham equations via (1.6). However, $n(\mathbf{r})$ appears in the effective potential (1.9). Hence $n(\mathbf{r})$ is needed in order to compute the orbitals $\{\phi_i\}$ via the Kohn-Sham equations (1.7), on the other hand the solutions $\{\phi_i\}$ are needed in order to compute $n(\mathbf{r})$. Consequently the equations (1.7) have to be solved iteratively. Using an electron density $n_1^{\mathrm{in}}(\mathbf{r})$ one obtains orbitals and an electron density $n_1^{\mathrm{out}}(\mathbf{r})$. The densities $n_1^{\mathrm{in}}(\mathbf{r})$ and $n_1^{\mathrm{out}}(\mathbf{r})$ are then merged to a new density $n_2^{\mathrm{in}}(\mathbf{r})$, for which the equations are solved anew. This procedure is repeated several times. In the simplest case, we have for the electron densities of iterations $j$ and $j+1$:

$$n_{j+1}^{\mathrm{in}}(\mathbf{r}) \;=\; \alpha\, n_j^{\mathrm{out}}(\mathbf{r}) + (1-\alpha)\, n_j^{\mathrm{in}}(\mathbf{r})\,, \quad \alpha \,\epsilon\, [0,1]. \tag{1.10}$$

The self-consistency cycle is aborted, if a self-consistent solution is found, i.e. if $n_j^{\mathrm{out}}(\mathbf{r})$ and $n_j^{\mathrm{in}}(\mathbf{r})$ agree within a preselected tolerance.

## 1.5 Local Density Approximation

The simplest approximation for the exchange-correlation energy $E_{xc}$ is the local density approximation (LDA). In this approximation it is assumed that in a many-electron system with electron density $n(\mathbf{r})$, the exchange-correlation energy per electron at $\mathbf{r}'$ is equal to the exchange-correlation energy per electron in a homogeneous electron gas with density $n(\mathbf{r}')$. Let the latter be $\varepsilon_{xc}(n(\mathbf{r}'))$. The total exchange-correlation energy of an inhomogeneous system with electron density $n(\mathbf{r})$ is, in the LDA, given by

$$E_{xc}^{\mathrm{LDA}}[n(\mathbf{r})] \;=\; \int \varepsilon_{xc}(n(\mathbf{r}'))\, n(\mathbf{r}')\, \mathrm{d}\mathbf{r}'. \tag{1.11}$$

The function $\varepsilon_{xc}(n)$ is known from Monte Carlo simulations carried out for the homogeneous electron gas. In the LDA, the exchange-correlation potential is

$$V_{xc}(\mathbf{r}) \;=\; \frac{\delta E_{xc}[n(\mathbf{r})]}{\delta n(\mathbf{r})} \;=\; \frac{\partial\,[n(\mathbf{r})\,\varepsilon_{xc}(n(\mathbf{r}))]}{\partial\, n(\mathbf{r})}. \tag{1.12}$$

## 1.6 Generalized Gradient Approximations

In general, better approximations for the exchange-correlation energy $E_{xc}$ than the LDA can be found by taking not only the electron density at $\mathbf{r}'$, but also its derivative into account, which is given by the gradient $\nabla n(\mathbf{r}')$. Approximations for the exchange-correlation energy of the form

$$E_{xc}^{\mathrm{GGA}}[n(\mathbf{r})] \;=\; \int f(n(\mathbf{r}'), \nabla n(\mathbf{r}'))\, n(\mathbf{r}')\, \mathrm{d}\mathbf{r}' \tag{1.13}$$

are called generalized gradient approximations (GGA). There are many different GGA functionals differing in the choice of the function $f$. One particular and important GGA functional is the PBE functional, which is named after Perdew, Burke, and Ernzerhof, who have invented it in 1996 [8]. In the framework of the present thesis, all calculations with VASP have been performed using the PBE functional.

## 1.7 Calculation of Forces acting on Ions

The forces acting on the ions are computed by means of the Hellmann-Feynman theorem, which states that the force acting on ion $I$ is given only by the partial derivative of the energy $E$ with respect to the coordinates of the ion:

$$\mathbf{F}_I = -\frac{\mathrm{d}E}{\mathrm{d}\mathbf{R}_I} = -\frac{\partial E}{\partial \mathbf{R}_I}. \tag{1.14}$$

This in not self-evident since in principle also derivatives of the electronic orbitals contribute to the force. The derivation of the Hellmann-Feynman theorem is shown in Appendix A.4.

# Chapter 2

# NiO on Rh(111)

In this chapter, which closely follows our publication

T. Franz, J. Zabloudil, F. Mittendorfer, L. Gragnaniello, G. Parteder, F. Allegretti, S. Surnev, F. P. Netzer, *Deformed Surface Oxides: Uncommon Structure of a (6×1) NiO Surface Oxide on Rh(111)*, J. Phys. Chem. Lett. 3, 186 (2012),

we investigate the formation of a (6×1) NiO monolayer supported on a Rh(111) single-crystal surface. The theoretical methods employed comprise simulated annealing, simulation of STM images, calculation of vibrational spectra, and investigation of thermodynamic stability via computation of Gibbs free energies. This work was done in collaboration with our colleagues from Karl-Franzens University Graz who performed the experiments. For experimental details we refer to our abovementioned paper.

## 2.1 Introduction

The structure of an oxide surface, such as NiO, can be rather complex. Due to the rocksalt (NaCl) bulk structure of nickel oxide, the crystal can display both nonpolar surfaces such as NiO(100), with no macroscopic dipole moment, and also polar surfaces such as NiO(111). In the case of a polar surface, the resulting polar instability has to be compensated for by either structural or electronic modifications. An overview of the dominant compensating mechanisms can be found in Ref. [9]. In the case of the polar NiO(111) surface, surface X-ray diffraction experiments [10, 11] indicate a compensation by the formation of a p(2×2) octopolar reconstruction.
If the oxide surface is not the termination of the NiO bulk structure but is present as an ultrathin layer (with a thickness of only a few nanometers) supported on a single-crystal metal substrate, the structural and electronic flexibility at the interface allows for the presence of new phases that would be unstable in the thick-film limit. Moreover, such surface oxide structures

are determined not only by polarity considerations but also by the strain induced by the lattice mismatch between the metallic substrate material and the (bulk) nickel oxide. In particular, fcc (111) surfaces offer an interesting playground as the lattice symmetry of the substrate favors a polar (111) termination while the polarity considerations usually predict a lower surface energy for the nonpolar (100) bulk terminations. In addition, low dimensionality aspects of the supported Ni oxide structures have to be considered and may give rise to different physical behavior [12, 13].
Some of the experimental results, for which the aim of this work was to find a theoretical model, are shown in Fig. 2.1. Oxidation of submonolayer Ni films at an oxygen pressure of $5 \times 10^{-8}$ mbar induces the formation of islands exhibiting a (6×1) structure (Fig. 2.1 (a)). These islands grow in size with increasing Ni coverage and eventually form a wetting layer at 1 ML (Fig. 2.1 (b)). The atomically resolved STM image (Fig. 2.1 (c)) shows that the (6×1) structure displays zigzag ridges aligned pseudomorphically along the $\langle 110 \rangle$ substrate directions, which are separated by 6 Rh lattice constants, yielding the (6×1) periodicity (the unit cell is indicated in the image). Between the ridges, hexagonally ordered areas are visible. Occasionally, other periodicities like (4×1) and (2×1) have also been observed in STM, but the (6×1) is the dominant structure on the large scale, as confirmed by the LEED pattern (Fig. 2.1 (d)). Two-dimensional Ni oxide structures with a (6×1) and (2×1) periodicity have also been observed previously on a stepped Rh(15 15 13) surface in the monolayer coverage range [14], but no structural models have been proposed yet. Ni oxide layers with a (7×1) structure, grown on a Pt(111) surface under similar preparation conditions [15], show a very similar appearance in the STM images as the (6×1) phase. This structural similarity indicates that the (6×1) Ni oxide phase is not specific for a given oxide-metal interface but rather derives its stability from polarity cancellation and/or low surface energy effects, as discussed below.

## 2.2 Structure Search and STM Simulation

To find the structure of lowest total energy at fixed stoichiometry, we applied a *simulated annealing* approach [16]. Using Molecular Dynamics with a Nosé thermostat, the system was brought to thermodynamic equilibrium at 2200 K, and subsequently, in a simulation time of 38 ps using a time step of 2 fs, annealed to 300 K. Temperature was decreased linearly by 0.05 K per fs. In order to save computational time, simulated annealing was performed non spin polarized with a rhodium slab consisting of three layers, and a cutoff energy of 311 eV. Brillouin zone integration was performed using a Gamma-centered (6×6×1) mesh in the primitive (1×1) surface cell. Optimization of the most promising structures at zero temperature was accomplished using a *damped molecular dynamics* algorithm and modelling the

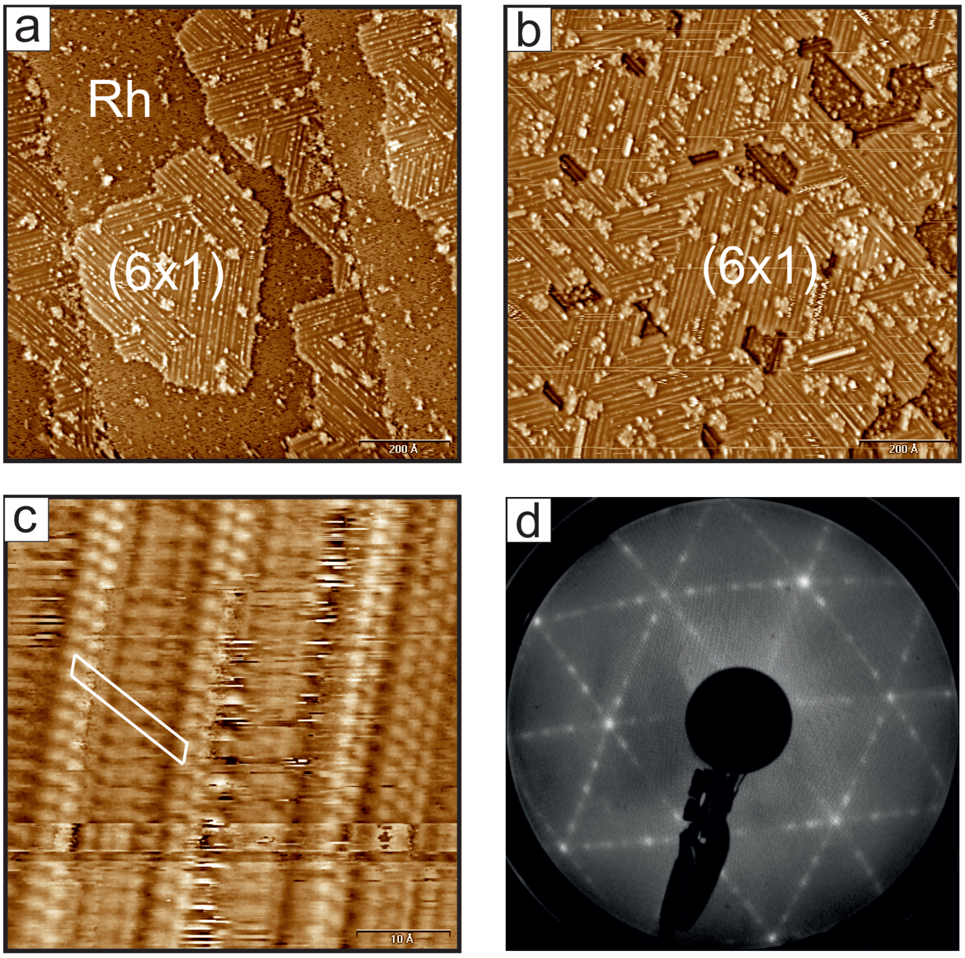

Figure 2.1: Large-scale (1000 Å × 1000 Å, +1.0 V, 0.2 nA) STM images of the (6×1) structure of NiO on Rh(111) at a coverage of (a) 0.5 ML and (b) 1 ML; (c) high-resolution STM image (50 Å × 50 Å, +8 mV, 1.5 nA) revealing details of the (6×1) structure; (d) LEED image ($E_p = 150$ eV).

surface with six rhodium layers, allowing for relaxation of the uppermost three layers. The cutoff energy in these spin polarized calculations was increased to 415 eV, and the Brillouin zone was integrated using a (24×24×1) mesh in the primitive (1×1) surface cell. Finally, STM simulations were performed in a Tersoff-Hamann approach [17] for the charge distribution between the Fermi energy and ±0.2 eV, where the cutoff energy was further increased to 540 eV.

The structure with the most satisfactorily agreement between simulated and experimental STM images is shown in Fig. 2.2 (a), (b). Although this structure consists formally of a single NiO monolayer with a $Ni_5O_5$ stoichiometry, it displays a sizable corrugation of 1.2 Å. The simulated STM images

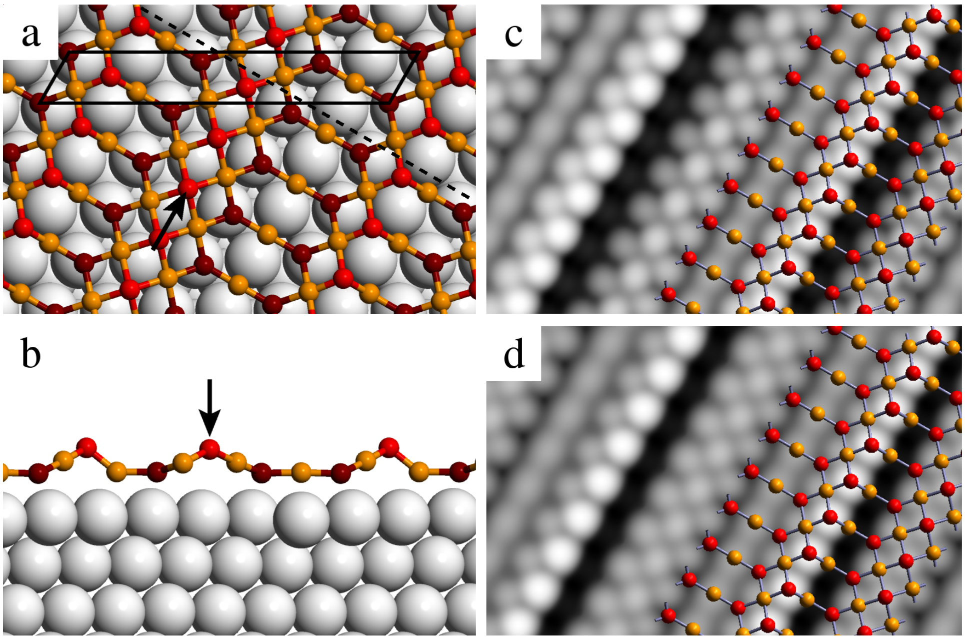

Figure 2.2: (a) Top view and (b) side view of the structural model for the (6×1) $Ni_5O_5$ structure. Ni (Rh) atoms are shown in orange (gray), lower O atoms are in dark red, and higher O atoms are in bright red. The cutting plane for (b) is indicated as a black dashed line in (a). Tersoff-Hamann simulation of the STM images (energy range ±0.2 eV around the Fermi level) for the (c) occupied and (d) unoccupied states.

(Fig. 2.2 (c), (d)) display bright stripes, separated by (electronically) lower regions, in good agreement with the experimental data. The deep minima in the simulations are less pronounced in the experimental images, but we attribute this deviation to smearing and convolution effects originating from the final size of the STM tip.

A closer look at the $Ni_5O_5$ structure reveals two types of building blocks, one triangular unit with a three-fold coordinated oxygen atom and a rectangular unit with a four-fold coordinated oxygen. Both elements are closely related to selected surface orientations of the NiO (rocksalt) bulk crystal, corresponding to the (100) orientation (four-fold O) and to the (111) orientation (three-fold O), respectively. Indeed, flat monolayers corresponding to these two orientations have been observed for related surface oxides, such as CoO/Pd(100) [18] or $RhO_2$/Rh(111) [22]. The structure of the full oxide layer shows a clear correlation between the local building block and the interaction with the Rh(111) substrate. On the one hand, the three lower-lying oxygen atoms (Fig. 2.2 (b)) are positioned on top of the substrate Rh atoms (with an O-Rh distance of 2.1Å) and thus anchor the NiO layer to the Rh surface. On the other hand, the two higher O atoms display a cer-

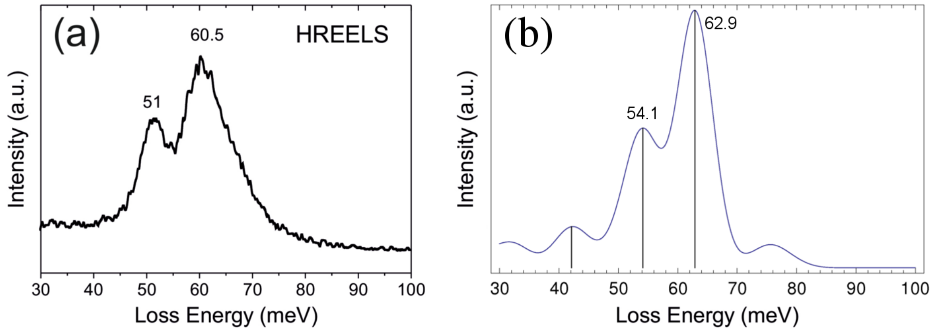

Figure 2.3: (a) Experimental HREELS spectrum of the (6×1) NiO layer on Rh(111) and (b) the calculated vibrational spectrum weighted by the dipole activity of the modes.

tain flexibility to connect the network and appear in both triangular and rectangular units. It should be noted that with a Ni-Ni distance of 2.70 Å along the Rh rows and 2.50 Å in the perpendicular direction, the arrangement of the Ni atoms in the rectangular units is strongly compressed with respect to the ideal NiO(100) bulk planes (2.96 Å), resulting in a local deformation of the layer with an uniaxial buckling (Fig. 2.2 (a), (b), black arrows).

## 2.3 Vibrational Spectrum

High-resolution electron energy loss spectroscopy (HREELS) provides additional information about the chemical composition and structure of the (6×1) NiO phase and allows us to confirm the predicted model by comparing the experimental phonon loss structure with the calculated infrared intensity spectrum. The infrared intensities of the vibrational eigenmodes were calculated via Born effective charges. The experimental phonon loss structure (Fig. 2.3 (a)) consists of a main phonon loss peak at 60.5 meV, which is asymmetrically broadened at the high-energy side, and a second peak at 51 meV. Indeed, this observation is in very good agreement with the calculated vibrational spectrum of the $Ni_5O_5$ (6×1) model (Fig. 2.3 (b)), which shows two dipole active modes for the out-of-plane vibrations of the uppermost O atoms (Fig. 2.2 (a), (b), bright red atoms) at 63 meV and 54 meV.

## 2.4 Thermodynamic Stability

In order to assess the thermodynamic stability of the $Ni_5O_5$ and competing structures we calculated the Gibbs free energy of each phase as a function of the oxygen chemical potential, which can be related to the experimental conditions (temperature $T$ and pressure $p$). This approach is discussed in detail in Ref. [19]. Neglecting vibrational contributions, the Gibbs free energy, which is the appropriate thermodynamic potential for constant $T$ and $p$, can be approximated by

$$\Delta G(\mu_{\mathrm{O}}) = \frac{1}{A}[E_{\mathrm{tot}} - N_{\mathrm{Rh}}\, E_{\mathrm{Rh}} - N_{\mathrm{Ni}}\, \mu_{\mathrm{Ni}} - N_{\mathrm{O}}\, (\mu_{\mathrm{O}} + E_{\mathrm{O}})]. \tag{2.1}$$

$E_{\mathrm{tot}}$ is the total energy of the system, $E_{\mathrm{Rh}}$ is the energy per atom in bulk rhodium, and $E_{\mathrm{O}}$ is half the energy of an isolated $\mathrm{O}_2$ molecule. We approximate the chemical potential of nickel, $\mu_{\mathrm{Ni}}$, by the bulk energy $E_{\mathrm{Ni}}$. From our DFT calculations we obtained $E_{\mathrm{Rh}} = -7.28\,\mathrm{eV}$, $E_{\mathrm{O}} = -5.03\,\mathrm{eV}$, and $E_{\mathrm{Ni}} = -5.47\,\mathrm{eV}$. $N_{\mathrm{Rh}}$, $N_{\mathrm{Ni}}$, and $N_{\mathrm{O}}$ are the numbers of rhodium, nickel, and oxygen atoms, respectively. $A$ is the surface area and $\mu_{\mathrm{O}} = \mu_{\mathrm{O}}(T, p)$ is the oxygen chemical potential, which relates the calculated energy $\Delta G(\mu_{\mathrm{O}})$ to the experimental temperature $T$ and pressure $p$. Treating the gas of $\mathrm{O}_2$ molecules as an ideal gas at constant temperature and pressure, the chemical potential of $\mathrm{O}_2$, $\mu_{\mathrm{O}_2}$, is equal to the Gibbs free energy per molecule

$$G_{\mathrm{O}_2}(T, p) = -\, k_B T \ln q(T, p), \tag{2.2}$$

with the molecular partition function [20]

$$q(T, p) = q^{\mathrm{t}}(T, p)\, q^{\mathrm{r}}(T)\, q^{\mathrm{v}}(T)\, q^{\mathrm{e}}(T). \tag{2.3}$$

The oxygen chemical potential is then simply given by

$$\mu_{\mathrm{O}}(T, p) = \mu_{\mathrm{O}_2}(T, p)/2 = G_{\mathrm{O}_2}(T, p)/2. \tag{2.4}$$

The only contribution that depends on both temperature and pressure is the translational partition function

$$q^{\mathrm{t}}(T, p) = \frac{k_B T}{p} \left( \frac{2\pi m k_B T}{h^2} \right)^{3/2}, \tag{2.5}$$

where $m$ is the mass of the $\mathrm{O}_2$ molecule and $h$ is Planck's constant. The rotational partition function is given by

$$q^{\mathrm{r}}(T) = \frac{k_B T I}{\hbar^2}, \tag{2.6}$$

where $I$ is the moment of inertia of the $\mathrm{O}_2$ molecule and $\hbar = h/2\pi$. The vibrational partition function is calculated as

$$q^{\mathrm{v}}(T) = \frac{1}{1 - \exp[-\beta h c \nu]}, \tag{2.7}$$

where $c$ is the speed of light in vacuum. In this work, the vibrational frequency $\nu = 1580\,\mathrm{cm}^{-1}$ was obtained from DFT calculations. Assuming that electronically excited states are not accessible at relevant temperatures, the electronic partition function is of no importance,

$$q^{\mathrm{e}}(T) = 1. \tag{2.8}$$

In experiment, in order to prepare the nickel oxide layers, a sample of Ni on Rh(111) was exposed to a molecular oxygen atmosphere. The temperature during the oxidation was 350°C at a pressure of $5 \times 10^{-8}$ mbar. According to (2.2) and (2.4) this corresponds to a chemical potential of $\mu_{\mathrm{O}} = -1.245\,\mathrm{eV}$. It is worth noting that the oxygen chemical potential can also be computed by

$$\mu_{\mathrm{O}}(T,\,p) = \mu_{\mathrm{O}}(T,\,p^{\circ}) + 1/2\,k_B T \ln(p/p^{\circ}) \tag{2.9}$$

(see Ref. [19]), where $\mu_{\mathrm{O}}(T,\,p^{\circ})$ is obtained from thermochemical tables. Assuming linear behavior of $\mu_{\mathrm{O}}(T,\,p^{\circ})$ in the temperature range between 600 K and 700 K at $p^{\circ} = 1\,\mathrm{atm}$, applying (2.9) yields $\mu_{\mathrm{O}} = -1.275\,\mathrm{eV}$ for the abovementioned experimental conditions ($\mu_{\mathrm{O}}(600\,\mathrm{K}, 1\,\mathrm{atm}) = -0.61\,\mathrm{eV}$ and $\mu_{\mathrm{O}}(700\,\mathrm{K}, 1\,\mathrm{atm}) = -0.73\,\mathrm{eV}$ taken from [19]), which is in good agreement with our value obtained from (2.2) and (2.4).

A phase diagram displaying the thermodynamic stability of various competing phases is shown in Fig. 2.4. This diagram reveals that the sizable lattice mismatch between the Rh substrate (lattice parameter $a = 3.82$ Å) and both the metallic Ni ($a = 3.52$ Å) and the bulk NiO lattices ($a = 4.21$ Å) plays a key role as it hinders an epitaxial growth of the corresponding films. The phase diagram shows clearly that the epitaxially grown Ni films are highly strained and thus rather unstable (Fig. 2.4, orange dashed line). Even though the adsorption of p(2×1) oxygen leads to a reduction of the stress of the Ni layer (Fig. 2.4, blue solid line), a mere oxygen adsorption phase (Fig. 2.5) remains only thermodynamically stable under oxygen-poor conditions ($\mu_{\mathrm{O}} < -1.3\,\mathrm{eV}$). This latter structure may thus correspond to the p(2×1) minority phase, observed to coexist with the (6×1) majority phase in the experiment, which marks the onset of the oxidation of the Ni layer. It should be noted that the high surface stress prevents the formation of a p(2×1) phase on the bare Ni(111) surface [21], but for the supported Ni monolayer, a certain amount of oxygen is even needed for a sufficient expansion of the NiO layer.

The (6×1) $Ni_5O_5$ stoichiometry (Fig. 2.4, red solid line) represents already the highest oxygen content that can be accommodated in a single flat NiO layer as additional oxygen can only be incorporated in the surface oxide layer by increasing both the Ni and O coverage. Fig. 2.6 displays the optimized (hypothetical) $Ni_6O_6$ structure with a (6×1) cell. The phase diagram clearly displays that this structure is only metastable, even though the energy difference to the $Ni_5O_5$ structure is rather small. Evaluating the related work

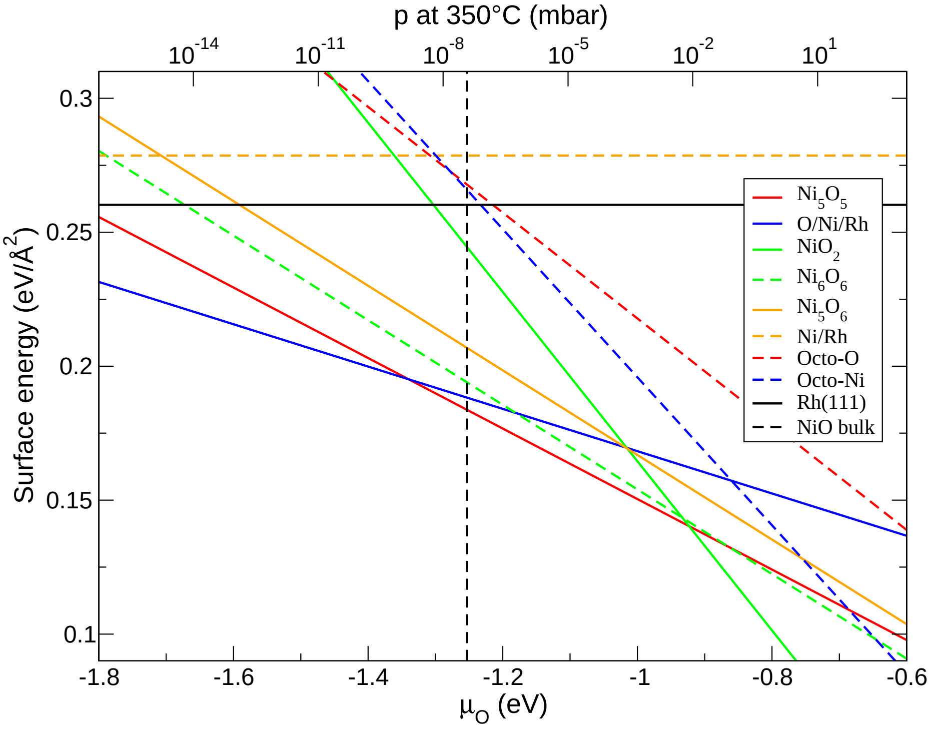

Figure 2.4: Phase stability diagram as constructed from equation (2.1). The values for the pressure $p$ were obtained by applying equation (2.4).

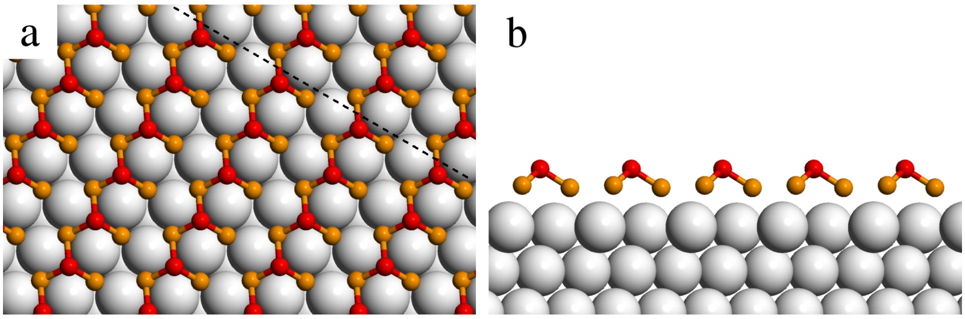

Figure 2.5: (a) Top view and (b) side view of the structural model for p(2×1) chemisorbed O on Ni/Rh(111) (blue solid line in Fig. 2.4). Ni (Rh) atoms are shown in orange (gray), O atoms are in red. The cutting plane for (b) is indicated as a black dashed line in (a).

functions allows one to assess the role of the induced surface dipoles. The calculations show a pronounced effect of the electronic contributions. While the calculated work function of the bare Rh(111) surface is increased from $\phi = 5.13\,\text{eV}$ to a value of $5.96\,\text{eV}$ ($\Delta\phi = 0.83\,\text{eV}$), the work function after the formation of the $Ni_5O_5$ layer is only increased to $5.17\,\text{eV}$ ($\Delta\phi = 0.04\,\text{eV}$).

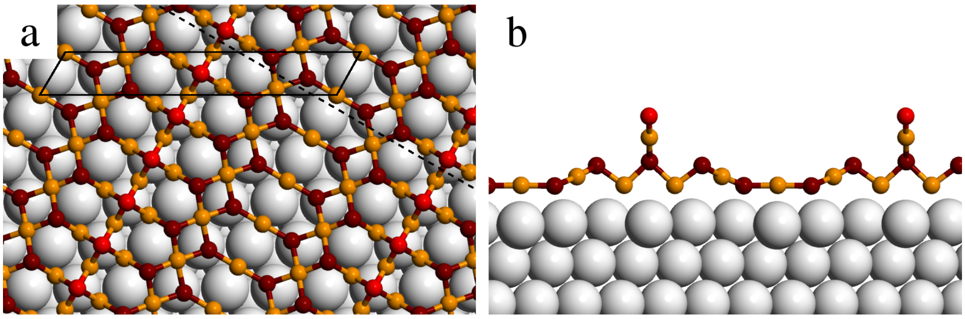

Figure 2.6: (a) Top view and (b) side view of the structural model for the (6×1) $Ni_6O_6$ structure (green dashed line in Fig. 2.4). Termination O atoms are in bright red, other O atoms are in dark red.

On the contrary, the presence of a $Ni_6O_6$ layer would lead to a change in the work function of $\Delta\phi = 1.37\,\text{eV}$. Therefore, only a very minor surface dipole is induced by the formation of the $Ni_5O_5$ layer.

If the oxygen content is increased even further, a thicker NiO film is formed. A comparison of several terminations demonstrates that the ultrathin film with a thickness slightly larger than 1 ML does not correspond to either oxygen- (Fig. 2.4, red dashed line; model in Fig. 2.7 (a), (b)) or Ni-terminated (Fig. 2.4, blue dashed line; model in Fig. 2.7 (c), (d)) octopolar reconstructions, which have been observed for the bulk NiO(111) surface [10, 11]. Instead, we predict that the NiO layer is transformed into an epitaxial (nonpolar) $NiO_2$ trilayer in an oxygen-rich environment (Fig. 2.8). Yet, the transformation into this high-coverage structure is only predicted for a significantly higher chemical potential of oxygen ($\mu_O > -1.0\,\text{eV}$), which corresponds to rather high oxygen partial pressures (Fig. 2.4).

## 2.5 Summary

A nonpolar (6×1) NiO film has been identified on the Rh(111) surface by STM and DFT calculations. The calculations demonstrate that the film has a formal stoichiometry of $Ni_5O_5$, which is the highest amount of oxygen that can be accommodated in a single NiO layer on this surface orientation. Due to the large lattice mismatch between the NiO and the Rh(111) support, the $Ni_5O_5$ layer is not formed as a uniform structural film but consists of two different building blocks that are related to (111) and (100) NiO surface terminations. The combination of both structural elements leads to the formation of pronounced troughs along the [110] direction. These troughs create a potential template for the growth of low-dimensional nanostructures with a well-defined width.

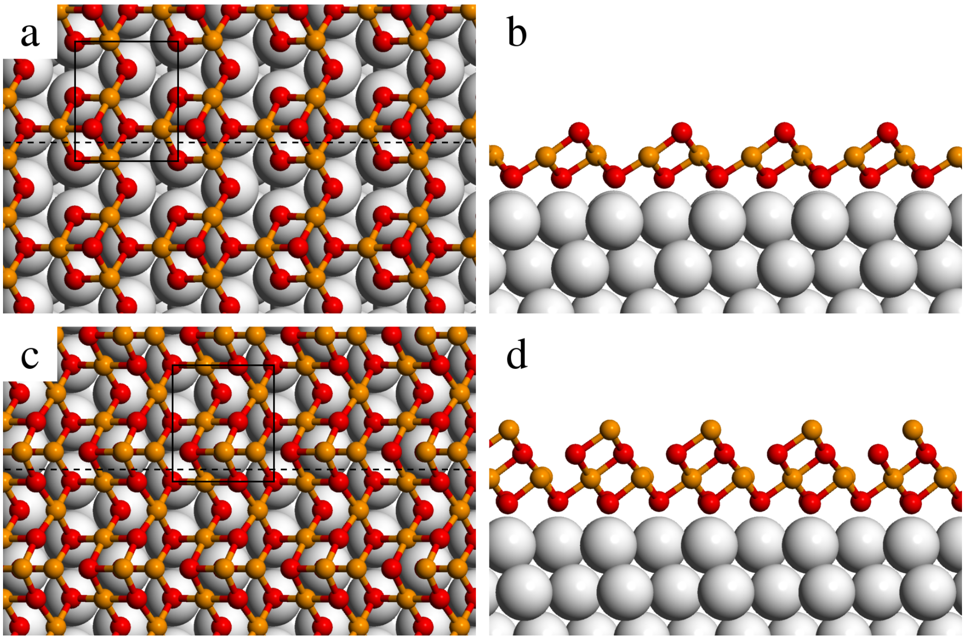

Figure 2.7: Structural models for octopolar reconstructions: (a) top view and (b) side view of the O-terminated reconstruction (red dashed line in Fig. 2.4); (c) top view and (d) side view of the Ni-terminated reconstruction (blue dashed line in Fig. 2.4). The cutting planes for (b) and (d) are indicated as a black dashed lines in (a) and (c), respectively.

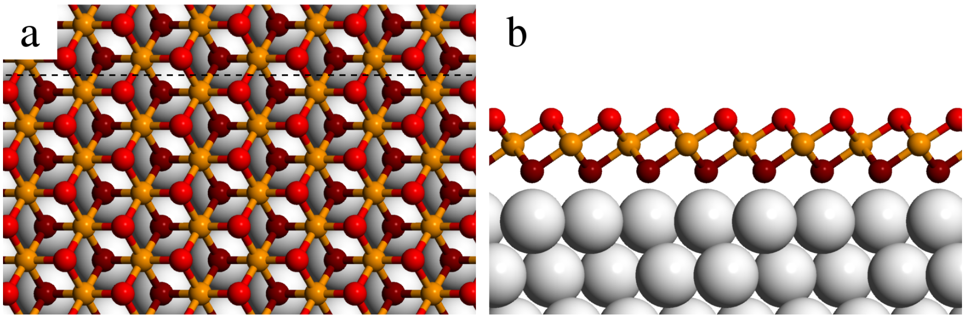

Figure 2.8: (a) Top view and (b) side view of the structural model for the $NiO_2$ structure (green solid line in Fig. 2.4). Ni (Rh) atoms are shown in orange (gray), termination O atoms are in bright red, lower O atoms are in dark red.

# Chapter 3

# CO on $NiO_2$-Rh(553)

## 3.1 Introduction

The oxidation of transition metal surfaces has been an active research topic in recent years and there has been a lot of discussion about the catalytic activity of the resulting surface oxides. It turns out that an extended two-dimensional surface oxide film is not very active, but that the oxide film needs to offer edges in order that enhanced catalytic activity can be observed (see [22] and references therein). Such edges are naturally provided by quasi-one-dimensional oxide structures. It has been shown that quasi-one-dimensional nickel oxide nanowires of formal $NiO_2$ stoichiometry can be experimentally fabricated on the Rh(553) surface [23]. This surface offers a regular array of steps at which the oxide stripes can form. Between neighboring step edges, the Rh(553) surface exhibits (111) terraces containing five rows of rhodium atoms (Fig. 3.1).

In the present chapter, we report on the study of the catalytic activity of these quasi-one-dimensional $NiO_2$ stripes on the Rh(553) surface. We address the question of whether these oxide stripes increase the reactivity for a probe reaction, namely the oxidation of carbon monoxide (CO) and the subsequent desorption of carbon dioxide ($CO_2$), compared to the bare Rh(111) and Rh(553) surfaces. We will also present the atomistic details of the reaction mechanism by following the reaction process from the chemisorbed CO to the desorbed $CO_2$ molecule in its gas phase state.

A part of this material has been published in

S. Surnev, F. Allegretti, G. Parteder, T. Franz, F. Mittendorfer, J. N. Andersen, F. P. Netzer, *One-Dimensional Oxide-Metal Hybrid Structures: Site-Specific Enhanced Reactivity for CO Oxidation*, ChemPhysChem 11, 2506 (2010).

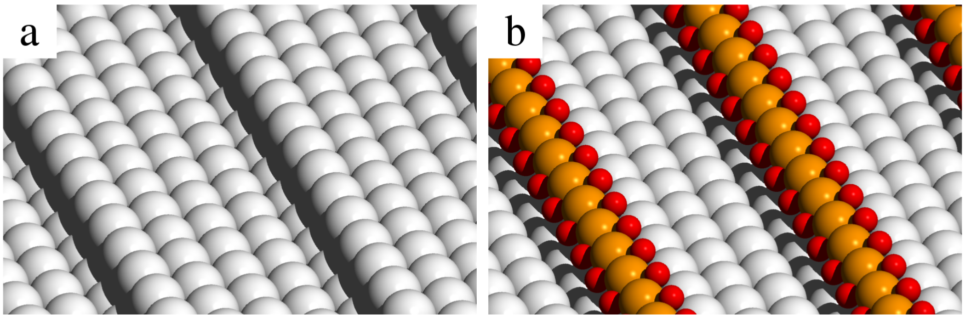

Figure 3.1: (a) The Rh(553) surface exhibits five-atom-wide (111) terraces between neighboring steps. (b) Quasi-one-dimensional nickel oxide nanowires grown at the steps of the Rh(553) surface. Nickel atoms are shown in orange, oxygen atoms in red.

## 3.2 Methods for finding reaction mechanisms, energy barriers and reaction rate constants

### 3.2.1 Rare Events and Transition States

Transitions between stable states of a system are *activated processes*, which means that for the transition to occur an energy barrier has to be overcome. Given a typical experimental temperature of 320 K, the *thermal energy* is about 0.03 eV, whereas in most transitions of interest in atomic systems the barriers to be surmounted are significantly higher. As a consequence these processes occur very infrequently, which is why they are referred to as *rare events*. As an example, in the following study the fastest *reaction rate constant* (number on average of reactions per molecule per second) at 320 K for a CO molecule to react with oxygen on the $NiO_2$-Rh(553) surface and to desorb as $CO_2$ will be about $10^{-3}\,s^{-1}$. This means that when using a simulation cell including only one CO molecule, we would, on average, have to simulate a real time of almost 17 minutes at 320 K to observe a single transition. Yet calculating sufficiently exact classical trajectories of atomic systems by integrating Newton's equations of motion requires time steps of only a few femto seconds, which limits the real time that can be simulated with DFT for realistic systems usually to less than a micro second. Consequently it is hopeless to attempt at studying transitions with a significant energy barrier directly by calculating trajectories, and other strategies are necessary to identify reaction mechanisms and to estimate their rate constants. These strategies aim at revealing certain details of the *potential energy surface* (PES), which is the potential energy as a function of the coordinates of all atoms (function of the configuration space), at zero temperature. A *minimum energy path* (MEP) of a particular transition is a path on the PES, where at each point of the path the system follows the (positive or negative) local gradient of the potential energy. For a transition from one minimum on the PES to another minimum, the MEP passes through a saddle point, which is a maximum along the direction of the MEP and a minimum along all other directions. The configuration which corresponds to this special point on the PES is called a *transition state*. Being aware of this relation between saddle point and transition state, we will frequently use these two notions synonymously, which is acceptable for zero temperature. Between two stable states there might be multiple minimum energy pathways, each of which passing through a different saddle point. The probability for a transition from one stable state to another one is related to the height of the separating saddle point of a MEP with respect to the initial state. Knowledge of all relevant saddle points yields the activation barriers and allows for the estimation of rate constants, providing information about energetically preferred transitions.

### 3.2.2 Nudged Elastic Band

The *nudged elastic band* method (NEB) [24, 25, 26] is applied to determine the minimum energy path between two given structural configurations of an atomic system. Several *images* (different configurations) of the system are created and connected with one another via artificial *spring forces*. The set of images $\{\mathbf{R}_0, \mathbf{R}_1, \ldots, \mathbf{R}_N\}$, where the vector $\mathbf{R}_i$ contains the positions of all atoms of image $i$, is referred to as a band. Images $\mathbf{R}_0$ and $\mathbf{R}_N$ remain fixed, while the other images are moved simultaneously using standard optimization algorithms. To carry out these relaxations, we employed the *damped molecular dynamics* mode of VASP, where a damped second order equation of motion is integrated with a velocity Verlet algorithm. Let $U$ be the potential energy function of the system under investigation, then the total force acting on image $i$ is

$$\mathbf{F}_i = \mathbf{F}_i^s - \boldsymbol{\nabla} U(\mathbf{R}_i) + \boldsymbol{\nabla} U(\mathbf{R}_i) \cdot \hat{\boldsymbol{\tau}}_i \, \hat{\boldsymbol{\tau}}_i. \tag{3.1}$$

The unit vector $\hat{\boldsymbol{\tau}}_i$ is the local tangent of the band at image $i$, and $\mathbf{F}_i^s$ is the component of the spring force parallel to $\hat{\boldsymbol{\tau}}_i$. Only the component orthogonal to $\hat{\boldsymbol{\tau}}_i$ of the force stemming from the potential $U$ contributes to the total force $\mathbf{F}_i$. At every step of the structural relaxation, the tangent and total force are updated for each image. In this manner, the band will converge to the nearest MEP if the number of images is sufficiently large, thereby providing a discrete representation of the MEP. Typically, we used a set of 16 images. In most cases, the fixed images $\mathbf{R}_0$ and $\mathbf{R}_N$ correspond to minima on the potential energy surface. However, these points do not necessarily need to be energy minima in all degrees of freedom. The method works equally well if the fixed images are not energy minima, but reside on the minimum energy path. Consequently, any two images of a band, which has been converged sufficiently well to a MEP, can be used as fixed images of another NEB calculation. This was done in the present work in a few cases.

We used the *climbing image nudged elastic band method* (cNEB) of Henkelman *et al* [27], where the image of highest energy in the band is made to 'climb up' towards increasing energy along the MEP on the potential energy surface. In the cNEB method the image $j$ with the highest energy is not affected by spring forces. Furthermore, the component of the force stemming from the potential $U$, which is parallel to the tangent vector, is inverted. Hence the total force on this image is [27]

$$\mathbf{F}_j = -\boldsymbol{\nabla} U(\mathbf{R}_j) + 2\,\boldsymbol{\nabla} U(\mathbf{R}_j) \cdot \hat{\boldsymbol{\tau}}_j\,\hat{\boldsymbol{\tau}}_j, \tag{3.2}$$

whereas the forces acting an all the other images in the band are given by (3.1). The tangent vector at image $i$ is [28]

$$\boldsymbol{\tau}_i = \left\{ \begin{array}{lll} \mathbf{R}_{i+1} - \mathbf{R}_i & \text{if} & U_{i+1} > U_i > U_{i-1} \\ \mathbf{R}_i - \mathbf{R}_{i-1} & \text{if} & U_{i+1} < U_i < U_{i-1} \end{array} \right. , \tag{3.3}$$

where $U_i := U(\mathbf{R}_i)$, and in case of $U_{i+1} > U_i < U_{i-1}$ or $U_{i+1} < U_i > U_{i-1}$,

$$\boldsymbol{\tau}_i = \left\{ \begin{array}{lll} (\mathbf{R}_{i+1} - \mathbf{R}_i)\Delta U_i^{\max} + (\mathbf{R}_i - \mathbf{R}_{i-1})\Delta U_i^{\min} & \text{if} & U_{i+1} > U_{i-1} \\ (\mathbf{R}_{i+1} - \mathbf{R}_i)\Delta U_i^{\min} + (\mathbf{R}_i - \mathbf{R}_{i-1})\Delta U_i^{\max} & \text{if} & U_{i+1} < U_{i-1} \end{array} \right. , \tag{3.4}$$

where

$$\Delta U_i^{\max} = \max(|U_{i+1} - U_i|,\, |U_{i-1} - U_i|)$$

and

$$\Delta U_i^{\min} = \min(|U_{i+1} - U_i|,\, |U_{i-1} - U_i|).$$

Equations (3.1) and (3.2) require the normalized tangent vector $\hat{\boldsymbol{\tau}}_i = \boldsymbol{\tau}_i/|\boldsymbol{\tau}_i|$. Compared to previous definitions of the tangent vector, (3.3) and (3.4) reduce the tendency of the band to form kinks. The spring force, which is required in (3.1), is calculated as [28]

$$\mathbf{F}_i^s = k(|\mathbf{R}_{i+1} - \mathbf{R}_i| - |\mathbf{R}_i - \mathbf{R}_{i-1}|)\hat{\boldsymbol{\tau}}_i, \tag{3.5}$$

where $k$ is the spring constant.

Whereas when using the original NEB scheme, in most cases additional techniques are needed to identify the transition state, this is not necessary with the cNEB method. The climbing image often converges exactly to the saddle point.

If the band is initially set up linearly in configuration space between the two fixed images, very small relaxation steps may be necessary because of possibly extremely large forces acting on atoms in some of the images. Furthermore, it is very important not to apply equation (3.2) from the beginning if the band is initially far off the MEP. Doing so may cause the wrong image to move towards increasing energy and thus the calculation will fail. Generally, we used an algorithm according to equation (3.1) for all images until all total forces had dropped below 0.3 eV/Å or even less, and only then employed equation (3.2) for the image of highest energy. Note that according to (3.3) and (3.4) the direction toward which the climbing image moves is determined by the coordinates of the adjacent images. Hence this direction may be ill defined if these images are not close to the MEP.

One should bear in mind that generally there is no guarantee that the MEP found with NEB is indeed the one with the lowest transition state. The band converges to a MEP that is close to its initial course in configuration space, which can be set up arbitrarily. Since there may be multiple reaction paths connecting stable states, it can not be ruled out that there exists a more favorable MEP than the one obtained from a particular NEB calculation.

### 3.2.3 Dimer Method

The *dimer method* [29, 30] is designed to find saddle points on the potential energy surface, but it does not provide information about the explicit minimum energy pathway like the NEB. Two images,

$$\mathbf{R}_1 = \mathbf{R} + \Delta\mathrm{R}\,\hat{\boldsymbol{n}} \quad \text{and} \quad \mathbf{R}_2 = \mathbf{R} - \Delta\mathrm{R}\,\hat{\boldsymbol{n}}, \tag{3.6}$$

separated by a small distance $2\Delta\mathrm{R}$, constitute the dimer, where $\mathbf{R}$ is a point in the configuration space and $\hat{\boldsymbol{n}}$ is a unit vector. The dimer is subject to rotations and translations. At some location on the PES, the sum of the energies of the two images, $E_1 + E_2$, is minimized by rotation, which is equivalent to aligning the dimer along the mode of lowest curvature, as can be seen from the expression for the curvature $C$ of the PES at $\mathbf{R}$ along $\hat{\boldsymbol{n}}$ [29, 30]:

$$C \approx \frac{E_1 + E_2 - 2E_0}{(\Delta\mathrm{R})^2}. \tag{3.7}$$

Here, $E_0$ is the energy of the midpoint $\mathbf{R}$ between the two images, which is fixed during rotation. Subsequently to rotation the dimer is translated according to the total force acting on the images with the component parallel to $\hat{\boldsymbol{n}}$ being inverted.

The method does not require knowledge of the final state of a transition. Initially the dimer can be located near an energy minimum on the PES as well as in the vicinity of a saddle point if some guess of a transition state is available. In the present work, we used this method exclusively in the latter context.

### 3.2.4 Quasi-Newton Algorithms

When optimizing structures of atomic systems, quasi-Newton methods are frequently used if a good initial guess of the atomic positions is available.

Then these methods are very efficient. Quasi-Newton methods are based on Newton's method for finding the root of a function (cf., e.g., Ref. [31]), which is accomplished by the iterative scheme

$$x_{n+1} = x_n - \frac{f(x_n)}{f'(x_n)}. \tag{3.8}$$

For a "well-behaved" function $f(x)$, this series converges towards a root of $f$ if the initial guess $x_0$ is close enough to this root. To determine a minimum of $f$, the first derivative $f'$ must be zero, i.e. the minimum is a root of the derivative. Hence

$$x_{n+1} = x_n - \frac{f'(x_n)}{f''(x_n)} \tag{3.9}$$

will converge towards the desired minimum for a reasonably chosen $x_0$. For multiple dimensions, as in the case of the potential energy function of an atomic system, (3.9) generalizes to

$$\mathbf{x}_{n+1} = \mathbf{x}_n - \mathbf{H}^{-1}\,\nabla f(\mathbf{x}_n), \tag{3.10}$$

with the Hessian matrix $\mathbf{H}$ and the gradient $\nabla f(\mathbf{x}_n)$. In quasi-Newton methods, the exact Hessian is not calculated, but an approximation of its inverse is computed from gradient vectors of previous iteration steps. The algorithm implemented in VASP is referred to as *residual minimization, direct inversion in the iterative subspace* (RMM-DIIS) [32].

What is essential for the present chapter is that a vanishing first derivative is a condition which holds not only for minima but also for maxima and saddle points. Consequently, also the latter can be found by applying Newton's method and we can use a quasi-Newton algorithm in order to find transition states. However, this will only be successful if our initial guess for the structural geometry is close enough to a transition state. This is, e.g., the case if some preconverged transition state structure with a slab of 4 substrate layers is to be recalculated with 7 layers, as it was often done in the present work, or if numerical parameters like the energy cutoff or the k-point density in the Brillouin zone are altered in order to increase the numerical accuracy. A good initial guess may also be at hand if a structure arises from a nudged elastic band calculation. In this regard it may in some cases be more efficient not to completely converge the band to the MEP but to stop at a certain point in the course of the NEB calculation and to continue with a quasi-Newton method for the energetically highest image of the band.

### 3.2.5 Verification of Transition States

If one of the methods described above has converged to a particular structure, it is advisable to perform further tests to verify that this structure is indeed a transition state and to identify the connected neighboring energetic minima. This can be checked by analyzing the local curvature of the PES via the Hessian and, subsequently, following the MEP from the saddle point down to minima by careful structure relaxations.

Diagonalization of the Hessian gives a set of eigenvectors which are the *normal coordinates* or *vibrational modes* of the system for a particular atomic configuration. At a saddle point, the curvature of the PES is negative in exactly one of these directions and positive in all the remaining directions. In a harmonic approximation, the frequency of a vibrational mode is proportional to the square root of the curvature of the PES in the direction of the mode. Consequently, due to the negative curvature in exactly one direction, a saddle point exhibits one, and only one, imaginary vibrational frequency, whereas a minimum exhibits only real frequencies. If the forces acting on a particular atomic structure are vanishing, the entire set of vibrational frequencies of this structure should be calculated to verify it to be a transition state.

These vibrational frequencies are not only valuable in order to assess whether a certain structure is a transition state, but they are also needed in order to calculate the vibrational partition function, which is necessary for evaluating reaction rate constants, as will be discussed below.

After verifying a transition state, it has to be checked which minima on the PES (and, accordingly, which stable configurations in real space) are connected by this saddle point. This can be accomplished by slightly displacing the system from the transition state in opposite directions along the eigenvector corresponding to the imaginary frequency (i.e. the local tangent to the MEP), and subsequent relaxation. We have conducted these relaxations by applying damped molecular dynamics, where we have used very small relaxation steps to ensure that the system stays close to the MEP in the course of the relaxation from the saddle point to the respective minimum. This approach yields an explicit mapping of the reaction from the reactant state to the product state.

### 3.2.6 Transition State Theory

Once all relevant saddle points have been found, reaction rate constants can be calculated in the framework of *transition state theory* (TST) [33, 34]. This theory assumes that the transition over a barrier involves the activation of only one degree of freedom, which is called the *reaction coordinate*, and that initial and transition state are in thermal equilibrium with respect to all remaining degrees of freedom [35]. In principle, for a system with a potential energy surface of dimensionality $n$, a *dividing surface* of dimensionality $n$-1, which is locally orthogonal to the reaction coordinate, can be identified [36]. Since at elevated temperatures the system is not restricted to the minimum energy path on the PES when surmounting a barrier, the whole dividing surface is identified as the transition state. Note that only for the zero

Kelvin potential energy surface we use 'saddle point' and 'transition state' synonymously in the present work. TST assumes that once the system reaches the dividing surface, it will proceed toward the final state of the reaction, i.e. each trajectory crosses the dividing surface only once. Because of this assumption the rate from TST is considered to be an upper bound for the true rate.
In the most general form of TST, the rate constant is given by [35, 37]

$$k_{\mathrm{TST}} = \frac{k_B T}{h} \frac{Q^{\ddagger}}{Q^A}. \tag{3.11}$$

$Q^A$ is the partition function at the initial state, and $Q^{\ddagger}$ is the partition function at the transition state for all degrees of freedom except for the reaction coordinate, hence $Q^{\ddagger}$ is proportional to the configuration integral over the dividing surface [36]. A partition function $Q$ is the product

$$Q = Q_{\mathrm{tr}} Q_{\mathrm{rot}} Q_{\mathrm{vib}} Q_{\mathrm{el}} \tag{3.12}$$

of translational, rotational, vibrational, and electronic contributions. For a chemisorbed molecule like carbon monoxide on a surface, the translations and rotations of the molecule are *frustrated degrees of freedom* of a subsystem and become vibrational degrees of freedom of the overall system, contributing to $Q_{\mathrm{vib}}$. For this kind of system, there are no translational or rotational contributions to the partition function $Q$, so that we can set

$$Q_{\mathrm{tr}} = Q_{\mathrm{rot}} = 1 \tag{3.13}$$

for both the initial and transition state. Note that (3.13) may not hold in the case of weak physisorption.
If electronically excited states do not contribute at relevant temperatures, the ratio of the electronic partition functions is simply

$$\frac{Q^{\ddagger}_{\mathrm{el}}}{Q^A_{\mathrm{el}}} = \exp[-\beta\,(U^{\ddagger} - U^A)], \tag{3.14}$$

where $U^{\ddagger}$ and $U^A$ are the ground state (0 K) potential energies of the saddle point and the energy minimum of the initial state, respectively, and $\beta = (k_B T)^{-1}$. With (3.13) and (3.14) the rate (3.11) becomes [38]

$$k_{\mathrm{TST}} = \frac{k_B T}{h} \frac{Q^{\ddagger}_{\mathrm{vib}}}{Q^A_{\mathrm{vib}}} \exp[-\beta\,(U^{\ddagger} - U^A)]. \tag{3.15}$$

This is an Arrhenius-like equation, where the factor

$$\nu^*(T) = \frac{k_B T}{h} \frac{Q^{\ddagger}_{\mathrm{vib}}}{Q^A_{\mathrm{vib}}} \tag{3.16}$$

can be seen as a temperature dependent effective frequency of dimension $s^{-1}$, which is often referred to as the *prefactor*. The temperature dependence of $\nu^*$ is not only due to the thermal energy $k_BT$, but also due to the vibrational partition functions $Q^{\ddagger}_{\text{vib}}$ and $Q^{A}_{\text{vib}}$, which themselves depend on temperature. In the harmonic approximation, each vibrational mode is treated as a harmonic oscillator with the partition function

$$\sum_{n=0}^{\infty} \exp[-\beta h\nu(n+\frac{1}{2})] = \frac{\exp[-\beta h\nu/2]}{1-\exp[-\beta h\nu]}, \tag{3.17}$$

where $\nu$ is the frequency of the mode. Consequently, the vibrational partition functions in (3.15) are

$$Q^{\ddagger}_{\text{vib}} = \prod_{i=1}^{N-1} \frac{\exp[-\beta h\nu_i^{\ddagger}/2]}{1-\exp[-\beta h\nu_i^{\ddagger}]} \tag{3.18}$$

and

$$Q^{A}_{\text{vib}} = \prod_{i=1}^{N} \frac{\exp[-\beta h\nu_i/2]}{1-\exp[-\beta h\nu_i]}, \tag{3.19}$$

where $N$ is the number of vibrational modes. Note that N frequencies $\{\nu_i\}$ contribute to $Q^{A}_{\text{vib}}$, whereas only $N-1$ frequencies $\{\nu_i^{\ddagger}\}$ contribute to $Q^{\ddagger}_{\text{vib}}$. At the transition state, the frequency of one vibrational mode is imaginary. Only the real frequencies are included in (3.18). By doing so, the contributions of the reaction coordinate are excluded from the overall partition function as we demanded for $Q^{\ddagger}$ in (3.11).

In case of $\beta h\nu \ll 1$, the exponential functions in (3.17) can be expanded in a Taylor series around zero, $\exp[x] \approx 1 + x$ for $x \ll 1$, which yields for the vibrational partition functions

$$Q^{\ddagger}_{\text{vib}} = \prod_{i=1}^{N-1} \frac{k_BT}{h\nu_i^{\ddagger}} \tag{3.20}$$

and

$$Q^{A}_{\text{vib}} = \prod_{i=1}^{N} \frac{k_BT}{h\nu_i}. \tag{3.21}$$

Substitution of (3.20) and (3.21) into (3.15) yields the formula often found in literature [36, 38]:

$$k_{\text{TST}} = \frac{\prod\limits_{i=1}^{N} \nu_i}{\prod\limits_{i=1}^{N-1} \nu_i^{\ddagger}} \exp[-\beta\,(U^{\ddagger} - U^{A})]. \tag{3.22}$$

Note that there is one frequency more in the numerator than in the denominator. The effective frequency, in contrast to (3.16), is now independent of the temperature:

$$\nu^{**} = \frac{\prod_{i=1}^{N} \nu_i}{\prod_{i=1}^{N-1} \nu_i^{\ddagger}}. \tag{3.23}$$

In the study reported below, we considered temperatures ranging from 150 K to 420 K. For the transitions investigated here, the quantity $\beta h\nu$ is between 0.3 and 18.7 at 150 K, and between 0.1 and 6.7 at 420 K, i.e. the condition $\beta h\nu \ll 1$ is only partially fulfilled at best. Consequently, use of (3.18) and (3.19) with (3.15) was necessary instead of (3.22) in order to calculate the rate constants. However, it will be shown later that for these transitions $\nu^*(T)$ in (3.16) varies only little with temperature and that the values of this function do not significantly deviate from its classical limit $\nu^{**}$. We calculated rate constants employing (3.18) and (3.19) as well as (3.22) and found that, although the condition $\beta h\nu \ll 1$ does not hold, the application of (3.22) is justified in this study.

It is also instructive to write the transition rate constant in a different form. In the canonical ensemble, the partition function $Q$ and the *Helmholtz free energy* $F$ are related via

$$Q = \exp[-\beta F] = \exp[-\beta(E - TS)], \tag{3.24}$$

where $E$ is the *internal energy* and $S$ is the *entropy*. Using this relation, the rate (3.11) can be expressed as

$$k_{\text{TST}} = \frac{k_B T}{h} \exp[-\beta \Delta F], \tag{3.25}$$

with the free energy difference $\Delta F = F^{\ddagger} - F^{A}$ between the free energy of the transition state,

$$F^{\ddagger} = -\, k_B T \ln Q^{\ddagger}, \tag{3.26}$$

and the free energy of the initial state,

$$F^{A} = -\, k_B T \ln Q^{A}. \tag{3.27}$$

Equation (3.25) can be quite useful since there exist multiple simulation techniques to calculate free energy differences without direct evaluation of partition functions.

Further insight into the nature of rate constants from TST is provided by writing (3.25) as

$$k_{\text{TST}} = \frac{k_B T}{h} \exp[\Delta S / k_B] \exp[-\beta \Delta E], \tag{3.28}$$

which yields an effective frequency $(k_BT/h)\exp[\Delta S/k_B]$ that is related to the change in entropy $\Delta S$ from the initial state to the transition state. However, the term $\exp[-\beta\Delta E]$ in (3.28) is not to be confused with the term $\exp[-\beta\,(U^{\ddagger}-U^{A})]$ in (3.15) or in (3.22). Whereas $U^{\ddagger}$ and $U^{A}$ are the energies of specific points on the zero Kelvin potential energy surface, the internal energy $E$ is an ensemble average of the Hamiltonian at finite temperature. Therefore, the difference $\Delta E$ involves the difference between the ensemble averages of the potential energy at the transition state and the initial state.

If some reaction has a rate determining step, i.e. the barrier of one of the consecutive reaction steps is significantly larger than the other ones, a further approximation can be used for the calculation of the reaction rate constants. In such a case, the reaction can be modeled as a one-step reaction with only one transition state, neglecting stable intermediate states. In this manner we will model a reaction from the most stable geometry of the system (reactant state) to desorbed CO$_2$ (product state) as a one-step reaction when calculating rate constants in the following results section. Therefore, input for a rate constant (energies and vibrational frequencies) comes only from the globally lowest energy minimum and from the highest saddle point along the respective MEP.

## 3.3 Results

### 3.3.1 Computational Setup

For computational reasons, we modeled the Rh(553) surface with a simulation cell containing a single step edge (and thus one terrace) with two atoms along the step edge. Transition states and reaction pathways were first identified using a rhodium slab with four layers parallel to the (111) terrace, of which only the uppermost layer was allowed to relax. After obtaining continuous minimum energy pathways with four layers, the saddle points and minima were recalculated with seven rhodium layers parallel to the (111) terrace, of which the three uppermost layers were fully relaxed. To this end, a quasi-Newton algorithm was used for the recalculation of saddle points and damped molecular dynamics for minima.

For comparison, oxidation of carbon monoxide was also studied on the Rh(111) surface. In order to obtain approximately the same lateral spacing as on Rh(553), we modeled the Rh(111) surface with a $2 \times 4$ surface cell.

Integration of the Brillouin zone was performed with a Gamma-centered $(6 \times 3 \times 1)$ grid for Rh(553) as well as for Rh(111). It should be noted that since the shape of the two Brillouin zones is not identical, numerical integration was not performed fully consistently, which may cause some inaccuracy when comparing energy barriers for these systems. A cutoff energy of 400 eV for the plane wave basis set was used.

### 3.3.2 Reference Structures

The energies of transition states were calculated with respect to the most stable adsorption geometries of CO and, where required, of atomic oxygen on the respective surface. In this respect it should be noted that the energetically preferred CO adsorption site given by DFT with PBE functionals is not in agreement with experiment in the low-coverage limit. While experimentally CO is found to adsorb preferentially on top sites on Rh(111) [39, 40, 41], DFT calculations predict the hcp-hollow site as the most stable adsorption site. For a $2 \times 4$ surface cell, our calculations yield CO adsorption in hcp-hollow sites to be 0.11 eV more stable than in fcc-hollow sites, 0.12 eV more stable than in top sites, and 0.15 eV more stable than adsorption in bridge sites. PBE generally fails to predict the right site preference for CO adsorption on metal surfaces, a problem that has been commonly known as the *CO adsorption puzzle* since the work of Feibelman and coworkers on CO/Pt(111) [42]. Semi-local functionals other than PBE as well as hybrid functionals do hardly offer any improvement [43]. It has been shown recently that the random phase approximation (RPA) to the correlation energy yields adsorption energies in very good agreement with experiment for CO on Pt(111) and Rh(111) and, in particular, predicts the correct adsorption site [44]. However, this method is extremely expensive in terms of computation time, and an extensive investigation of reaction dynamics as done in the present thesis is not yet possible with RPA. It might be an interesting topic for future work to investigate via RPA (or other high level approaches) whether reactions on transition metal surfaces involving carbon monoxide, like those presented in the present chapter, are satisfactorily described by PBE. In a first step this can be achieved by recalculating the energies of transition state geometries obtained from PBE, but in the long run full relaxation with forces from RPA would be desirable.

The conversion of CO in its most stable adsorption site to $CO_2$ involves multiple separate reaction steps. The calculations show that a common initial reaction barrier has to be overcome so that the CO molecule binds to oxygen. In the remainder of this chapter, we will frequently refer to this first relevant energy barrier as the *oxidation barrier*. Note that we investigate a MEP starting with the energy minimum that precedes this barrier, since diffusion barriers between the globally most stable state, which we consider as the reactant state, and the minimum preceding the oxidation barrier can be assumed to be rather small and thus do not affect the reaction rates. Furthermore, we will refer to the final barrier, which has to be overcome so that $CO_2$ actually desorbs from the surface, as the *desorption barrier*. The energy difference between the highest saddle point along the MEP and the reactant state is called the *overall barrier*, assuming that the highest saddle point determines the overall rate, as discussed above.

### 3.3.3 Oxidation of CO on Rh(111)

Fig. 3.2 shows the minimum energy path for the CO oxidation on the Rh(111) surface. The first transition state (Fig. 3.2 (a)) corresponds to a structure where the oxygen atom is activated from the hollow site to an adjacent bridge site and the CO molecule is moved slightly away from the ideal top site towards the O atom. With an energy barrier of 1.42 eV it is the highest saddle point on the potential energy surface for this transition path and hence determines the transition rate. In the subsequent intermediate state, the CO molecule and the atomic oxygen move closer towards each other (Fig. 3.2 (b)). The minimum energy path continues with a second transition state and a subsequent intermediate state, where the $CO_2$ complex tilts from an hcp-hollow position involving three rhodium atoms to a bridge-like position involving two rhodium atoms (Fig. 3.2 (c)). The third transition state (Fig. 3.2 (d)) corresponds to the desorption barrier. The O-C-O angle at this transition state is 157 degree and increases to 180 degree in the final stable state of the path, where the $CO_2$ is in the gas phase state (Fig. 3.2 (e)). The potential energy $U$ of the structures was calculated with respect to p$(2 \times 4)$ CO adsorbed in hcp-hollow (energy $U_{\mathrm{CO}}$), p$(2 \times 4)$ O adsorbed in fcc-hollow (energy $U_{\mathrm{O}}$), and the bare rhodium slab (energy $U_{\mathrm{Rh}}$) as $U = U_{\mathrm{tot}} - U_{\mathrm{CO}} - U_{\mathrm{O}} + U_{\mathrm{Rh}}$, where $U_{\mathrm{tot}}$ is the total potential energy of the simulation cell.

An equivalent reaction was found to occur also in an fcc-hollow position, with an overall barrier of 1.48 eV and thus slightly larger than for the reaction in hcp-hollow described above.

### 3.3.4 Oxidation of CO on $NiO_2$/Rh(553)

**Initial Oxidation**

For the $NiO_2$/Rh(553) surface, the oxidation of CO with chemisorbed oxygen on the terrace as shown in Fig. 3.3 is very similar to oxidation on the Rh(111) surface. The geometry of the $CO_2$ complex in the first (and rate determining) transition state of the reaction (Fig. 3.3 (a)) is virtually identical to the geometry of the first transition state on Rh(111) (Fig. 3.2 (a)). Yet the correspondent energy barrier is 1.29 eV on $NiO_2$/Rh(553) and thus smaller than on Rh(111) (1.48 eV for reaction in fcc-hollow and 1.42 eV in hcp-hollow). It should be noted that there are several inequivalent hollow sites on the terraces of the stepped $NiO_2$/Rh(553) surface at which this reaction as shown in Fig. 3.3 might occur, but we did not investigate all of these possibilities. Therefore, we can not exclude that the barrier for CO oxidation at one of these sites is lower than 1.29 eV. Nevertheless, oxidation of CO with atomic oxygen on the terraces seems to occur with a smaller energy barrier than on Rh(111).

Initial oxidation of CO at the $NiO_2$ nanowires is conceivable at both the

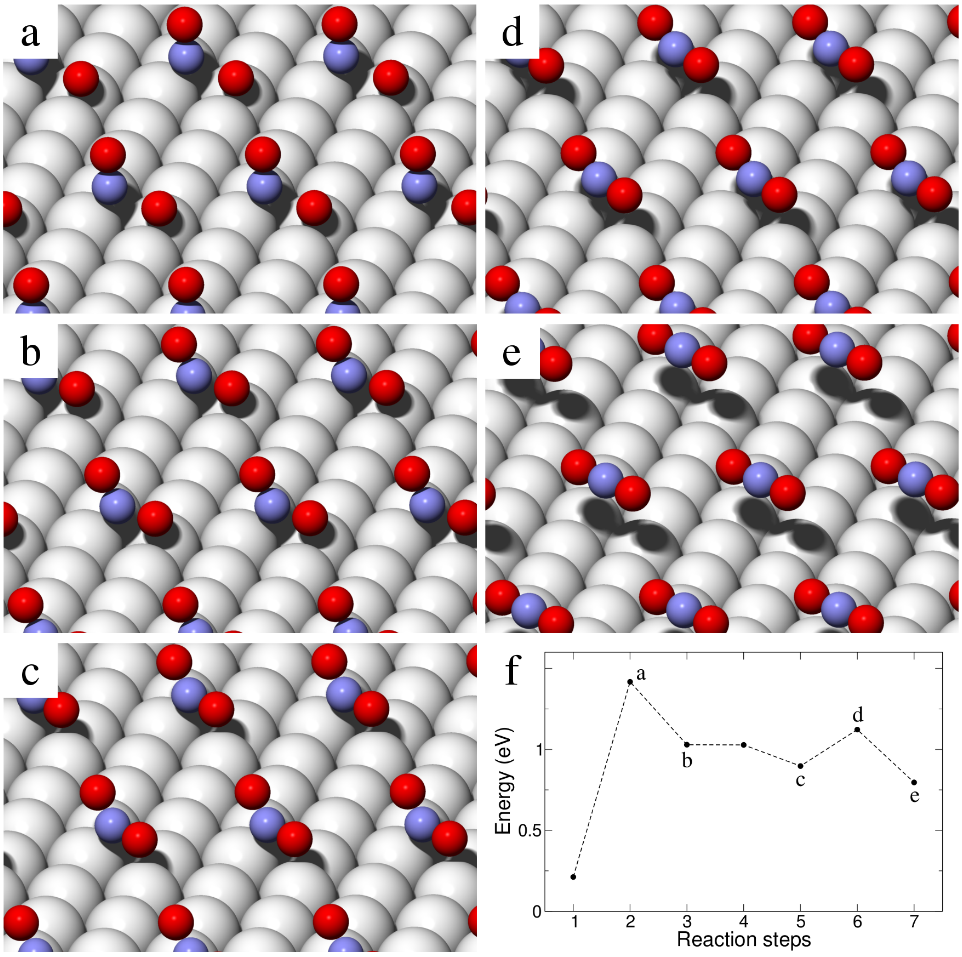

Figure 3.2: CO oxidation with atomic oxygen on Rh(111): (a) Transition state of the oxidation barrier (1.42 eV); (b) First intermediate state which is very close to the second transition state (1.03 eV); (c) Second intermediate state; (d) Transition state of the desorption barrier (1.12 eV); (e) $CO_2$ desorbed; (f) Energy diagram.

lower and the upper oxygen rows. We found that the oxygens at the lower row are considerably more reactive. The transition path with the smallest overall barrier is shown in Fig. 3.4. The reference state (energy zero) is the CO molecule adsorbed in an hcp-hollow site as shown in Fig. 3.4 (a), which turns out to be the most stable adsorption site for CO, according to the PBE functional. The stable state preceding the oxidation barrier is CO adsorbed in a top site near the $NiO_2$ stripe (not shown). Starting from this, the reaction consists of five transition states and accordingly four intermediate states. The first step of the transition is characterized by the carbon atom approaching an oxygen atom in the lower row of the nickel oxide, and the

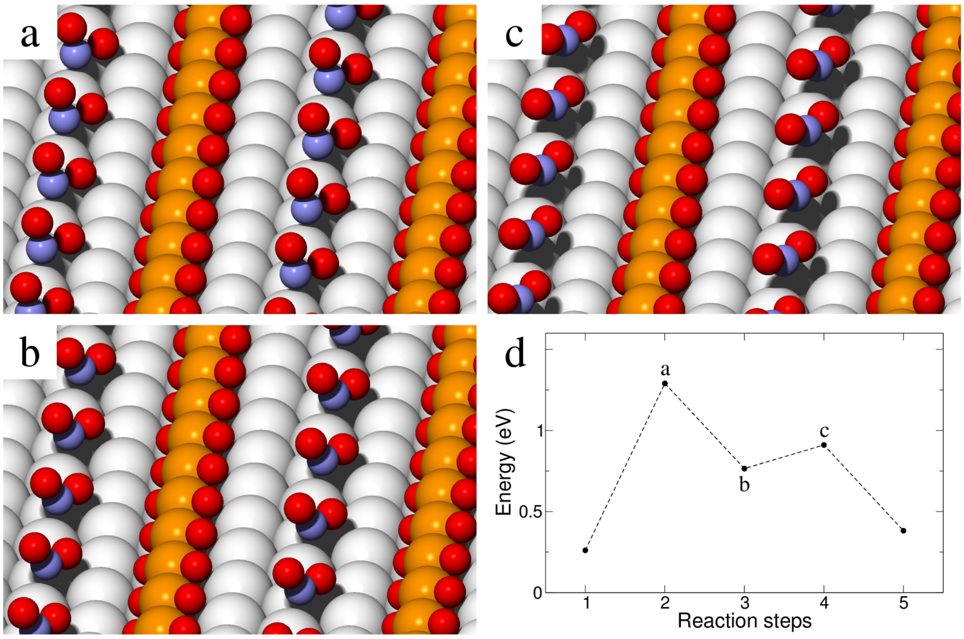

Figure 3.3: CO oxidation with atomic oxygen on the terraces of NiO$_2$/Rh(553): (a) Transition state of the oxidation barrier (1.29 eV); (b) Intermediate state; (c) Transition state of the desorption barrier (0.91 eV); (d) Energy diagram.

according energy barrier is due to bond formation between these atoms. The distance between the carbon and the oxygen in the NiO$_2$ stripe is 1.64 Å in the transition state (Fig. 3.4 (b)) and 1.45 Å in the subsequent intermediate state. Since this distance is 2.92 Å in the stable state preceding the barrier (CO in top), the transition state can be characterized as a late transition state. The next reaction step is a tilting of the CO$_2$ complex with an energy barrier of 1.05 eV (Fig. 3.4 (c)) before, in the subsequent steps, the bonds between the oxygen atom and the nickel atoms are broken (not shown). The final step is the desorption process where bonds between the CO$_2$ complex and the rhodium atoms are broken and the CO$_2$ stretches to form a linear molecule. The O-C-O angle is 150 degree in the transition state (Fig. 3.4 (d)) and 180 degree in the final gas phase state (Fig. 3.4 (e)).

Compared to CO oxidation at the lower oxygen rows of the NiO$_2$ stripes, initial oxidation at the upper oxygen rows is energetically less favorable. The appropriate transition path for this reaction consists of two transition states according to a first reaction step, viz. the oxidation of CO, and a second step - the desorption of CO$_2$. The oxidation barrier of 1.28 eV (Fig. 3.5 (a)) is significantly higher as compared to oxidation at the lower oxygen rows (0.93 eV, Fig. 3.4 (b)). The same applies to the desorption barrier of 1.32 eV (Fig. 3.5 (c)) compared to 0.96 eV (Fig. 3.4 (d)). Initial oxidation of CO is

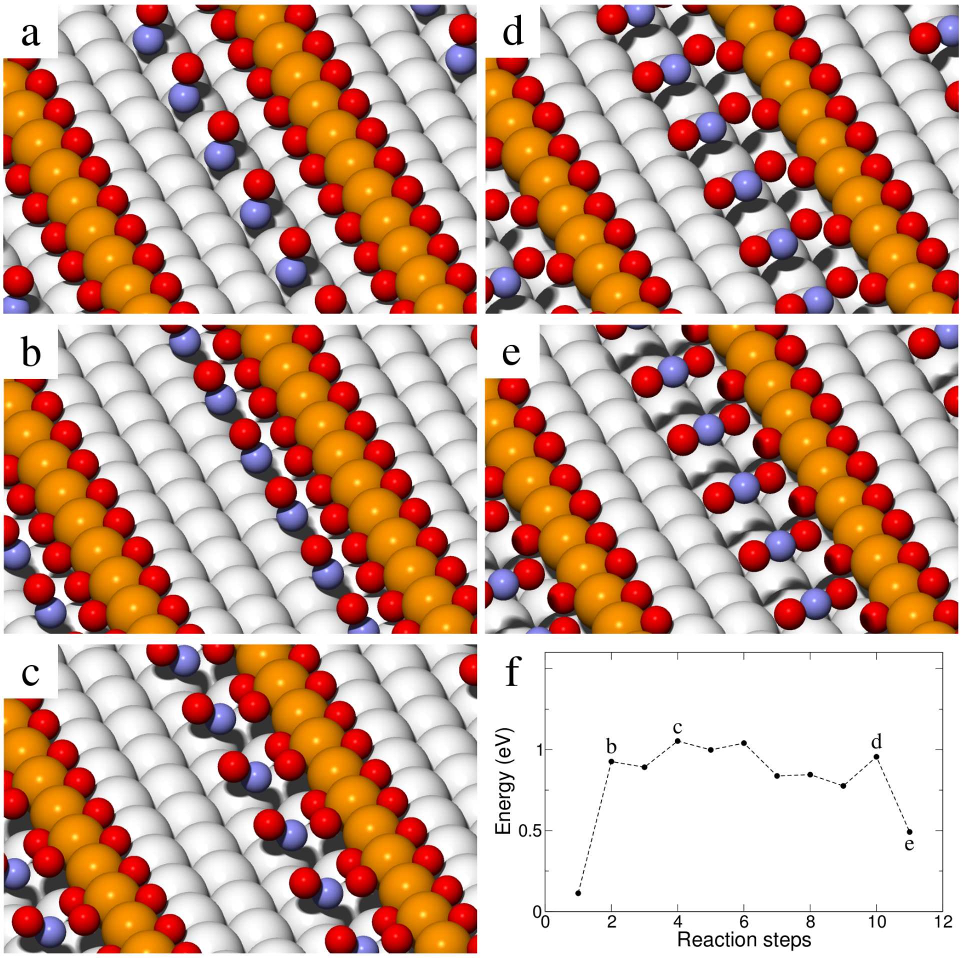

Figure 3.4: Initial CO oxidation at the lower oxygen rows of the quasi-one-dimensional nickel oxide stripes on Rh(553): (a) CO in hcp-hollow (0 eV); (b) Transition state of the oxidation barrier (0.93 eV); (c) Transition state of the largest energy barrier of this reaction path (1.05 eV); (d) Transition state of the desorption barrier (0.96 eV); (e) $CO_2$ desorbed (0.49 eV); (f) Energy diagram.

thus more likely to happen at the lower oxygen rows with an overall energy barrier of 1.05 eV than at the upper rows with an overall barrier of 1.32 eV or on the terrace with an overall barrier of 1.29 eV.

### Further Oxidation Steps

We also investigated how further oxidation of CO takes place after oxygens have been removed from the lower oxygen rows, leaving nickel oxide stripes as shown in Fig. 3.4 (e). Given the periodicity of our simulation cell con-

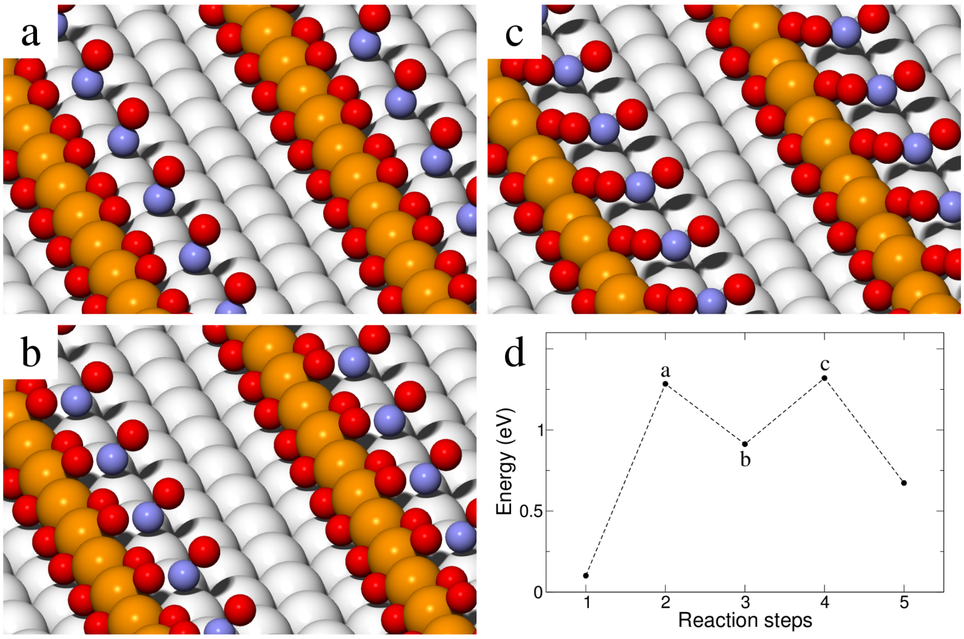

Figure 3.5: Initial CO oxidation at the upper oxygen rows of the quasi-one-dimensional nickel oxide stripes on Rh(553): (a) Transition state of the oxidation barrier (1.28 eV); (b) Intermediate state; (c) Transition state of the desorption barrier (1.32 eV); (d) Energy diagram.

taining two nickel atoms, three possible scenarios were considered. One of these is again a reaction of CO with oxygen of the lower row, which results in a complete removal of the lower oxygen row while leaving the upper oxygen row unchanged. The minimum energy path for this scenario is sketched in Fig. 3.6. It consists of three transition states and the overall barrier of 0.90 eV is even smaller than for the initial oxidation with 1.05 eV. The energetically most favorable structure, relative to which the transition state energies are evaluated, is again CO adsorbed in an hcp-hollow site (not shown).

After we had found this reaction path we tried to adopt it for the initial oxidation step at the full oxygen covered nickel oxide stripe in order to lower the overall energy barrier from 1.05 eV to likewise 0.90 eV. This undertaking was not successful. Several attempts with quasi-Newton and the dimer method were made. However, despite careful preparation of the structure to resemble the transition state in Fig. 3.6 (b) with a fully occupied lower oxygen row, in each attempt the system moved away from the corresponding region in configuration space, indicating that no transition state was nearby. It seems that with the lower oxygen row of the oxide stripe being fully occupied, a reaction path similar to the one in Fig. 3.6 does not exist.

Fig. 3.7 shows the other two possible scenarios where, after initial oxidation

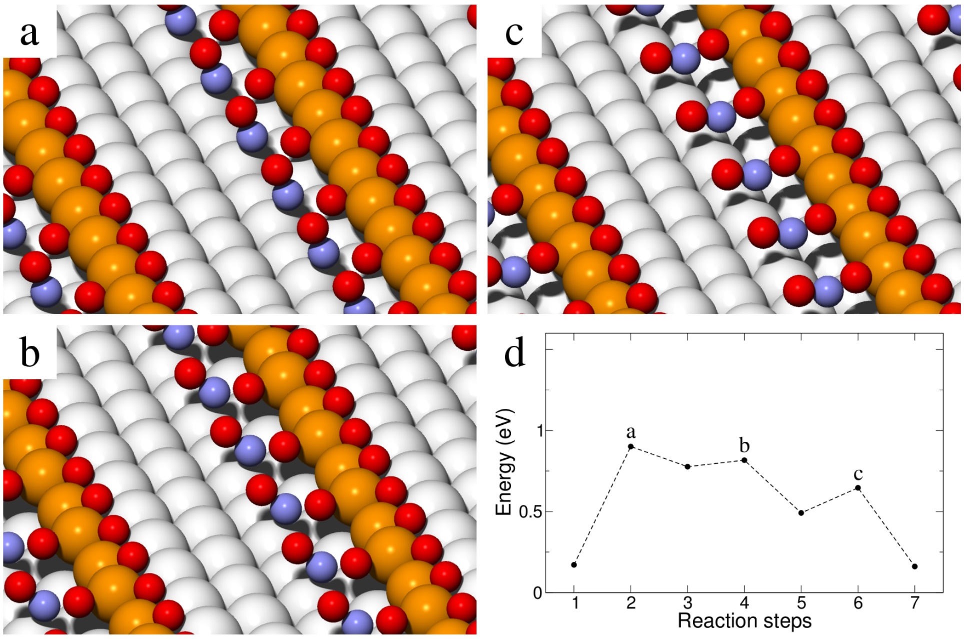

Figure 3.6: Further removal of oxygen at the nickel oxide stripe after initial oxidation: (a) Transition state of the oxidation barrier (0.90 eV); (b) Second transition state (0.82 eV); (c) Transition state of the desorption barrier (0.65 eV); (d) Energy diagram.

at the lower oxygen row, further oxidation occurs at the upper row. Since in both cases already the first transition state is energetically very unfavorable, we did not search for further transition states of these reactions. The overall energy barrier is in each case at the least as high as the energy of the first saddle point (1.56 eV and 1.30 eV, respectively) and hence much larger than for oxidation at the lower oxygen row with an overall barrier of only 0.90 eV.

### Rearrangements of the NiO Stripes

The oxidation reactions as shown in Figures 3.4 and 3.6, discarding possible readsorption of atomic oxygen into the nickel oxide, leave NiO stripes with oxygen only at the upper row (Fig. 3.8 (a)). However, for this stoichiometry a zigzag arrangement of the oxygen atoms is more stable by about 0.07 eV per oxygen atom (Fig. 3.8 (c)). Since the energy barrier for a proper rearrangement is as low as 0.58 eV (Fig. 3.8 (b)), the zigzag phase is likely to be established immediately after a sufficient number of atoms of the lower oxygen row have been removed by oxidation. An arrangement with full oxygen content at the lower row and no oxygen atoms at the upper row (not shown) is about 0.37 eV per oxygen atom less stable than the zigzag phase.

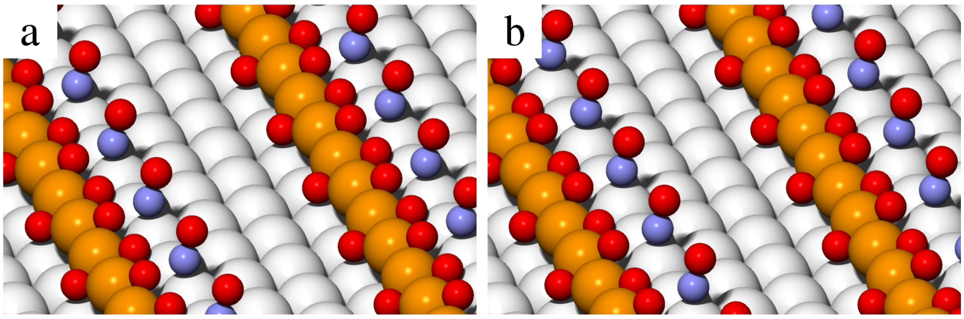

Figure 3.7: CO oxidation at the upper oxygen row of a nickel oxide stripe after initial oxidation at the lower oxygen row: (a) The overall energy barrier for reaction of CO with the oxygen atom opposite to the empty site in the lower row is at least 1.56 eV. (b) Removal of the oxygen atom in the upper row opposite to the oxygen atom in the lower row yields a NiO zigzag structure. The overall barrier for this reaction is at least 1.30 eV.

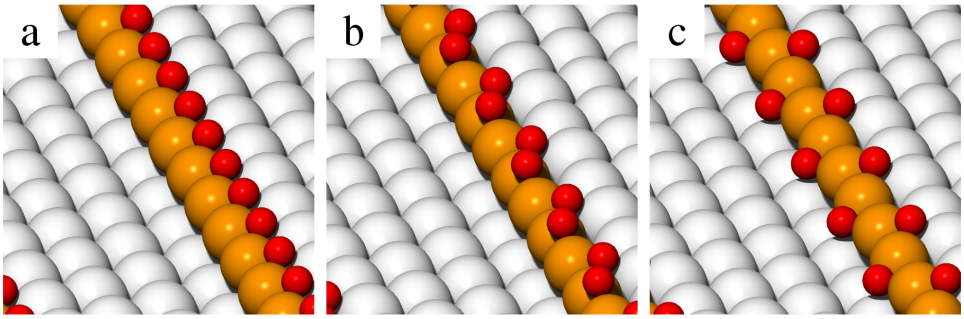

Figure 3.8: Starting with nickel oxide stripes with full oxygen content (Fig. 3.1 (b)), the most favorable CO oxidation reaction (see Figures 3.4 and 3.6) establishes stripes as shown in (a). However, at zero temperature, the zigzag phase in (c) is about 0.07 eV per oxygen atom more stable than the phase in (a). The energy barrier for the transition from (a) to (c) is only 0.58 eV, the corresponding transition state is shown in (b).

The establishment of the zigzag stripes is also possible by initial oxidation at the lower oxygen row followed by a suitable reaction at the upper oxygen row (Fig. 3.7 (b)). With an overall energy barrier of at least 1.30 eV, this is of course a possible scenario and may occasionally happen as temperatures become sufficiently high. Yet, removal of oxygen from only the lower row and subsequent displacement of atoms of the upper oxygen row in order to build the zigzag arrangement is more likely to occur, since the barriers for this reaction sequence are significantly lower.

CO oxidation at the NiO zigzag stripes occurs probably at a lower rate than the preceding reactions. The oxidation barrier is 1.11 eV at the lower oxygen row (Fig. 3.9 (a)) and 1.47 eV at the upper row (Fig. 3.9 (b)). We did not

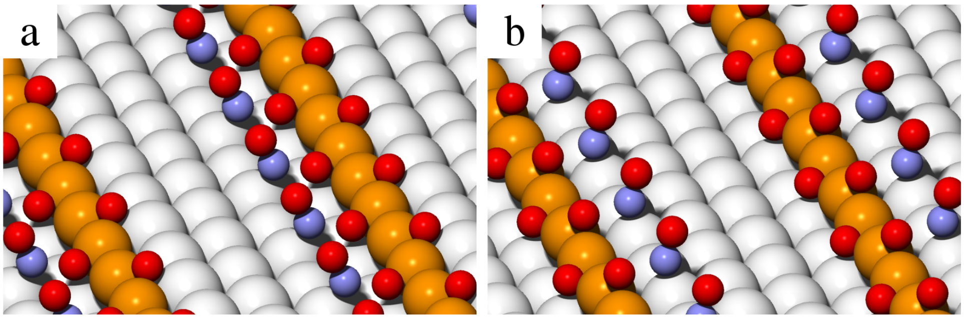

Figure 3.9: CO oxidation at NiO zigzag stripes: Transition state of the oxidation barrier for reaction at (a) the lower oxygen row (1.11 eV) and (b) the upper oxygen row (1.47 eV).

search for subsequent transition states.

### High Coverage

So far we have restricted our attention to the case of low coverage with only one CO molecule in the simulation cell. Since our theoretical study aims to find atomistic models for experiments in which a large amount of CO is initially adsorbed on the surface at 90 K before oxidation reactions are initiated by heating to elevated temperatures [13], our investigations would ideally be done with additional CO molecules in the simulation cell to describe reactions occurring in experiment at low temperatures. The low-coverage case on the contrary applies at high temperatures of about 400 K, where only a small amount of CO is left on the surface. However, performing an extensive study of the high-coverage case was not possible within the framework of this thesis. Nevertheless, some basic questions were examined.

The structure relative to which the reaction barriers for initial oxidation have been calculated was carbon monoxide adsorbed in an hcp-hollow site (Fig. 3.10 (a)), since this is the most stable configuration according to PBE. The adsorption energy of CO in this adsorption site decreases from $-1.76$ eV to $-1.41$ eV, i.e. by 0.35 eV, if additional CO molecules adsorb on the terrace as shown in Fig. 3.10 (b). This shows that the binding of carbon monoxide to the substrate becomes weaker as the coverage increases. As a consequence, reaction barriers for a particular molecule become lower if the transition state geometries and the respective energies are not significantly affected by the other CO molecules. However, it can not be ruled out that the latter is the case.

Consistently with the investigations of the low-coverage case, reaction barriers for higher coverage should be calculated with respect to the most stable adsorption structure. The energetically most favorable configura-

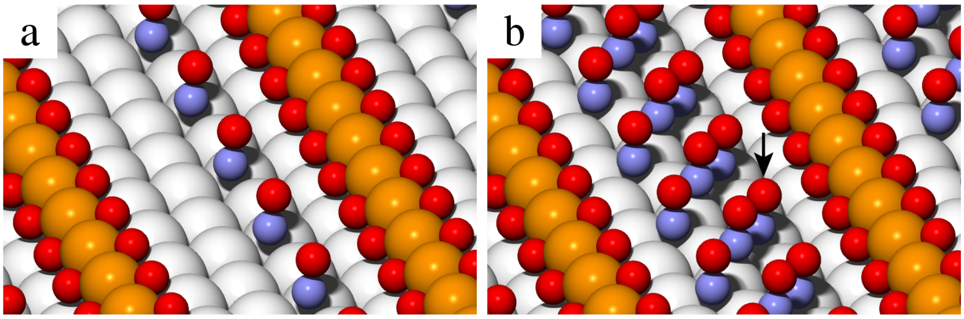

Figure 3.10: (a) Carbon monoxide in its most stable adsorption position (hcp-hollow), according to PBE, where the simulation cell contains only one CO molecule. Reaction barriers for initial CO oxidation were calculated relative to this structure. (b) In the presence of additional CO molecules (one CO in fcc-hollow and one CO in a top site), the adsorption energy of CO in hcp-hollow (same as in (a), marked by a black arrow) decreases by 0.35 eV.

tion for three CO molecules in the simulation cell is shown in Fig. 3.11 (a). This structure was found by applying simulated annealing starting from 800 Kelvin, a temperature at which carbon monoxide is sufficiently mobile on the rhodium terraces. The molecule closest to the lower oxygen row of the nickel oxide stripe and hence the one to undergo a reaction is now adsorbed in a top site, in contrast to the low-coverage case, where the reacting CO is adsorbed in the hcp-hollow site (Fig. 3.10 (a)). The geometry of the reacting $CO_2$ complex in the transition state of the oxidation barrier (Fig. 3.11 (b)) is very similar to the transition state geometry in the low-coverage case (Fig. 3.4 (b)). The height of the oxidation barrier in the high-coverage case is only 0.64 eV (with respect to the most stable adsorption structure in Fig. 3.11 (a)), whereas it was 0.93 eV in the low-coverage case (with respect to the most stable adsorption structure in Fig. 3.10 (a)). If we calculate this barrier for low coverage not with respect to the most stable structure, but with respect to CO adsorbed in the same top site as considered for high coverage, we obtain a value of 0.81 eV. Either way, increasing the coverage results in a lower oxidation barrier for initial oxidation at the lower oxygen rows of the nickel oxide stripes. More transition states for the high-coverage case, providing a whole reaction pathway from adsorbed CO to desorbed $CO_2$, could not be investigated in the present thesis.

### 3.3.5 Oxidation of CO on bare Rh(553)

For comparison we also investigated CO oxidation at oxidized step edges of Rh(553) as shown in Fig. 3.12. The results provide further confirmation that nickel oxide nanowires enhance the reactivity for CO oxidation. The

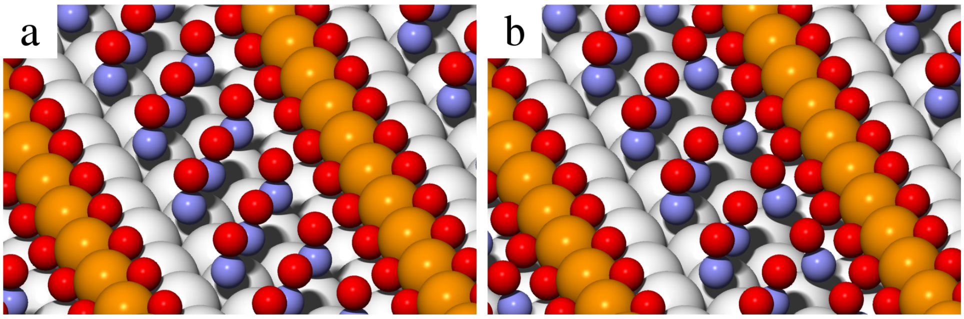

Figure 3.11: (a) Most stable structure for three CO molecules in the simulation cell as found by employing simulated annealing. The CO molecule closest to the nickel oxide stripe is adsorbed in a top site. (b) Transition state of the oxidation barrier for the CO molecule closest to the oxide stripe reacting with oxygen of the lower oxygen row. This transition state is to be compared with the transition state in Fig. 3.4 (b). Whereas the oxidation barrier is 0.93 eV with one CO molecule in the simulation cell, it is only 0.64 eV in the presence of the additional CO molecules.

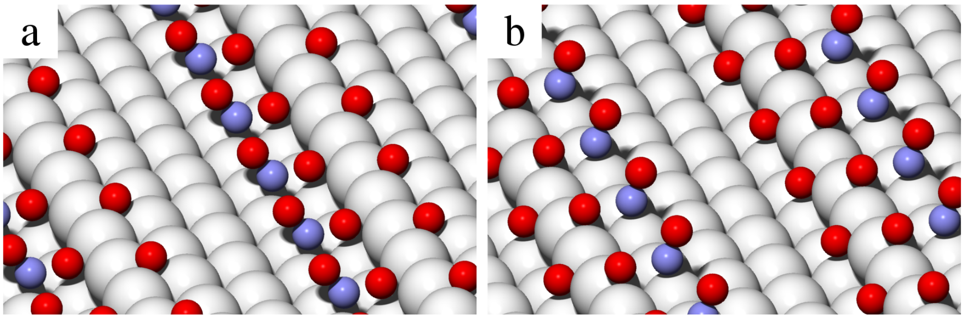

Figure 3.12: CO oxidation at rhodium oxides on the Rh(553) surface: Transition state of the oxidation barrier for reaction at (a) the lower oxygen row (1.22 eV) and (b) the upper oxygen row (1.46 eV).

oxidation barrier at the lower oxygen row is 1.22 eV and thus slightly larger than 1.11 eV for the zigzag nickel oxide. However, experimentally the step edges of the bare Rh(553) surface can not be oxidized exclusively as it can be done with a row of nickel atoms at the rhodium steps. On bare Rh(553), oxygen adsorption is more favorable on the terrace than at the lower step edge, and the zigzag arrangement of oxygen atoms at the step as shown in Fig. 3.12 can only be grown in coexistence with a local p(2 ×1) structure on the terrace [45]. Hence the reactions in Fig. 3.12 are merely model reactions that are not of particular interest for experiment.

| | $\nu^*(150\,\mathrm{K})$ | $\nu^*(320\,\mathrm{K})$ | $\nu^*(420\,\mathrm{K})$ | $\nu^{**}$ |
|---|---|---|---|---|
| **Rh(111)** | $2.7 \times 10^{12}$ | $4.5 \times 10^{12}$ | $5.0 \times 10^{12}$ | $6.2 \times 10^{12}$ |
| **$\mathbf{NiO_2}$/Rh(553)** | | | | |
| lower oxygen | $7.5 \times 10^{13}$ | $7.3 \times 10^{13}$ | $7.3 \times 10^{13}$ | $6.8 \times 10^{13}$ |
| upper oxygen | $3.8 \times 10^{15}$ | $4.8 \times 10^{15}$ | $5.5 \times 10^{15}$ | $7.7 \times 10^{15}$ |
| oxygen on terrace | $2.5 \times 10^{13}$ | $3.0 \times 10^{13}$ | $3.2 \times 10^{13}$ | $3.8 \times 10^{13}$ |
| **$\mathbf{NiO_{2-x}}$/Rh(553)** | | | | |
| lower oxygen | $2.4 \times 10^{13}$ | $2.5 \times 10^{13}$ | $2.5 \times 10^{13}$ | $2.7 \times 10^{13}$ |

Table 3.1: Effective frequency $\nu^*(T)$ (in $s^{-1}$) as defined in equation (3.16) for three different temperatures, where the partition functions were calculated according to (3.18) and (3.19). The column on the very right shows the values of the classical limit $\nu^{**}$ as defined in (3.23). The transitions for which these frequencies (and the rate constants, see Table 3.2) have been calculated are the oxidation of CO and subsequent desorption of $CO_2$ on Rh(111) (Fig. 3.2), on $NiO_2$/Rh(553) ('lower oxygen': Fig. 3.4; 'upper oxygen': Fig. 3.5; 'oxygen on terrace': Fig. 3.3), and on $NiO_{2-x}$/Rh(553) (Fig. 3.6). This table shows that for each transition the effective frequency varies insignificantly with temperature and that the classical limit $\nu^{**}$ is an acceptable approximation.

### 3.3.6 Reaction Rate Constants

We calculated reaction rate constants for five of the reaction mechanisms discussed above, namely the oxidation of CO with atomic oxygen on Rh(111), cf. Fig. 3.2, the three possibilities for initial oxidation on $NiO_2$/Rh(553), cf. Figures 3.3, 3.4 and 3.5, and oxidation at the already reduced lower oxygen rows of the oxide stripes as shown in Fig. 3.6. We evaluated these rates at the experimentally relevant temperatures of 150 K, 320 K, and 420 K. The rates are determined not only by the height of the energy barrier that has to be surmounted, but also by the vibrational partition functions of the initial and the transition state, see equation (3.15). These partition functions yield a temperature dependent effective frequency, or prefactor, $\nu^*(T)$, as defined in (3.16). The values of this prefactor are given in Table 3.1, which clearly shows that at the specified temperatures, for each of the five reactions, $\nu^*(T)$ does not deviate much from $\nu^{**}$, which is the value of the prefactor in the classical limit $\beta h\nu \ll 1$.

The reaction rate constants resulting from the prefactors of Table 3.1 are shown in Table 3.2. The reaction of CO at the lower oxygen rows of the nickel oxide stripes is definitely the most favorable mechanism for initial oxidation. However, the table also shows that differences in the energy barriers of different reactions become less important with increasing temperature.

| | $U^{\ddagger} - U^{A}$ | 150 K | 320 K | 420 K |
|---|---|---|---|---|
| **Rh(111)** | 1.42 | $6.4 \times 10^{-36}$ | $2.1 \times 10^{-10}$ | $4.9 \times 10^{-5}$ |
| **$\mathbf{NiO_2}$/Rh(553)** | | | | |
| lower oxygen | 1.05 | $3.1 \times 10^{-22}$ | $1.9 \times 10^{-3}$ | $1.7 \times 10^{1}$ |
| upper oxygen | 1.32 | $1.7 \times 10^{-29}$ | $7.9 \times 10^{-6}$ | $8.0 \times 10^{-1}$ |
| oxygen on terrace | 1.29 | $1.1 \times 10^{-30}$ | $1.4 \times 10^{-7}$ | $1.0 \times 10^{-2}$ |
| **$\mathbf{NiO_{2-x}}$/Rh(553)** | | | | |
| lower oxygen | 0.90 | $1.3 \times 10^{-17}$ | $1.6 \times 10^{-1}$ | $3.9 \times 10^{2}$ |

Table 3.2: Reaction rate constants (per CO molecule) according to harmonic TST (in $s^{-1}$), calculated by employing (3.18), (3.19), and (3.15), for three different temperatures, and the respective energy barriers (in eV) on the zero Kelvin potential energy surface.

Whereas the highest and the lowest rate constant for initial oxidation of CO at $NiO_2$/Rh(553), viz. the rate constant of the reaction at the lower oxygen row of the nickel oxide stripe and the rate constant of the reaction on the terrace, deviate by a factor of about $10^8$ at a temperature of 150 K, this deviation decreases to a factor of approximately $10^3$ at 420 K.

The rate constants in Table 3.2 were calculated using equations (3.18), (3.19), and (3.15). Yet, it turns out that also the simpler formula (3.22) suffices in case of the transitions investigated here, although the condition $\beta h\nu \ll 1$ is not fulfilled. This is due to the fact that the effective frequencies (3.16) for these transitions do not vary significantly with temperature, as can be seen from Table 3.1. Using equation (3.22), the rate constants in Table 3.2 merely change by factors between 1.1 and 2.4 at a temperature of 150 K, and by factors between 1.1 and 1.4 at 420 K, which is absolutely negligible.

It is noticeable that the prefactor for initial CO oxidation at the upper oxygen rows is of the order of $10^{15}\,s^{-1}$, whereas the prefactors for the other reactions are of the order of $10^{13}$ or $10^{12}\,s^{-1}$. A constant prefactor of $10^{13}\,s^{-1}$ is often used in literature if no information about this quantity is available. This is due to the fact that the frequencies of the vibrational modes are typically of the order of $10^{12}$ to $10^{13}\,s^{-1}$. According to equation (3.23), the product of the frequencies of some stable state is divided through the product of the frequencies of some transition state in order to obtain the effective frequency. If the initial state of the reaction and the rate determining transition state are similar as it is the case for an *early transition state*, it is to be expected that the vibrational frequencies are similar as well, so that all frequencies in (3.23) cancel each other except one remaining frequency in the numerator, since there is one frequency more in the numerator than in the denominator. The prefactor would then ideally be that one frequency, which, as indicated above, is typically of the order of $10^{13}\,\mathrm{s}^{-1}$. As an example, consider the reaction of CO with atomic oxygen on the terraces of $NiO_2$/Rh(553) (Fig. 3.3), with $\nu^{**} \approx 10^{13}\,\mathrm{s}^{-1}$ (cf. Table 3.1). For this reaction, the rate is determined by the transition state of the oxidation barrier (cf. energy diagram in Fig. 3.3 (d)), which can be regarded as an early transition state. Here, 'early' means that the transition state rather resembles the adsorbed CO molecule than the desorbed $CO_2$. In contrast, in case of CO oxidation at the upper oxygen rows of the $NiO_2$ stripes (Fig. 3.5), the rate is determined by the transition state of the desorption barrier (cf. energy diagram in Fig. 3.5 (d)). This saddle point for the transition into the gas phase is definitely a *late transition state*, which means that it is much closer to the product state (desorbed $CO_2$) than to the reactant state and hence in general fairly different from the latter, which may amongst other things be expressed in sizeable differences in the vibrational frequencies. In such a case, cancellation of frequencies in (3.23) is not accomplished as well as for an early transition state and the prefactor may deviate significantly from the popular value of $10^{13}\,\mathrm{s}^{-1}$, as it is observed for this reaction where $\nu^{**} = 7.7 \times 10^{15}\,\mathrm{s}^{-1}$.

It is worth noting that in kinetic Monte Carlo simulations of temperature programmed desorption of oxygen from Rh(111), which will be reported in Chapter 4, we had to use a frequency prefactor of $2 \times 10^{15}\,\mathrm{s}^{-1}$ in order to yield good agreement with experiment. Considering the example we have just described, where we have assumed the rate to be determined solely by the transition state of a desorption process, it is perfectly understandable that the prefactor may generally be of such a high value for associative desorption.

Table 3.2 shows that although the energy barrier for oxidation at the upper oxygen rows on $NiO_2$/Rh(553) with a value of 1.32 eV is larger than the barrier of 1.29 eV for oxidation on the terraces, the former reaction is slightly favored, as expressed by the higher rate constants at all temperatures, because of a significantly higher effective frequency. However, concerning the particular case of CO oxidation at the upper oxygen rows, it can be seen from the energy diagram in Fig. 3.5 (d) that for this reaction the oxidation barrier is only slightly lower than the desorption barrier and modeling the whole process as a one-step reaction discarding the stable intermediate state may not yield a good value for the rate constant, especially at elevated temperatures, where differences in energy barriers become less important. Hence the rate constants for this reaction may be lower than the values we have reported in Table 3.2.

Some important remarks about the energy barriers and rate constants given in Table 3.2 should be made. The rate constants we have calculated for 150 K are most likely too low compared with experiment, which is primarily due to the use of only one CO in the simulation cell and the inaccuracy of DFT. Using PBE potentials, DFT overestimates the adsorption energies of

CO on rhodium by at least 0.2 eV [44]. Therefore, assuming that the energies of the various transition states calculated with DFT are more accurate than these adsorption energies (it is not known whether this is the case), the reaction barriers are too high, since these barriers are evaluated as energy differences between transition states and states in which CO is adsorbed in hollow sites. Lowering the energy barrier for initial oxidation of CO at the lower oxygen rows of the $NiO_2$ stripes (Fig. 3.4) from 1.05 eV to 0.85 eV increases the rate constant at 150 K from about $10^{-22}\,s^{-1}$ to about $10^{-15}\,s^{-1}$, i.e. by seven orders of magnitude, whereas it is only increased by two orders of magnitude at 420 K. The second reason why the rate constants at 150 K are too low is that also for this temperature we have used data from the low-coverage case. However, experimental core-level spectra indicate that CO oxidation only sets in at about 150 K [13], consequently the full amount of CO initially adsorbed on the surface is still present at this temperature. We have shown in section 3.3.4 that increasing the coverage causes a considerably weaker binding of a certain CO molecule that is about to undergo some reaction. Summarized, both the PBE potentials and the use of only one CO molecule in the simulation cell cause the adsorption energies of CO on rhodium to be significantly overestimated, which most likely also results in an overestimation of activation barriers. Especially at low temperatures this yields rate constants that are too low by several orders of magnitude.

## 3.4 Summary

We have investigated the catalytic activity of quasi-one-dimensional nickel oxide nanowires for the oxidation of carbon monoxide and the subsequent desorption of carbon dioxide. These nanowires of formal $NiO_2$ stoichiometry can be grown at the step edges of the Rh(553) surface. The methods applied to identify reaction paths comprise the nudged elastic band, the dimer method, and quasi-Newton algorithms. Structure candidates for transition states were tested by calculating the vibrational modes and frequencies via the Hessian matrix, and by careful relaxation from transition states along minimum energy paths. Energy barriers and vibrational frequencies were used to evaluate reaction rate constants according to transition state theory.

We studied reaction processes at the lower and upper oxygen row of the oxide stripe and on the terrace of the $NiO_2$-Rh(553) surface, as well as on Rh(111) and on bare Rh(553) for comparison. Our results clearly show that the nickel oxide stripes enhance the activity for CO oxidation and subsequent $CO_2$ desorption. The reaction with the smallest overall barrier and the highest reaction rate constant occurs at the lower oxygen rows of the $NiO_2$ stripes. The energy barrier for reaction of CO with oxygen of the already partially unoccupied lower oxygen row is even lower (and the rate constants higher) than for the initial reaction at the fully occupied oxygen rows.

We have shown that if in a reaction sequence of oxidation and desorption processes the desorption barrier is rate determining, a prefactor of the order of $10^{15}\,\mathrm{s}^{-1}$ can apply, which is significantly higher than the value of $10^{13}\,\mathrm{s}^{-1}$ commonly used in literature. This result presumably holds generally for associative desorption of chemisorbed atoms or molecules, since for this kind of reaction the transition state very much differs from the reactant state. We will use this conclusion in Chapter 4, in which we report on kinetic Monte Carlo simulations of temperature programed desorption of oxygen from Rh(111).

# Chapter 4

# Kinetic Monte Carlo Simulations of Temperature Programed Desorption of O/Rh(111)

## 4.1 Introduction

Whereas in Chapter 3 we identified particular reaction processes and calculated their rate constants, in the present chapter we address the question of how an atomic system with multiple competing reactions evolves in time. As a model case, we simulated a *temperature programed desorption* (TPD) experiment for oxygen on the Rh(111) surface. In this experiment, an adsorbate layer of atomic oxygen is prepared on the metal substrate. Subsequently, associative desorption is induced by heating, and the $O_2$ desorption rate as a function of temperature is determined.

The simulation of TPD experiments allows to analyze the interactions between the adsorbates, and also provides a test for the approximations (such as DFT) used in the calculations. Agreement between the simulated TPD spectra and the experimental spectra indicates that the adsorbate-substrate and adsorbate-adsorbate interactions most likely are described properly. Accordingly, our simulations provide a test for the quality of adsorption- and interaction energies evaluated with PBE potentials. The inverse conclusion, however, does not apply. Unsatisfactory agreement of the spectra is not necessarily due to a bad model for the interactions, but can also result from an incomplete catalog of competing processes or inaccurate rate constants.

As described in the following sections, we use a multi-site *lattice gas model* and construct an effective Hamiltonian for the lateral interactions from DFT calculations. This Hamiltonian is used to calculate rate constants which enter the *kinetic Monte Carlo* procedure in order to simulate the time evolution

of the system.
The following results have been published in a similar (but less detailed) form in

T. Franz, F. Mittendorfer, *Kinetic Monte Carlo simulations of temperature programed desorption of O/Rh(111), J. Chem. Phys. 132, 194701 (2010).*

## 4.2 Kinetic Monte Carlo

The problem of rare events, for which an explicit Molecular Dynamics simulation on the DFT level is usually not feasible, has already been discussed in section 3.2.1. Note that energy barriers for the associative desorption of oxygen are even considerably larger (at least twice as large) than the barriers we have found in Chapter 3 for oxidation of CO and desorption of $CO_2$. In order to calculate TPD spectra, we need to simulate a huge number of desorption events on a macroscopic timescale. If there is sufficient knowledge about which reactions are possible and what their rate constants are, kinetic Monte Carlo (kMC) [46, 47] is the method of choice to accomplish this task.
With kMC the state-to-state dynamics of an atomic system is simulated as a Markov walk (transition probabilities independent of history). Here, the term 'state' does not refer to an individual geometry of the system, but all geometries within a particular basin on the potential energy surface constitute one state. Consequently, the state changes only if the system passes a transition state, that is, a dividing surface. At first sight it seems surprising that the time evolution of a system can be simulated as a stochastic process, since according to Newtonian mechanics a trajectory in phase space is deterministic. However, when integrating Newtons equations of motion (Molecular Dynamics), usually some random initial conditions need to be assigned which determine the trajectory for all time. Without knowledge of the initial conditions and the exact trajectory, it is reasonable to assume that the system will leave a particular energy basin on the PES to some other basin with a probability proportional to the rate constant of the respective transition. Performing a large number of kMC and MD simulations, both methods will yield the same probability distribution of state-to-state sequences. In this manner, kMC can give the exact time evolution on a macroscopic time scale, provided that all transition paths and rate constants are known.
The major drawback of the kMC method is that it requires the complete set of reaction pathways and the corresponding rate constants as input. One way to calculate these quantities is to apply transition state theory, as discussed in section 3.2.6, where the rate constant for a transition from state $i$ to state $j$ has the form (cf. (3.15))

$$k_{ij} = \nu \exp[-\beta \, \Delta E_{ij}^{\mathrm{TS}}], \tag{4.1}$$

where $\Delta E_{ij}^{\mathrm{TS}}$ is the energy difference between the transition state (that connects states $i$ and $j$) and the minimum of state $i$, at zero temperature. If there are no translational and rotational contributions to the partition functions in the transition state and in state $i$, as it was the case for the reactions studied in Chapter 3, then the (temperature dependent) prefactor $\nu$ is obtained from the vibrational partition functions via (3.16).

Once all pathways out of state $i$ and the rate constants $\{k_{ij}\}$ are known, it is straightforward to employ kMC. A uniformly distributed random number $\xi$ is drawn on the interval $[0, 1)$. The transition from state $i$ to state $m$ is selected if

$$\sum_{j=0}^{m-1} k_{ij} \leq k_i \, \xi < \sum_{j=0}^{m} k_{ij}, \tag{4.2}$$

where $k_{i0} := 0$ and $k_i := \sum_j k_{ij}$. This guarantees that every transition is selected with a probability proportional to the respective rate constant. With the escape from state $i$, independent of which transition is chosen, the system time is incremented by $1/k_i$ [48, 49]. This procedure is repeated for the new state, with a new set of rate constants.

It should be emphasized that kMC is only exact if the rate catalog is complete. This requires that all possible reactions are known.

## 4.3 Desorption Processes of Oxygen on Rh(111)

Fig. 4.1 shows the energy profiles of two particular minimum energy pathways for the associative desorption of two oxygen atoms. The corresponding calculations were performed with a $(3 \times 3)$ surface cell, a slab of four layers of rhodium, a Gamma-centered $(9 \times 9 \times 1)$ k-point mesh for the primitive $(1 \times 1)$ cell, and a cutoff energy of 282.8 eV.

The reaction takes place via a hollow-type intermediate state (upper left inset in Fig. 4.1 (a)), after which the $O_2$ straightens up atop a rhodium atom (right inset) and lifts off. Alternatively, the system can move from the hollow-type intermediate state to a bridge-type intermediate state (inset in Fig. 4.1 (b)) and subsequently desorb in a very similar manner as in the other case. The transition states connecting the state of dissociated oxygen atoms (lower inset in Fig. 4.1 (a)) and the two intermediate states were found with NEB and quasi-Newton algorithms. The second part of the path which connects one of the intermediate states with the gas phase state, however, can be found with simple relaxation alone, for the following reason. The profiles in Fig. 4.1 clearly show that for the second part of the path the energy increases monotonically, and the transition state coincides with the final state. As for any other transition state, we carried out relaxation with the $O_2$ molecule initially placed quite far away from the rhodium slab so that the forces acting on the molecule are almost zero (as it is generally the case

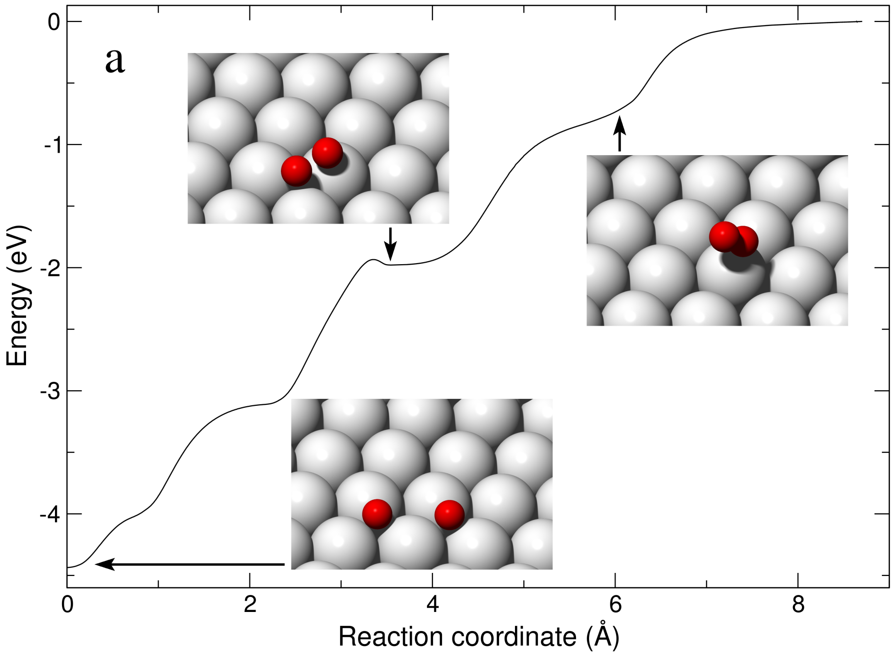

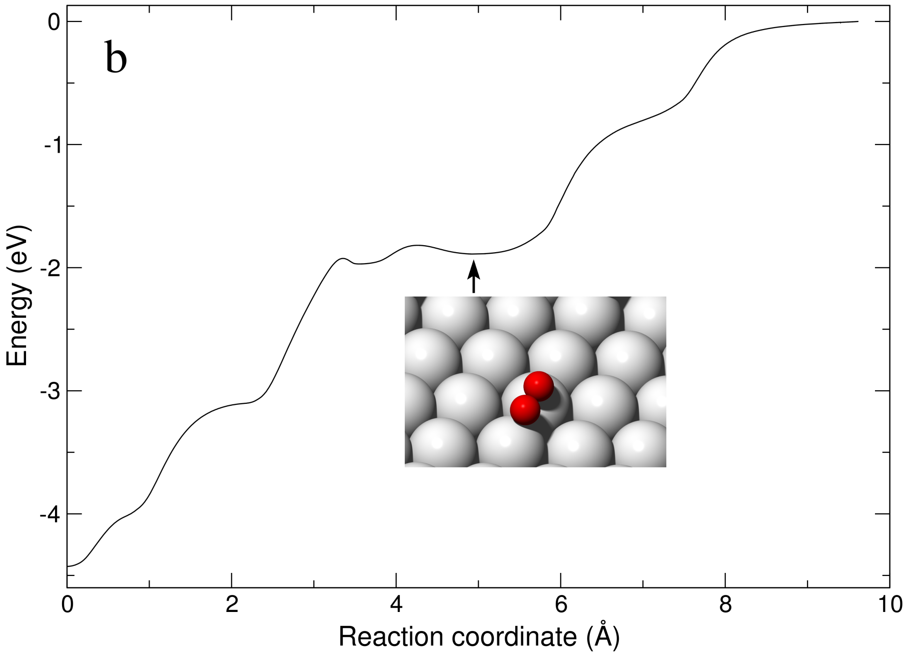

Figure 4.1: Energy profiles of minimum energy paths for the associative desorption of oxygen: (a) Reaction with one intermediate state; (b) Reaction with two intermediate states.

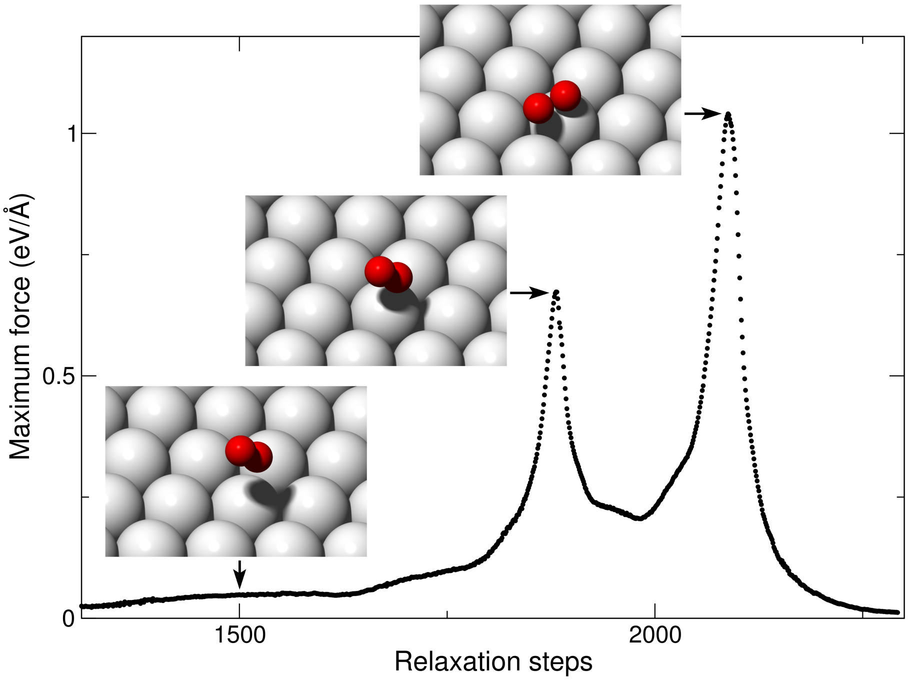

Figure 4.2: Maximum force in the system in the course of a damped MD relaxation from the $O_2$ gas phase state into the hollow-type intermediate state (upper left inset in Fig. 4.1 (a)). Typical for relaxation from a transition state, the force is almost zero at the beginning of the relaxation, increases to fairly large values and tends again to zero towards the end.

in the vicinity of a transition state). Using damped Molecular Dynamics with very small relaxation steps, we can expect the system to follow (in good approximation) a minimum energy path. Fig. 4.2 shows the largest force acting on any of the atoms in the system as the relaxation from the gas phase state to the hollow-type intermediate state is conducted. Typical for relaxations from transition states along minimum energy pathways, this force is vanishingly small at the beginning of the calculation and reaches a maximum in the course of the relaxation before it tends to zero again. Note that this behavior is entirely different if a bad initial guess for some structure is optimized, in which case the forces are in general quite large at the beginning of the relaxation and (in most cases) decrease monotonically.

We note that the procedure of applying the NEB method would result in the very same relaxation as shown here. Setting up the band with one of the intermediate states as the first image, we would place the $O_2$ molecule somewhere in the vacuum where the forces are vanishing to obtain the last image of the band. No matter where exactly we put the molecule in the vacuum, the NEB calculation would in any case yield a monotonically increasing energy profile, which consequently requires subsequent relaxation from the very last image of the band in order to map the minimum energy path. Hence an explicit NEB calculation is not needed.

We performed multiple relaxations starting in the gas phase with various initial conditions. In each attempt, the system relaxed into the hollow-type or the bridge-type intermediate state. Direct dissociative adsorption without an intermediate state (and an additional small energy barrier) was not found. Also, we did not succeed in finding such a path applying the dimer method or the nudged elastic band starting from the dissociated state (lower inset in Fig. 4.1 (a)).

Due to the very small barrier for the inverse transition from an intermediate state to the initial state (dissociated atoms), the second step of the associative desorption which leads from an intermediate state to the gas phase is definitely rate determining, and in the kMC simulations the whole process of associative desorption can be simulated as one single step.

The essential conclusion that can be drawn from the energy profiles is that, since there is no activation barrier for adsorption, the activation energy for desorption equals the effective adsorption energy $E^{\mathrm{ads}}$ of the oxygen molecule, including the lateral interactions in case of additional atoms in the local environment on the surface. However, the prefactor and the rate constant for desorption can not be calculated within the framework of harmonic transition state theory, as it was performed in Chapter 3, since in the transition state, which equals the gas phase state, rotations and translations of the molecule are no longer frustrated. Hence the prefactor can not be calculated from the vibrational partition functions alone as in (3.16). Nevertheless, we use for the rate constant the empirical Arrhenius equation

$$k = \nu \exp[\beta\, E^{\mathrm{ads}}], \tag{4.3}$$

where $E^{\mathrm{ads}}$ is negative. This equation is formally identical to (4.1), but in contrast to the latter the prefactor $\nu$ in (4.3) can not be calculated via formula (3.16).

Related to the fact that in the gas phase state rotations and translations contribute to the partition function is the question of how strong the prefactors and rate constants for $O_2$ desorption vary with temperature. In the case of the reactions involving CO as discussed in Chapter 3, all the transition states, even for $CO_2$ desorption, were chemisorbed states in which translations and rotations are frustrated. We found that for those reactions the prefactors and rate constants hardly depend on temperature. In the case of $O_2$ desorption, however, the prefactors depend not only on chemisorbed states but also on the gas phase state in which translations and rotations are not frustrated. Hence it can be expected that the prefactors and the

| Adsorption site | Energy (eV) | Type |
|---|---|---|
| fcc-hollow | -2.119 | minimum |
| hcp-hollow | -2.020 | minimum |
| bridge | -1.594 | saddle point |
| top | -0.591 | maximum |

Table 4.1: Adsorption energies of an isolated oxygen atom in the high symmetry adsorption sites of the Rh(111) surface.

rate constants for $O_2$ desorption from Rh(111) vary considerably with temperature.

Furthermore, an explicit prefactor and rate constant should be calculated for each single desorption event. This is due to the fact that, because of lateral interactions, the occupation of adsorption sites in the local environment influences the vibrational modes and the vibrational partition function in the dissociated state of the oxygen atoms. Consequently, even if harmonic TST could be applied, an exact calculation of every single prefactor for the huge number of different reactions we encounter in the course of a kMC simulation would not be feasible.

In the present work the prefactor was assumed to be constant, i.e. independent of both temperature and the local environment on the rhodium surface.

## 4.4 Diffusion Events

At zero temperature, an isolated atom adsorbs in high symmetry sites. In case of Rh(111), high symmetry sites are fcc-hollow, hcp-hollow, top, and bridge. Our results for the adsorption energies of an oxygen atom in these sites are listed in Table 4.1. The corresponding calculations were performed with a single oxygen atom in a $(6 \times 6)$ surface cell (yielding a minimum distance between oxygen atoms of 16.3 Å), six rhodium layers, and a Gamma-centered $(24 \times 24 \times 1)$ k-point mesh for the primitive $(1 \times 1)$ cell.

The fcc-hollow and the hcp-hollow sites are stable sites where the fcc-hollow site is about 0.1 eV more favorable than the hcp-hollow site.

The bridge site with an energy of about 0.5 eV higher than the fcc-hollow site is the transition state of the minimum energy path connecting an fcc-hollow and a neighboring hcp-hollow site.

The top site is also unstable with a value of more than 1.5 eV higher than the fcc-hollow site. It is an energetic maximum with respect to surface diffusion, which means that from the ideal top site an oxygen atom gains energy along all in-plane directions. This does of course not mean that this point on the PES is a maximum along all possible degrees of freedom.

The barrier of 0.5 eV for diffusion from fcc-hollow over bridge to hcp-hollow is much lower than the barrier for associative desorption of more than 4 eV. Consequently, the diffusion rates are orders of magnitudes higher than the desorption rates in this system, and a full kMC simulation would mainly sample the diffusion events on the surface. Yet the high diffusion rate also implies that after every desorption event the system returns to thermal equilibrium before the next desorption event occurs. Therefore we have chosen a procedure where only the desorption events are treated in the kMC framework [48, 49], whereas the system is equilibrated after each desorption event using the Metropolis algorithm [50].

## 4.5 Lattice Gas Model

To describe different configurations of chemisorbed oxygen atoms on the Rh(111) surface, we employed a *lattice gas model*. By constructing an effective parametrization of interactions, such a model allows to avoid the explicit DFT calculation of each single configuration in the course of the Monte Carlo simulations.

As discussed in the previous section, the oxygen atoms adsorb in high symmetry sites which form a regular lattice. However, in case of multiple atoms the adsorption positions in general deviate from the high symmetry sites due to lateral interactions. Furthermore, at elevated temperatures, atoms do not reside in their ground state positions but can move considerably away from the latter. At temperatures high enough, also the geometry of the topmost substrate layer may be distorted in which case high symmetry sites can no longer be defined. Applying a lattice gas model, each adsorption position is mapped to the nearest high symmetry adsorption site of the ideal substrate geometry at zero temperature. In this manner, each atom at any time is considered to occupy the (zero Kelvin) high symmetry site which is closest to its real position. Because of the instability of the bridge and top sites (Table 4.1), we only have to take account of fcc-hollow and hcp-hollow sites in our lattice gas model.

This is in agreement with experiment. It is widely known that chemisorbed oxygen on the Rh(111) surface forms a $p(2 \times 2)$ structure at a coverage of 1/4 ML (1 ML = 1 adsorbate atom per substrate atom of the topmost layer) and a $p(2 \times 1)$ structure at a coverage of 1/2 ML, and that in both phases the oxygen atoms reside in the threefold fcc-hollow sites [51, 52]. For a coverage of 2/3 ML a $(2\sqrt{3} \times 2\sqrt{3})R30°$ structure was found with oxygen atoms adsorbed in fcc- and hcp-hollow sites [53]. Fig. 4.3 shows models of all three phases. At even higher coverages, a surface oxide has been observed, but its formation is kinetically hindered and occurs only at temperatures above 800K [54]. As we are aiming to describe the desorption of oxygen from adsorbate covered surfaces that have been prepared at significantly lower

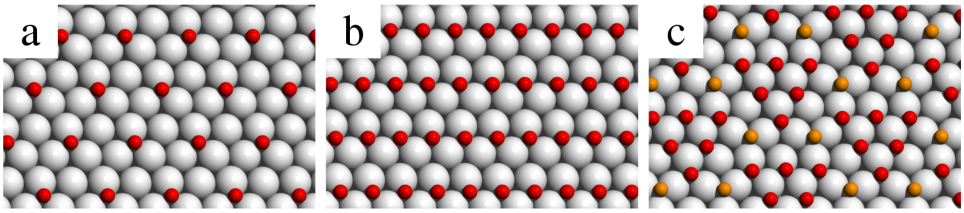

Figure 4.3: Schematic representation of the experimentally observed adsorption structures of oxygen on Rh(111): (a) p(2×2) structure at a coverage of 1/4 ML; (b) p(2 × 1) structure at a coverage of 1/2 ML; (c) $(2\sqrt{3}\times2\sqrt{3})R30°$ structure at a coverage of 2/3 ML. Red balls indicate oxygen atoms in fcc-hollow sites, yellow balls in hcp-hollow sites.

temperatures, we did not include this phase in our model. Therefore, due to the experimentally observed structures as sketched in Fig. 4.3, application of a multi-site lattice gas model which takes account of both fcc- and hcp-hollow sites is required in order to describe oxygen chemisorption on Rh(111) at different coverages.

The shortest distance between two hollow sites on the resulting lattice is 1.57 Å (in case of rhodium with a lattice constant of 3.84 Å). However, two oxygen atoms adsorbed in these sites, as shown in Fig. 4.4 (a), experience very strong repulsion and thus such configurations are energetically very unfavorable. Preparing two oxygen atoms in these high symmetry sites and performing relaxation, the distance between the oxygens increases from 1.57 Å to 2.39 Å (not shown). Calculated in a (3 × 3) surface cell, the energy of the fully relaxed structure is 1.11 eV higher than of the likewise relaxed reference structure of two oxygens in neighboring fcc-hollow sites (cf. Fig. 4.4 (b)). This is a huge energy difference, even at temperatures of up to 1400 K that we are concerned with in the present study: the acceptance probability for an energy gain of 1.11 eV at 1400 K in the Metropolis Monte Carlo simulations is $10^{-4}$. Thus, it is highly unlikely that a structure with an atom in an fcc-hollow site and another atom in one of the nearest hcp-hollow sites will ever be accepted. Consequently, the occurrence of such structures can safely be excluded, which simplifies the parametrization of the configurational energies considerably.

It might be objected that due to the large energy difference of 1.11 eV, which implies a transition barrier that is at least as high as this value, this particular diffusion event, like the desorption events, needs to be treated in the framework of kinetic Monte Carlo and not with the Metropolis algorithm. We have examined the minimum energy path for this transition from two oxygen atoms in adjacent fcc-hollow sites (Fig. 4.4 (b)) into the unfavorable state in question (Fig. 4.4 (a)). Since identifying transition states and minimum energy paths is computationally very demanding, we performed these calculations in a (3 × 3) surface cell with 4 layers of rhodium and a

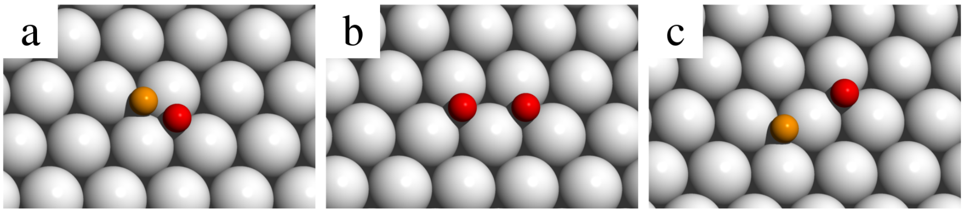

Figure 4.4: Three pairs of oxygen atoms in ideal adsorption sites (not relaxed): (a) Due to strong repulsion, occupation of an fcc-hollow site together with one of its nearest neighboring hcp-hollow sites is energetically very unfavorable and thus excluded in our lattice gas model. (b) In our model, nearest neighboring oxygen atoms occupy either nearest neighboring fcc-hollow sites (as shown here) or nearest neighboring hcp-hollow sites (not shown). (c) Second-nearest neighbors according to our model.

Gamma-centered $(18 \times 18 \times 1)$ k-point mesh for the primitive $(1 \times 1)$ cell. The energy profile of this transition is shown in Fig. 4.5 (a). Fig. 4.5 (b) displays a magnification of the very right part of this profile. The barrier for the reverse transition is only about 7 meV and hence negligible at relevant temperatures. Consequently, the state which corresponds to the right end of the energy curve is virtually unstable and the system will not spend a significant amount of time in this state, which means that there is no need for treating this state within the framework of kinetic Monte Carlo.

In summary, a system state with two oxygen atoms adsorbed in an fcc-hollow site and one of its nearest neighboring hcp-hollow sites (Fig. 4.4 (a)) is practically unstable at temperatures of interest. That is why we exclude such states from our lattice gas model and thus nearest neighbors in this model are oxygen atoms occupying either nearest neighboring fcc-hollow sites (Fig. 4.4 (b)) or nearest neighboring hcp-hollow sites (not shown). Second nearest neighbors are shown in Fig. 4.4 (c).

## 4.6 Parametrization

### 4.6.1 Lattice Gas Hamiltonian

In the kMC simulations of temperature programed desorption, each time after the system of adsorbed oxygen atoms has been equilibrated using the Metropolis algorithm, all pairs of oxygen atoms are examined. The question of which desorption pathways do exist and hence for which pairs of atoms in the lattice gas a desorption rate needs to be added to the rate catalog is a crucial point for the kMC simulations. An incomplete rate catalog can result in a wrong time evolution of the system.

We have shown in section 4.3 that a pathway for associative desorption definitely exists for nearest neighbors in fcc-hollow sites. A similar pathway

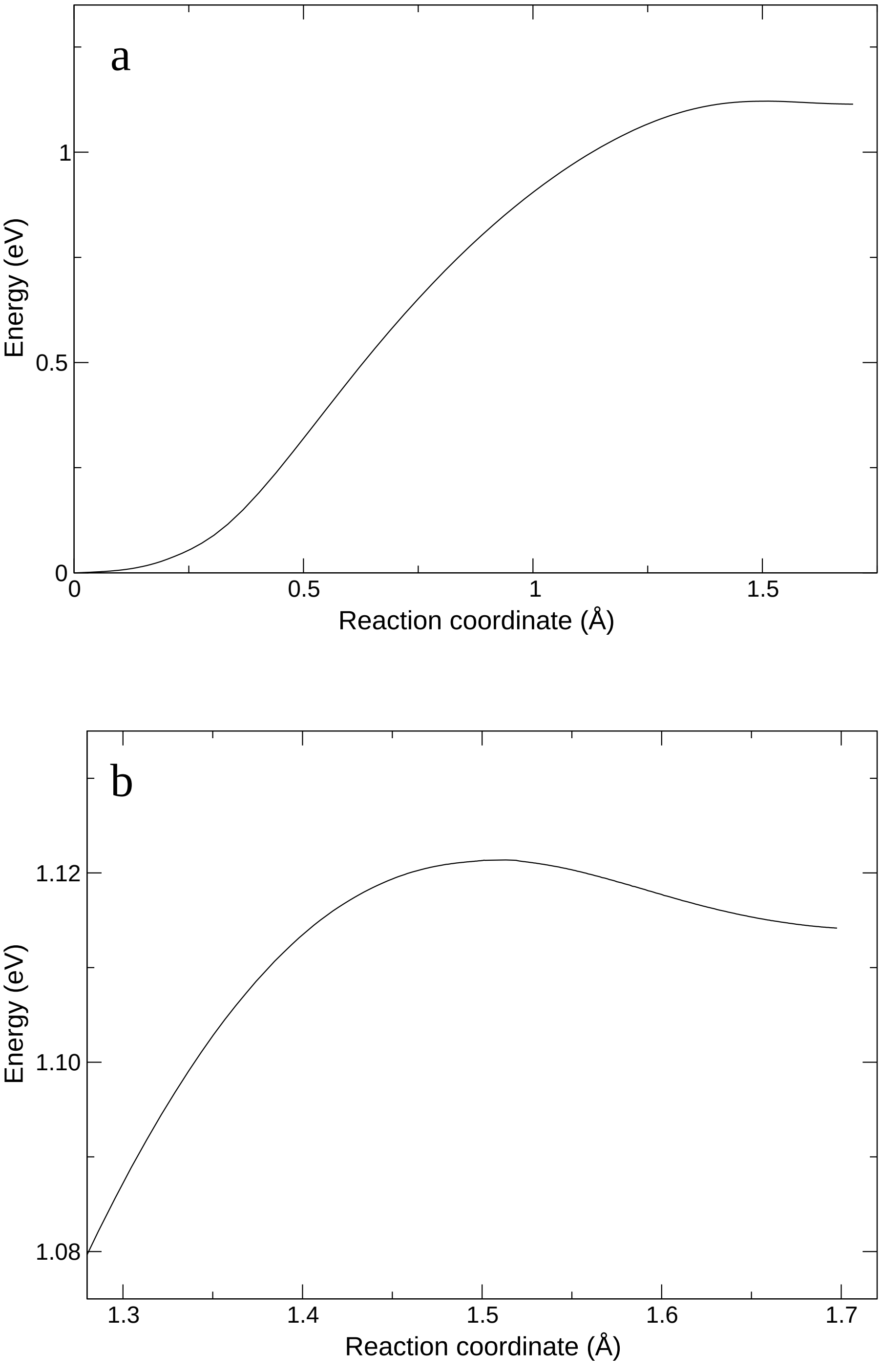

Figure 4.5: (a) Energy profile of two oxygen atoms occupying nearest neighboring fcc-hollow sites (Fig. 4.4 (b)) switching to the occupation of an fcc-hollow site together with one of its nearest neighboring hcp-hollow sites (Fig. 4.4 (a)). (b) Magnification of the very right part of the energy profile.

presumably exists for nearest neighbors in hcp-hollow sites. It seems that a rhodium atom of the topmost layer plays an important part for the association process of the oxygens. Therefore, we assume that a path also exists for second nearest neighbors (Fig. 4.4 (c)), since they are located next to the same rhodium atom as it is the case for nearest neighbors.

Accordingly, we calculate rate constants of desorption for nearest and second nearest neighbors to establish the rate catalog. If the adsorption energy of a single oxygen atom is calculated with respect to one half of the energy of an isolated $O_2$ molecule in vacuum, then the adsorption energy $E^{\text{ads}}$ of a particular pair of oxygen atoms, which is needed in order to calculate the rate constant (4.3), is given by the adsorption energy of the whole oxygen layer including both atoms minus the adsorption energy of the layer with those two atoms being removed. For this purpose, we write the adsorption energy of a configuration of particles on the surface as

$$\begin{aligned} E = \sum_i E_i \quad & + \quad \frac{1}{2}\sum_{ij}(p_{1,ij}\,P_1 + p_{2,ij}\,P_2 + \dots) \\ & + \quad \frac{1}{3}\sum_{ijk}(t_{1,ijk}\,T_1 + t_{2,ijk}\,T_2 + \dots) \\ & + \quad \dots\,. \end{aligned} \tag{4.4}$$

An expansion of this form is known as *lattice gas Hamiltonian* (LGH) [55]. All sums run over the adsorbed particles in the system. $E_i$ is the adsorption energy of an isolated particle occupying either an fcc-hollow or an hcp-hollow site, so there are only two possible values for $E_i$. The coefficients $\{\{P_n\}, \{T_n\}, \dots\}$ are effective interaction parameters (EIPs). Each EIP is associated with a so called figure, which is an arrangement of particles in high symmetry adsorption sites, according to the lattice gas model. The effective pair interactions $\{P_n\}$ are associated with figures consisting of two oxygen atoms, the effective trio interactions $\{T_n\}$ are associated with figures consisting of three oxygen atoms etc. Examples of figures are shown in Fig. 4.6. In our lattice gas model, each adsorbed oxygen atom occupies the high symmetry hollow site which is closest to its real position. With the double sum $\sum_{ij}$ in (4.4) all pairs of atoms in these high symmetry adsorption sites are considered. The coefficient $p_{n,ij}$ equals 1 if particles $i$ and $j$ form the figure that the EIP $P_n$ is associated with, and 0 otherwise. With the three sums $\sum_{ijk}$ all trios of oxygen atoms are considered etc.

It should be noted that in literature the LGH is often written in a different form using sums that run over adsorption sites and occupation numbers which equal either 0 or 1. However, we chose the form (4.4) because it better reflects our particular implementation.

In general, multiple figures might be equivalent due to the symmetry of the surface. For example, Fig. 4.6 (a) shows an element of a set of three figures

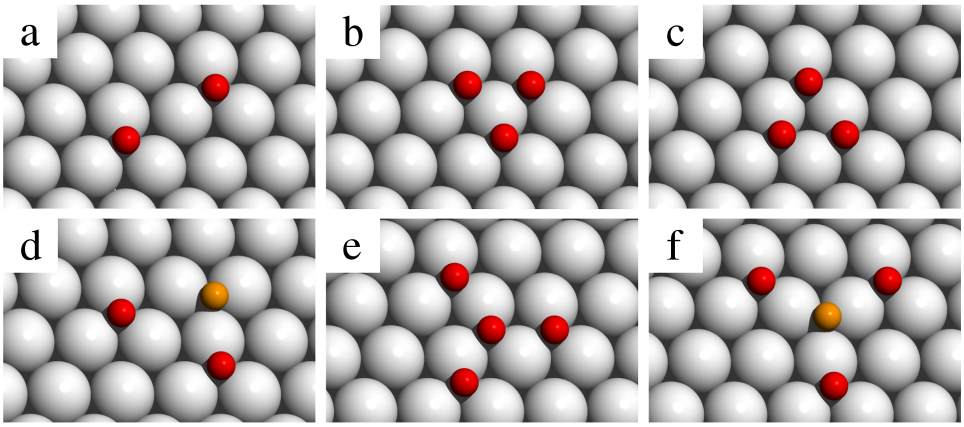

Figure 4.6: Examples of figures that the effective interaction parameters are associated with: (a) Effective pair interactions are related to figures consisting of two oxygen atoms. (b)-(d) Effective trio interactions are related to figures consisting of three oxygen atoms. (e), (f) Effective quattro interactions are related to figures consisting of four oxygen atoms.

that are equivalent by rotational symmetry, whereas Fig. 4.6 (f) shows the only element of its set. Note that the figures in (b) and (c) are not equivalent, although in both cases the distances between the three atoms are the same in the lattice gas model. The atoms in (b) are arranged around a top site, whereas the atoms in (c) are arranged around a hollow site. Performing relaxation, the oxygen atoms in (b) relax from the center of mass towards the outward bridge sites, whereas the oxygen atoms in (c) relax towards the adjacent top sites. Our DFT calculations show an energy difference between the fully relaxed structures of 170 meV, thus the two figures can not be associated with the same effective trio interaction.

### 4.6.2 Cross Validation

To construct the LGH, i.e. determine the optimal set of EIPs in (4.4), we applied the procedure of (leave-one-out) *cross validation* [56], which has already been used for the characterization of oxygen adsorbed on other transition metals [57, 58]. In order to perform cross validation, a set of configurations of adsorbed atoms (like e.g. the structures in Fig. 4.3) is calculated with DFT and used as input for the procedure. For a set of $M$ input configurations, the *cross validation score* is defined as [56, 57]

$$\mathrm{CV} = \left\{ M^{-1} \sum_{i=1}^{M} \left[ E^{\mathrm{DFT}}(i) - E^{\mathrm{LGH}}(i) \right]^2 \right\}^{1/2} . \tag{4.5}$$

Here, $E^{\mathrm{DFT}}(i)$ is the energy per adsorbed atom of configuration $i$ obtained from DFT, and $E^{\mathrm{LGH}}(i)$ is the energy per adsorbed atom of configuration $i$

calculated via (4.4), where the set of EIPs used in the LGH is determined by a least-squares fit to all input configurations except configuration $i$. The cross validation score is considered to be the mean absolute error for configurations which were not included in the set of input configurations, and hence the set of EIPs that yields the lowest CV is the optimal choice for the lattice gas Hamiltonian.

To determine the relevant structures that are needed as input for cross validation, an iterative scheme is used where new important configurations predicted by the LGH are calculated with DFT and added to the set of input configurations, before (4.5) is evaluated anew [57]. For this purpose, it is appropriate to use *formation energy* plots. For an arbitrary configuration, the formation energy is defined as [57]

$$\Delta E_f := \Theta(E_{\text{conf}} - E_{(1\times1)}), \tag{4.6}$$

where $\Theta$ is the coverage of the configuration (in ML as defined above), $E_{\text{conf}}$ is the energy per adsorbed oxygen atom of the configuration, and $E_{(1\times1)}$ is the energy per adsorbed oxygen atom of the p$(1 \times 1)$ structure (all atoms in fcc-hollow sites) for which $\Theta = 1$. The formation energy can be calculated from both DFT and the LGH. In a diagram where $\Delta E_f$ obtained from DFT is plotted versus $\Theta$ for all configurations, the convex hull which connects the lowest lying points is called the DFT ground-state line. If the LGH predicts some configuration to lie below the DFT ground-state line, it is calculated with DFT and added to the input set for (4.5).

We calculated DFT energies of system configurations of $(2 \times 2)$, $(3 \times 3)$, $(4 \times 4)$, $(6 \times 6)$, and $(8 \times 8)$ periodicities. For the corresponding primitive cells, integration in the Brillouin zone could be performed consistently using a $(24 \times 24)$ k-point mesh in the $(1 \times 1)$ surface cell. These calculations were carried out with a slab of six layers of rhodium, where the three uppermost layers were allowed to relax.

Given some set of EIPs obtained from (4.5), we performed the search for new relevant structures by employing Metropolis Monte Carlo sampling at different temperatures from 100 K to 300 K in $(8 \times 8)$ and $(12 \times 12)$ surface cells. The coverage range was investigated in steps of approximately 0.01 ML and for each coverage $4 \times 10^4$ passes per lattice site were performed (one pass is defined as one trial move per particle). If in these Monte Carlo simulations a configuration was found to be lying below the DFT ground-state line in the formation energy plot, then this configuration was calculated with DFT and added to the set of input configurations for the cross validation procedure, which was subsequently started from scratch.

With an input of the DFT energies of 87 system configurations, which are shown in Appendix B.1, we obtained a LGH consisting of 18 pair, 17 trio, and 3 quattro interactions, a CV of 6.7 meV and a mean absolute error for the input configurations of 2.1 meV. An unsatisfactory point of this parametrization was that the error for the experimentally observed $(2\sqrt{3} \times 2\sqrt{3})R30^\circ$

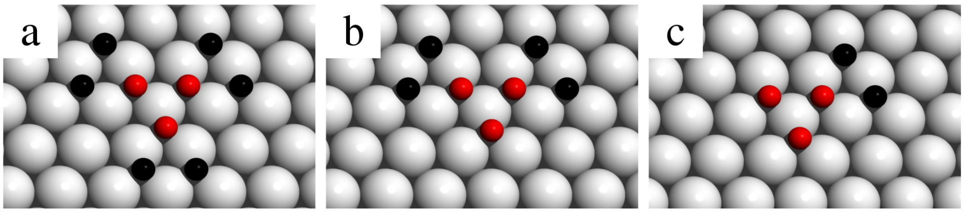

Figure 4.7: Three figures comprising oxygen atoms (red balls) as well as holes (black balls). An adsorption site is occupied by a hole if it is not occupied by an oxygen atom.

structure (Fig. 4.3 (c)) was as high as 11.1 meV, indicating that the relaxation effects in this structure are quite different from relaxation effects in all the other input structures. This problem is not only restricted to the description of the $(2\sqrt{3} \times 2\sqrt{3})R30°$ structure, but it also worsens the description of all the other input configurations, since every structure influences the EIPs of the figures it contains.

### 4.6.3 Inclusion of Unoccupied Sites

In principle, better parametrizations can be achieved by adding more and more figures to the pool from which the LGH is constructed. However, the problem with the bad description of the $(2\sqrt{3} \times 2\sqrt{3})R30°$ structure gave us the idea to address certain relaxation effects more directly by considering the occupation of sites that are adjacent to the particles of some figure. We added figures to our pool which include unoccupied sites and which are therefore particularly suited to describe certain relaxation effects. Since we defined a figure as and arrangement of *particles* in high symmetry adsorption sites, the extension to empty sites can be accomplished by formally including a second species of atoms which we will simply call *holes* in the remainder of this chapter and which occupy hollow sites if they are not occupied by oxygen atoms.

Fig. 4.7 shows three examples of figures comprising oxygen atoms as well as holes, where the latter are visualized as black balls. Considering these three figures (together with the figure in Fig. 4.6 (b)) means distinguishing explicitly different relaxation effects for the three nearest neighboring oxygens. If one of the three oxygen atoms has a pair of holes as nearest neighbors, as shown in Fig. 4.7, then this atom can easily relax towards the adjacent outward bridge site due to repulsive interaction with the other two oxygen atoms, whereas additional oxygen atoms instead of the holes would hinder outward relaxation. Consequently, quite large relaxation effects may be found if the figure in Fig. 4.7 (a) applies for a local arrangement of three nearest neighboring oxygen atoms, whereas only little relaxation effects will be observed if all of the neighboring holes are occupied.

However, in the lattice gas Hamiltonian the EIPs associated with figures including holes are accounted for in a slightly different way than the EIPs for which unoccupied sites are not directly considered. As an example, we show how the figures in Fig. 4.7 contribute to the expansion (4.4).

Let $T_1$ be the EIP that is associated with the figure in Fig. 4.6 (b). Consider three oxygen atoms which are arranged according to this figure, i.e. for which $t_{1,ijk} = 1$ in the expansion (4.4). Further, consider the three pairs of nearest neighboring fcc-hollow sites which are shown in Fig. 4.7 (a) to be unoccupied by oxygen (black balls). We call any of these three pairs of sites occupied if one or both sites are occupied by oxygen atoms, otherwise this pair of sites is unoccupied. The EIP $T_1$ next to $t_{1,ijk}$ in (4.4) is replaced according to

$$T_1 \rightarrow \begin{cases} T_1''' & \text{if} \quad \text{three pairs unoccupied,} \\ T_1'' & \text{if} \quad \text{one pair occupied and two pairs unoccupied,} \\ T_1' & \text{if} \quad \text{two pairs occupied and one pair unoccupied,} \\ T_1 & \text{if} \quad \text{three pairs occupied.} \end{cases} \tag{4.7}$$

Obviously, $T_1'''$, $T_1''$ and $T_1'$ correspond to the figures shown in Fig. 4.7 (a), (b) and (c), respectively. Note that the sums in (4.4) still only run over the adsorbed oxygen atoms in the system and not over holes. If the figures that comprise holes were accounted for in the usual way, then, for example, also the figure in Fig. 4.7 (b) would apply for a local arrangement of atoms if (a) applies. However, according to (4.7), only one of these two figures can apply at most. This approach allows for a more efficient mapping of different relaxation effects to different figures.

We constructed figures including holes with two as well as with three oxygen atoms and added the resulting new figures to our pool from which the EIPs were selected. Yet only EIPs associated with figures consisting of three oxygen atoms plus holes were selected by our algorithm. With this new parametrization, the cross validation score and the mean absolute error for the input configurations improved to 5.9 meV and 1.8 meV, respectively. The LGH now consisted of 18 pair and 21 trio interactions, of which 5 trio interactions were associated with figures comprising holes, and one quattro interaction. The error for the $(2\sqrt{3} \times 2\sqrt{3})R30°$ structure decreased from 11.1 meV to 5.5 meV.

A further improvement of the parametrization was accomplished by adding a figure to our pool consisting of six oxygen atoms in fcc-hollow sites and six holes (Fig. 4.8 (b)). By including the holes, this figure leads to a good description of the $(2\sqrt{3} \times 2\sqrt{3})R30°$ structure, because it accounts for important relaxation effects that are typical for this configuration (indicated as black arrows in Fig. 4.8 (a)). If we would only use the six oxygen atoms without the holes as a figure, other structures, which comprise the triangle of six oxygen atoms without major lateral relaxations (e.g. the $p(1 \times 1)$ phase), would influence the value of the corresponding EIP so that it would not lead

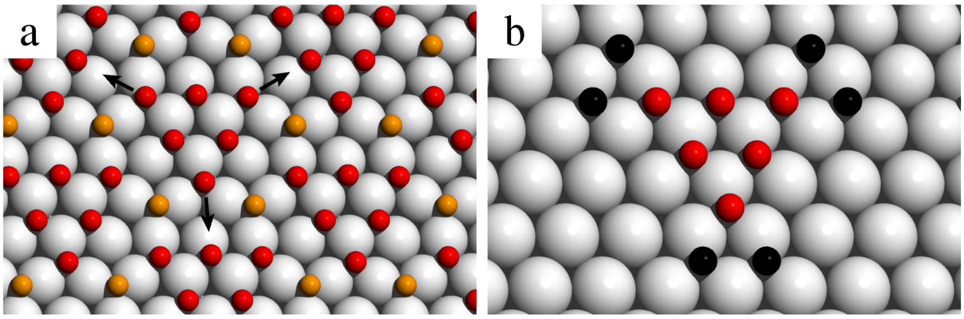

Figure 4.8: The holes of the figure in (b) allow for the typical outward relaxation of the oxygen atoms at the corners toward the bridge sites as it occurs in the $(2\sqrt{3} \times 2\sqrt{3})R30°$ structure, indicated by the black arrows in (a). Note that the positions of the black balls in (b) are not occupied by oxygen atoms in the configuration in (a).

to a significant improvement of the description of the $(2\sqrt{3} \times 2\sqrt{3})R30°$ structure.

Our final parametrization had values of 5.6 meV, 1.7 meV, and 1.0 meV for the cross validation score, the mean absolute error for the input configurations, and the error of the $(2\sqrt{3} \times 2\sqrt{3})R30°$ structure, respectively. The LGH consisted of 15 pair, 22 trio (5 of which associated with figures comprising holes), 3 quattro interactions and the effective EIP corresponding to the figure of six oxygen atoms and six holes (Fig. 4.8 (b)). The values of the EIPs and the associated figures are given in Appendix B.2. The adsorption energies of the isolated oxygen atom obtained from cross validation were −2.121 eV for the fcc-hollow site and −2.020 eV for the hcp-hollow site, which are almost identical with the values in Table 4.1.

The formation energy plot for this parametrization is shown in Fig. 4.9. In the coverage range between 0.35 and 0.50 ML we obtained structures from the lattice gas Hamiltonian slightly lower in energy than the DFT groundstate line. This may be related to the fact that some of the structures that were found in this range in the course of the Monte Carlo simulations could not be investigated with DFT, because they were not compatible with one of our periodic cells ($(2 \times 2)$, $(3 \times 3)$, $(4 \times 4)$, $(6 \times 6)$, and $(8 \times 8)$), for which integration of the Brillouin zone could be performed consistently and which were feasible in terms of computing time. For example, the configuration shown in Fig. 4.10 (a) at a coverage of 0.42 ML has a $(12 \times 12)$ periodicity with respect to the primitive cell vectors that are indicated in the picture. Calculations in such a big cell were beyond our computational capabilities. Note that this structure can also be calculated with a smaller cell but with different orientations of the primitive cell vectors, which does not allow for integration of the Brillouin zone in accordance with the other surface cells used in this work.

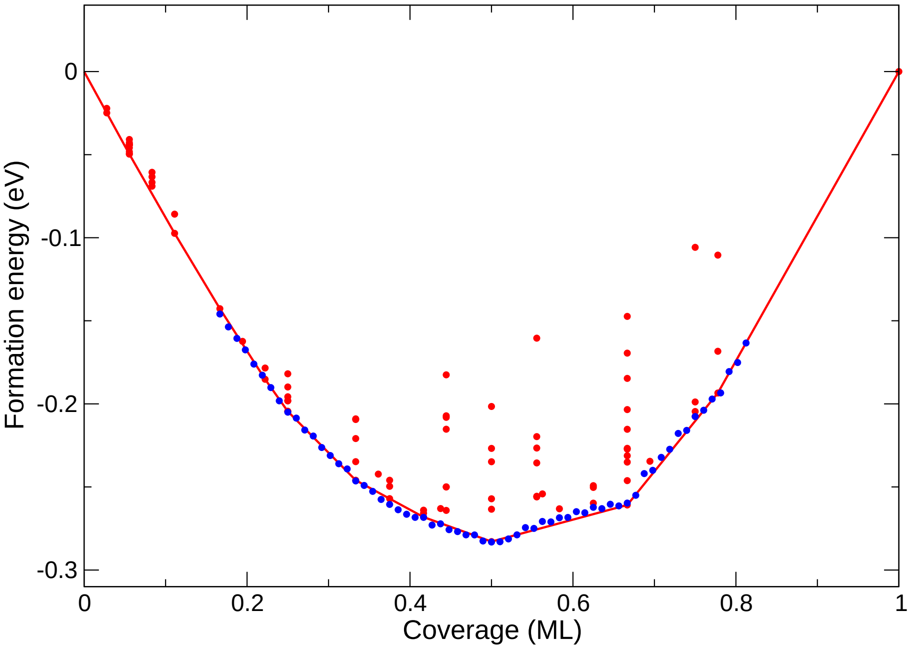

Figure 4.9: Formation energy plot. Red points show formation energies per oxygen atom given by DFT calculations. Blue points show the lowest formation energies given by the lattice gas Hamiltonian. The DFT ground-state line in red is the convex hull of the DFT formation energies.

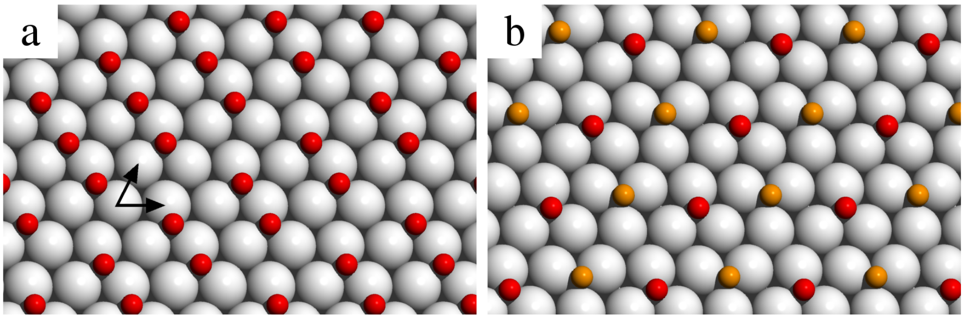

Figure 4.10: (a) Structure (unrelaxed) at a coverage of 0.42 ML with a $(12 \times 12)$ periodicity with respect to the primitive cell vectors that are indicated. (b) New stable structure at a coverage of $1/3$ ML.

| | Interactions | Species | CV | $\Delta E_{\text{in}}$ | $\Delta E_{2\sqrt{3}}$ |
|---|---|---|---|---|---|
| a | many-body | O, holes | 5.6 | 1.7 | 1.0 |
| b | many-body | O, holes | 5.9 | 1.8 | 5.5 |
| c | many-body | O | 6.7 | 2.1 | 11.1 |
| d | pairs only | O | 16.1 | 8.2 | 38.6 |

Table 4.2: Summary of the different parametrizations. CV is the cross validation score, $\Delta E_{\text{in}}$ is the mean absolute error for the input configurations, and $\Delta E_{2\sqrt{3}}$ is the error for the $(2\sqrt{3} \times 2\sqrt{3})R30°$ structure. All values are in meV per oxygen atom. (a) Parametrization using figures comprising oxygen atoms as well as holes. (b) Same as parametrization (a), but without the figure in Fig. 4.8 (b). (c) Parametrization for which figures comprising holes are not used. (d) Parametrization with pair interactions only.

Interestingly, our parametrization predicts a new ground state structure at a coverage of 1/3 ML (Fig. 4.10 (b)), which is also stable within the DFT calculations. Yet the energy difference between this new phase and a mixture of a $p(2 \times 2)$ phase and a $p(2 \times 1)$ phase is rather small, which might hinder an experimental verification at elevated temperatures.

### 4.6.4 Parametrization with Pair Interactions only

Constructing a lattice gas Hamiltonian of only pair interactions, the best parametrization we could find consisted of 16 pair interactions and had values of 16.1 meV for the cross validation score, 8.2 meV for the mean absolute error for the input configurations, and 38.6 meV for the error of the $(2\sqrt{3} \times 2\sqrt{3})R30°$ structure. Not only is the latter error very large, but at a coverage of 2/3 ML the LGH also predicts five other structures to be more stable than the $(2\sqrt{3} \times 2\sqrt{3})R30°$ structure, which however is the most stable phase according to DFT at this coverage. The LGH of only pairwise interactions generally is better suited to describe configurations at lower than at higher coverages. Whereas the mean absolute error for the input configurations is 12.2 meV at coverages larger than or equal to 1/2 ML, it is only 5.1 meV at coverages less than 1/2 ML. Consequently, especially configurations at high coverages require a description with many-body interactions. In Table 4.2, all foregoing parametrizations are summarized.

## 4.7 TPD Spectra

In the following section, we shall discuss the influence of the different parametrizations on the simulation of the desorption spectra.

We have simulated the TPD spectra performing kMC runs on a $(60 \times 60)$ lattice grid (comprising $60 \times 60$ fcc-hollow sites plus $60 \times 60$ hcp-hollow sites).

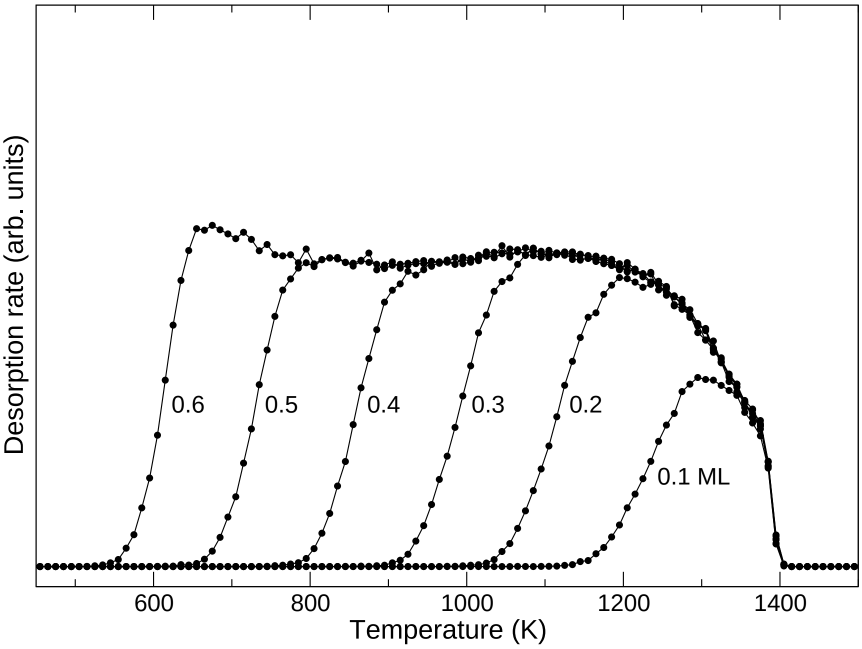

Figure 4.11: Simulated TPD spectra for O/Rh(111) for a coverage of 0.1 - 0.6 ML. These spectra were obtained by employing the parametrization with the lowest cross validation score (parametrization (a) of Table 4.2).

Performing test calculations on an $(80 \times 80)$ lattice grid with the same number of simulation runs, we found that the statistical noise of the data is a bit larger for the $(60 \times 60)$ grid. With an adequate number of additional runs on the $(60 \times 60)$ lattice grid, results from the $(60 \times 60)$ and the $(80 \times 80)$ grids were identical within the statistical error bars. Each desorption curve was taken as the average over 240 simulation runs. The initial configurations were set up randomly and equilibrated using Metropolis Monte Carlo performing 100 passes per lattice site for coverages greater than 0.5 ML, and 200 passes per lattice site for coverages less than or equal to 0.5 ML. After every desorption event, the system was equilibrated with the Metropolis algorithm performing a total of 400 passes. Taking twice the number of passes for initial configurations and after desorption events, the spectra remained unchanged within the statistical error bars.

Fig. 4.11 shows the simulated desorption spectra for a coverage ranging from 0.1 to 0.6 ML, calculated with the set of EIPs of lowest cross validation score (parametrization (a) of Table 4.2). The prefactor $\nu$ for the rate constants of desorption (4.3) was adjusted to experimental spectra, which are shown in Fig. 4.12. With a constant prefactor of $2 \times 10^{15}\,\mathrm{s}^{-1}$, the low-coverage

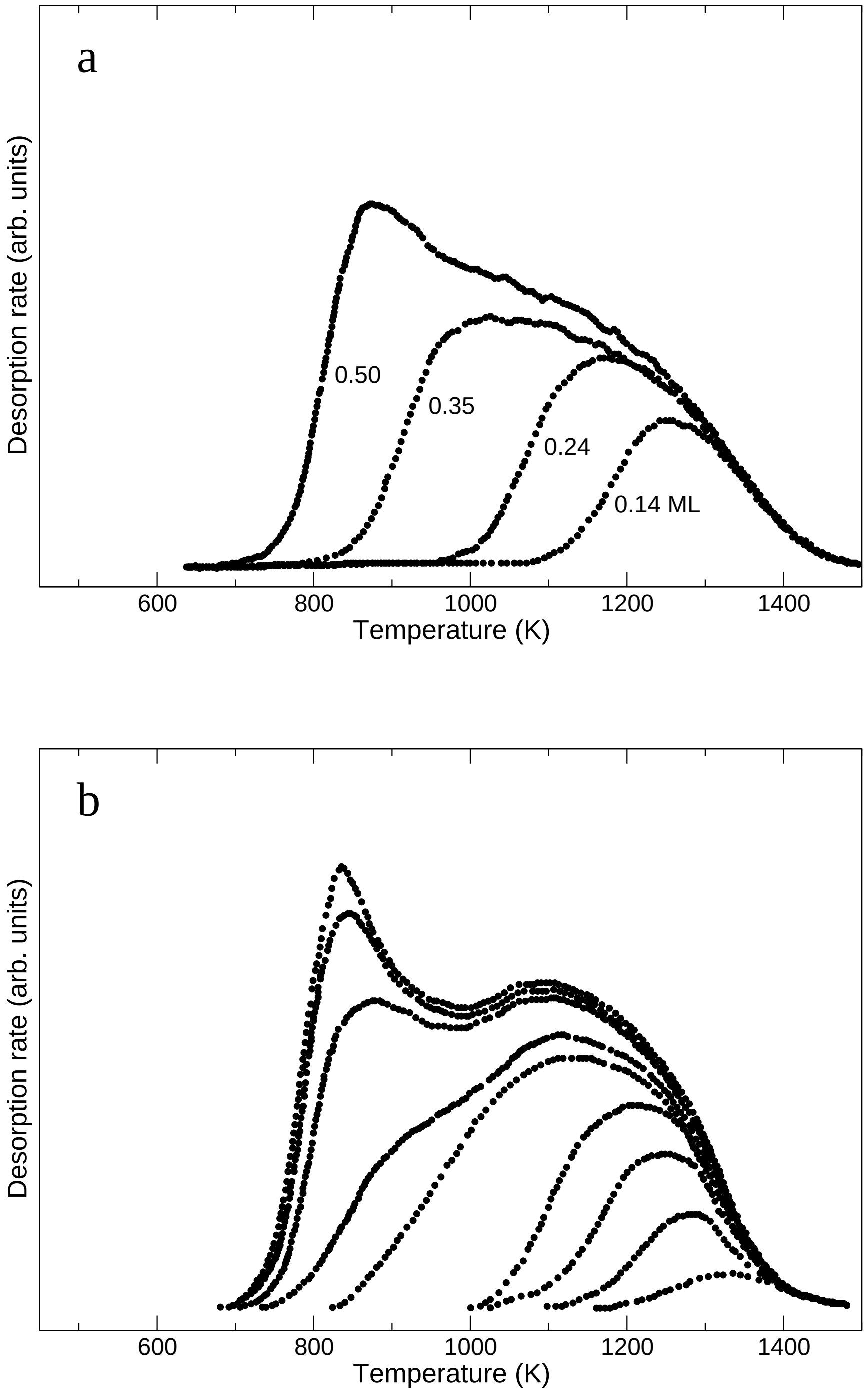

Figure 4.12: Experimental TPD spectra for O/Rh(111): (a) Spectra for a coverage of 0.14 - 0.50 ML from Xu and Friend [59]; (b) Spectra as a function of increasing exposure from 0.2 to 13 langmuirs from Root, Schmidt, and Fisher [60].

(high temperature) end of the spectra was shifted to approximately 1400 K to obtain agreement with the experimental data.

While the simulated spectra can be directly compared with the experimental data of Xu and Friend [59] (Fig. 4.12 (a)), who have measured the desorption spectra as a function of the oxygen coverage, the comparison with the second experimental spectrum measured by Root et al. (Fig. 4.12 (b)) is less clear as they have only indicated a dosing of 0.2 - 13 langmuirs of oxygen prior to the desorption [60]. While the authors claim that this dose corresponds to an effective coverage of 0.83 ML, other data in literature point towards a saturation coverage of about 0.5 ML under these preparation conditions [61, 62, 63].

Since the adsorption energies based on DFT calculations using gradient corrected PBE potentials have errors in the order of 0.1 eV and because a constant prefactor has been used, the onset of the desorption curve can not be described accurately on this level of theory. Both uncertainties, however, hardly affect the general shape of the curve. It has been shown previously that errors introduced by the choice of the exchange correlation functional primarily lead to a constant shift of the adsorption energies but have only little effect on the lateral interaction energies [57]. A stronger binding energy of 0.1 eV shifts the simulated TPD curves to lower temperatures (50 - 100 K) and the width of the curves decreases, weaker binding has the opposite effect, but the general shape of the curves remains unchanged. Increasing or decreasing a constant prefactor by an order of magnitude has similar effects as shifting the adsorption energies, but again has little influence on the shape of the TPD curves. Fig. 4.13 shows how the simulated spectra change if a prefactor of $2 \times 10^{14}\,\mathrm{s}^{-1}$ instead of $2 \times 10^{15}\,\mathrm{s}^{-1}$ is used. Yet it should be noted that the exact prefactor is not constant, but a function depending on temperature and coverage. If the constant prefactor could be replaced by the exact function in the simulations, this would very likely affect the general shape of the curve. In Chapter 5, we shall present our first attempts to calculate the temperature dependency of the prefactor via thermodynamic integration.

The general shape of the experimental spectra is reasonably well reproduced in our simulations. While the spectra display only a single peak in the case of a low oxygen coverage, the spectra display a broad plateau at a higher starting coverage and finally display a second peak at a lower temperature for a starting coverage of 0.5 ML. A comparison between the simulated and the experimental spectra also shows that the simulations seem to underestimate the relative desorption rate at lower temperatures. This observation can be presumably attributed to the fact that a constant prefactor was used in the simulations.

Fig. 4.14 shows the change of the TPD spectra if parametrizations (b) and (c) of Table 4.2 are used. Using the parametrization for which the figure consisting of six oxygen atoms and six holes (Fig. 4.8 (b)) is excluded

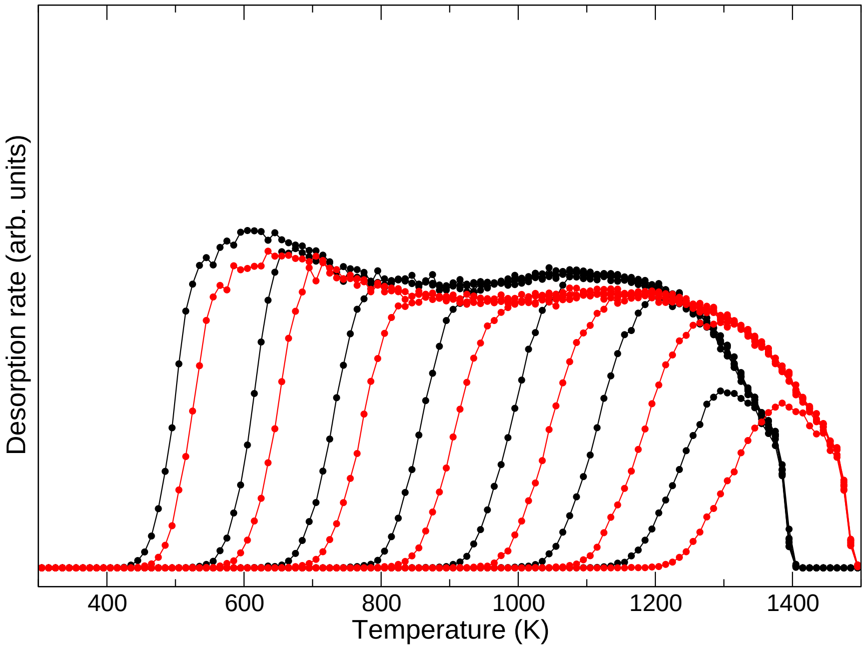

Figure 4.13: Simulated TPD spectra for a coverage of 0.1 - 0.7 ML: prefactor of $2 \times 10^{14}\,\mathrm{s}^{-1}$ (red) instead of $2 \times 10^{15}\,\mathrm{s}^{-1}$ (black).

(parametrization (b)), virtually no change is observed for starting coverages of 0.4 ML and lower. For higher coverages, small deviations from the spectra obtained with the parametrization of lowest CV are found. The deviations become larger as the parametrization is used for which figures that comprise holes are not included (parametrization (c)). Particularly for high coverages larger than 0.6 ML a major change in the spectra is observed (Fig. 4.14 (b)).

The red curves in Fig. 4.15 (a) depict the simulated TPD spectra obtained with only pair interactions (parametrization (d) of Table 4.2). This model gives an appropriate description in the limit of a low starting coverage, and displays only small deviations up to a starting coverage of 0.4 ML. For higher coverages of above 0.4 ML, the deviations are more pronounced. This observation reflects the fact that the parametrization using only pair interactions yields a more pronounced error for high-coverage structures, as shown in the previous section.

Fig. 4.15 (b) shows a comparison between the multi-site lattice gas model and a single-site model. Although only one single site, the fcc-hollow, is occupied in the experimental ground state structures at a low coverage, a single-site model fails to capture several interactions which are essential at

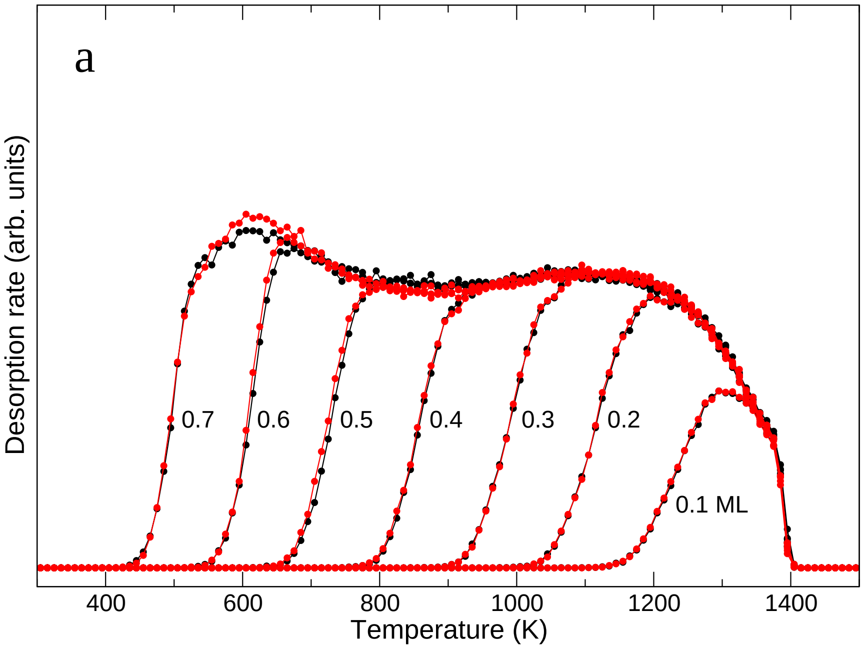

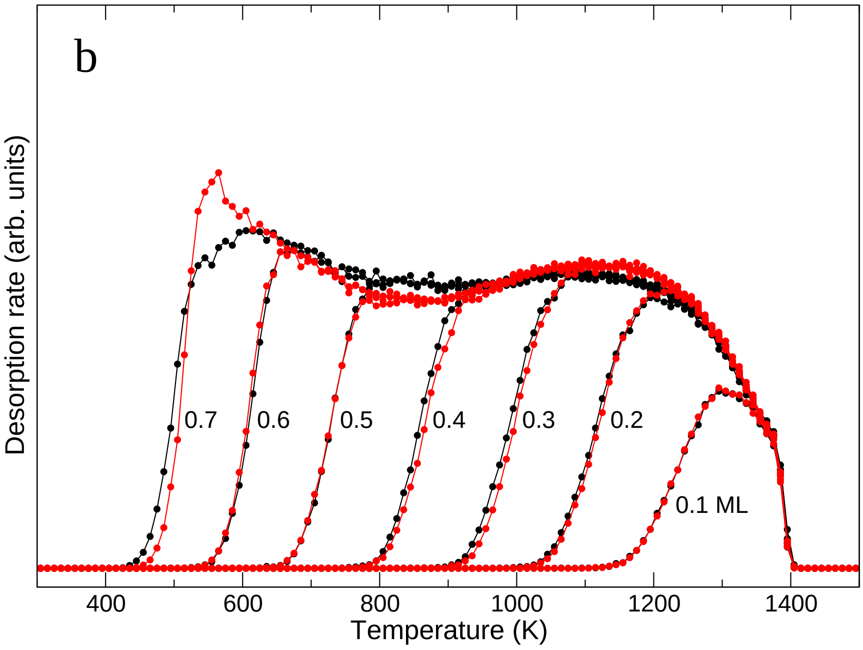

Figure 4.14: The black curves show the TPD spectra simulated with the parametrization of lowest CV. The red curves show: (a) TPD spectra simulated with the parametrization for which the figure in Fig. 4.8 (b) is excluded (parametrization (b) of Table 4.2); (b) TPD spectra simulated with the parametrization for which figures that comprise holes are not included (parametrization (c) of Table 4.2).

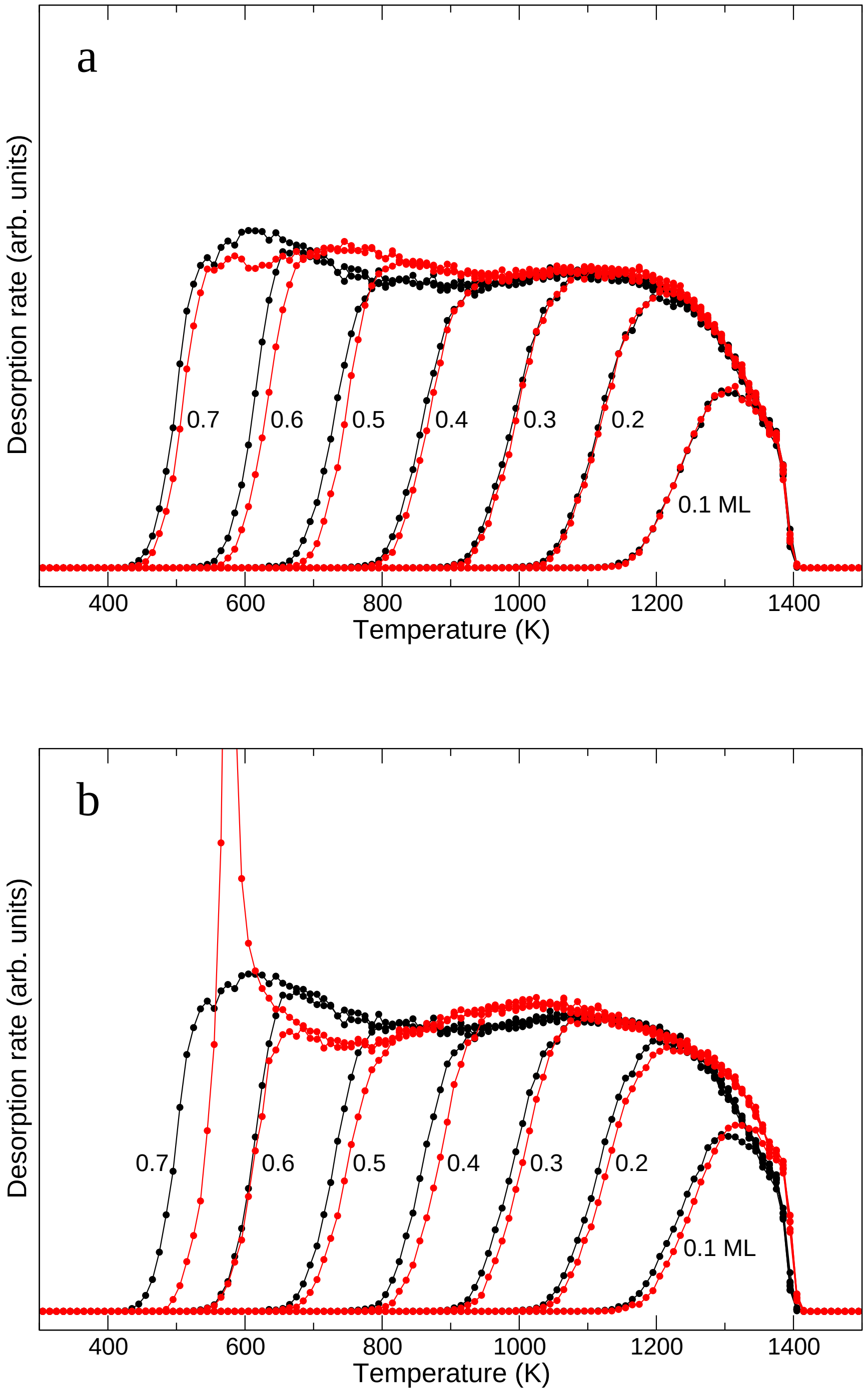

Figure 4.15: (a) TPD spectra simulated with the parametrization with pair interactions only (parametrization (d) of Table 4.2). (b) TPD spectra from a single-site model (only fcc-hollow sites).

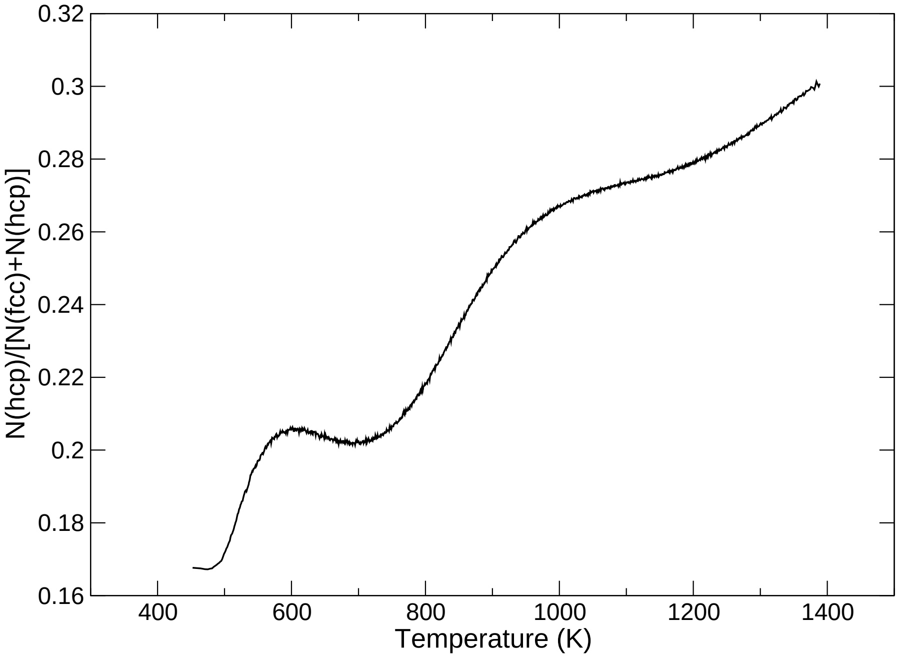

Figure 4.16: Fraction of atoms occupying hcp-hollow sites as a function of temperature.

the elevated temperatures used in the desorption experiments. Deviations between the TPD spectra from the single-site and the multi-site model can already be observed at lower coverages present in the higher temperature range. For an intermediate starting coverage of 0.3 ML and higher, the maximum of the curve is shifted to lower temperatures, and the second peak is not discernible at a starting coverage of 0.5 ML, but only appears using a higher starting coverage of 0.6 ML of oxygen. This observation can be related to the small energy differences between adsorption in hcp- and fcc-hollow sites, resulting in an occupation of hcp sites at elevated temperatures. Fig. 4.16 shows that the fraction of oxygen atoms in hcp-hollow sites is 0.2 to 0.3, as sampled in the course of the Monte Carlo simulations. Finally, for a starting coverage of 0.7 ML, the high oxygen content results in a drastic overestimation of the adsorbate-adsorbate repulsion, which in turn leads to a strong overestimation of the first desorption peak at 600 Kelvin.

## 4.8 Summary

We have investigated several models for the parametrization of the interaction of oxygen atoms adsorbed on a Rh(111) surface within a lattice gas

Hamiltonian, and used this parametrization to simulate temperature programed desorption spectra with a kinetic Monte Carlo algorithm. We find that an optimized parametrization only based on pair interactions yields a cross validation score of about 16 meV per oxygen atom, with especially pronounced deviations between LGH and DFT energies for high-coverage adsorption phases. The average error in the description is significantly reduced by including many-body interactions. If a selection of three- and four-body interactions is included in the LGH, the cross validation score can be reduced to less than 7 meV. Yet we still find a large error of 11.1 meV for the experimentally observed high-coverage $(2\sqrt{3} \times 2\sqrt{3})R30^\circ$ structure, which can be related to particular relaxation effects. An inclusion of unoccupied sites in the construction of the LGH allows to efficiently reduce the error in the parametrization of this structure to a value of only 1 meV.

Using various parametrizations as input for the kMC simulations of the TPD spectra, we find that the description of the low-coverage desorption spectra is rather robust with respect to the models used. Even a model based exclusively on a single adsorption site gives a reasonable description for a starting coverage smaller than 0.3 ML of oxygen, but deviations from the spectra obtained from a full parametrization become evident for a higher starting coverage. The reason for this behavior can be found in the substantial amount of (metastable) hcp-hollow sites that are occupied at the elevated temperatures needed for the desorption of the oxygen atoms. Consequently, the predictive power is significantly enhanced using a multi-site model including both fcc- and hcp-hollow sites. We note that using a multi-site model, the different parametrizations presented in this work provide similar shapes for the spectra, even if the LGH is restricted to pairwise interactions.

We therefore conclude that an accurate parametrization of the adsorbate interactions is mandatory for the correct prediction of the adsorption phases, but a significantly lower level of accuracy is needed for the prediction of the thermal desorption spectra. Only for the simulation of the desorption spectra starting from a high oxygen coverage greater than 0.6 ML, improved multi-site models have to be taken into account.

Deviations between simulated and experimental TPD spectra are presumably due to the fact that a constant prefactor was used in the simulations in order to calculate the desorption rate constants. The next chapter is dedicated to the evaluation of the temperature dependency of the prefactor.

# Chapter 5

# Free Energy Calculations for O/Rh(111)

## 5.1 Introduction

Our motivation for starting free energy calculations was to determine the temperature dependence of the prefactor used in the kinetic Monte Carlo simulations (Chapter 4) in order to obtain better agreement between simulated and experimental TPD spectra. Our guideline was the work of Alfè and Gillan who have used constrained Molecular Dynamics simulations for computing free energy curves for the desorption of water from MgO(001), from which they deduced absolute desorption rates and the prefactor [64, 65]. However, whereas water on MgO(001) only undergoes physisorption, in the case of oxygen adsorption on Rh(111) we are concerned with strong chemisorption and dissociation of the $O_2$ molecule. While the free energy calculations for this system were planned to be only a part of the kinetic Monte Carlo project, they turned out to be quite a challenge and became a full research project of their own in the framework of this thesis.

This chapter consists basically of three parts. In the first part, the method of *thermodynamic integration of free energy gradients* is explained in detail. The second part is about free energy calculations for a simple test case, namely the diffusion of an oxygen atom from an hcp-hollow site to an fcc-hollow site. In the third part of the chapter, we report on free energy calculations for the desorption of $O_2$ from the rhodium surface, which turned out to be considerably more involved than the calculations for the diffusion event.

We have carried out the calculations for temperatures of 10 K, 350 K, 700 K, and 1400 K. The calculations for 10 K allowed to gauge the reliability of the methods. The free energy calculations were performed for temperatures up to 1400 K since the experimental TPD spectra for oxygen desorbing from Rh(111) display desorption occurring up to approximately this temperature (see Fig. 4.12). For both diffusion and desorption we have compared the free energy differences resulting from thermodynamic integration with those resulting from a harmonic approximation.

## 5.2 Thermodynamic Integration

The free energy can not be computed as a mean value in a simulation as it can be done with the potential energy or the kinetic energy. At constant volume $V$ and temperature $T$, the ensemble average of an observable $O$ for a system of $N$ atoms with $3N$ Cartesian coordinates $\mathbf{x}$ and $3N$ momenta $\mathbf{p}$ is of the form

$$\langle O \rangle = \frac{\int \mathrm{d}\mathbf{x}\,\mathrm{d}\mathbf{p}\, O(\mathbf{x},\mathbf{p})\, \exp[-\beta\,\mathcal{H}(\mathbf{x},\mathbf{p})]}{\int \mathrm{d}\mathbf{x}\,\mathrm{d}\mathbf{p}\, \exp[-\beta\,\mathcal{H}(\mathbf{x},\mathbf{p})]}, \tag{5.1}$$

where $\mathcal{H}$ is the Hamiltonian of the system. This ensemble average can be calculated using Monte Carlo simulations. Assuming that the *ergodic hypothesis* holds for the system to be examined (time average equals ensemble average), (5.1) can also be computed by applying Molecular Dynamics. However, the Helmholtz free energy

$$F = -k_B T \ln Q_{NVT}, \tag{5.2}$$

with the canonical partition function

$$Q_{NVT} \propto \int \mathrm{d}\mathbf{x}\,\mathrm{d}\mathbf{p}\, \exp[-\beta\,\mathcal{H}(\mathbf{x},\mathbf{p})], \tag{5.3}$$

can not be expressed in the form (5.1). Hence the free energy can not be calculated as a mean value in a Monte Carlo or Molecular Dynamics simulation [66].

Thermodynamic integration of free energy gradients relies on the fact that, if not the free energy itself, at least derivatives of the free energy can be computed as ensemble averages, which allows for the calculation of free energy *differences*. In particular, the derivative of the free energy with respect to a reaction coordinate $\xi$ is [67]

$$\left(\frac{\mathrm{d}F}{\mathrm{d}\xi}\right)_{\xi'} = \left\langle \frac{\partial \mathcal{H}}{\partial \xi} \right\rangle_{\xi'}, \tag{5.4}$$

where the subscript $\xi'$ indicates that the ensemble average is taken at fixed value of the reaction coordinate $\xi = \xi'$. Integration of this function from $\xi_0$ to $\xi_1$ yields the free energy difference

$$\Delta F_{\xi_0 \to \xi_1} = \int_{\xi_0}^{\xi_1} \left(\frac{\mathrm{d}F}{\mathrm{d}\xi}\right)_{\xi'} \mathrm{d}\xi'. \tag{5.5}$$

If the reaction coordinate $\xi = \xi(\mathbf{x})$ can not be defined analytically, the integral (5.5) has to be approximated by integration over one or several simple geometric parameters $\{\zeta_k\}$, $k = 1, 2, \ldots, n$. Ideally, this set of parameters is complete in the sense that constraining all of these parameters necessarily constrains the reaction coordinate,

$$(\forall k : \dot{\zeta}_k = 0) \Rightarrow (\dot{\xi} = 0), \tag{5.6}$$

otherwise the derivatives (5.4) can not be calculated. Furthermore, $\xi$ as a function of the set $\{\zeta_k\}$ should be continuous, so that following any path in the coordinate system spanned by $\{\zeta_k\}$ does not result in any jumps of $\xi$. In practice, both conditions ((5.6) and continuity) will in general not be perfectly fulfilled. In this sense, the reaction coordinate $\xi$ is *approximated* by the parameters $\{\zeta_k\}$.

For the thermodynamic integration (5.5), two sets of values $\{\zeta_{k,0}\}$ and $\{\zeta_{k,1}\}$ need to be found such that

$$\begin{aligned} \xi(\zeta_{1,0}, \zeta_{2,0}, \ldots, \zeta_{n,0}) &= \xi_0, \\ \xi(\zeta_{1,1}, \zeta_{2,1}, \ldots, \zeta_{n,1}) &= \xi_1. \end{aligned} \tag{5.7}$$

By substituting the total derivative

$$\mathrm{d}F = \sum_{k=1}^{n} \frac{\partial F}{\partial \zeta_k}\, \mathrm{d}\zeta_k \tag{5.8}$$

into (5.5) and using (5.7) we obtain the line integral

$$\Delta F_{\xi_0 \to \xi_1} = \sum_{k=1}^{n} \int_{\zeta_{k,0},\, L}^{\zeta_{k,1}} \left( \frac{\partial F}{\partial \zeta_k} \right)_{\zeta'} \mathrm{d}\zeta'_k, \tag{5.9}$$

where the '$L$' indicates that the derivatives $\{\partial F/\partial \zeta_k\}$ are evaluated along a line in the space spanned by $\{\zeta_k\}$. The derivatives are computed for fixed values $\zeta' = (\zeta'_1, \zeta'_2, \ldots, \zeta'_n)$, i.e. $\zeta_k = \zeta'_k$ for all $k$.

In order to calculate the quantities $\{\partial F/\partial \zeta_k\}$ in (5.9), we have used the *blue-moon ensemble* method [68]. In case of multiple geometric parameters $\{\zeta_k\}$ to be constrained in a system of $N$ atoms with masses $\{m_i\}$, the derivative of the free energy with respect to the parameter $\zeta_k$ reads [69, 70, 71]

$$\begin{aligned} \left( \frac{\partial F}{\partial \zeta_k} \right)_{\zeta'} &= \frac{1}{\langle |\mathbf{Z}|^{-1/2} \rangle_{\zeta'}} \Bigg\langle |\mathbf{Z}|^{-1/2} \Bigg( \lambda_{\zeta_k} + \frac{k_B T}{2\, |\mathbf{Z}|} \\ &\quad \times \sum_{j=1}^{n} (\mathbf{Z}^{-1})_{kj} \sum_{i=1}^{N} m_i^{-1}\, \nabla_i \zeta_j \cdot \nabla_i\, |\mathbf{Z}| \Bigg) \Bigg\rangle_{\zeta'}. \end{aligned} \tag{5.10}$$

The quantity $\lambda_{\zeta_k}$ is the Lagrange multiplier associated with the geometric parameter $\zeta_k$ and is calculated by VASP using the SHAKE algorithm [72]. The tensor $\mathbf{Z}$ is defined as

$$(\mathbf{Z})_{\alpha\beta} = \sum_{i=1}^{3N} m_i^{-1} \frac{\partial \zeta_\alpha}{\partial x_i} \frac{\partial \zeta_\beta}{\partial x_i}, \tag{5.11}$$

where $\{x_i\}$ are the Cartesian coordinates of the particles.

The derivation of (5.10) can be roughly sketched as follows. First, a full set of generalized coordinates, including the set $\{\zeta_k\}$ of coordinates to be constrained, is introduced. The partition function $Q(\{\zeta_k\})$ and its derivatives $\partial Q/\partial \zeta_k$ are then expressed as integrals over the generalized coordinates. The Lagrange multipliers are introduced by setting up the equations of motion for the coordinates $\{\zeta_k\}$, which are Euler-Lagrange equations. Taking $\dot{\zeta}_k = 0$ and $\ddot{\zeta}_k = 0$ into account yields an equation for the Lagrange multiplier $\lambda_{\zeta_k}$ containing terms which can also be found in the aforementioned formula for $\partial Q/\partial \zeta_k$. Hence a substitution yields an equation for $\partial Q/\partial \zeta_k$ containing $\lambda_{\zeta_k}$. With some modifications, this derivative is substituted in

$$\frac{\partial F}{\partial \zeta_k} = -\frac{k_B T}{Q} \frac{\partial Q}{\partial \zeta_k}, \tag{5.12}$$

which leads to (5.10). Note that (5.12) follows immediately from $F(\{\zeta_k\}) = -k_B T \ln Q(\{\zeta_k\})$.

VASP calculates the derivatives of the free energy according to (5.10), independent of the constraints imposed to the system. However, in our simulations the numbers given by the code showed that in case of the constraints used in this work, the determinant $|\mathbf{Z}|$ is a constant. It is easy to see from (5.10) that in this special case, which implies $\nabla_i |\mathbf{Z}| = 0$ for all $i$, the derivative of the free energy is simply given by the statistical average of the Lagrange multiplier:

$$\left(\frac{\partial F}{\partial \zeta_k}\right)_{\zeta'} = \langle \lambda_{\zeta_k} \rangle_{\zeta'}\,. \tag{5.13}$$

It is well known that certain types of constraints lead to a constant $|\mathbf{Z}|$ and hence to (5.13). In case of oxygen diffusion, the only constraint we impose to the system is a bond distance between two atoms. In case of oxygen desorption, one of two constraints is again a bond distance and the other one (which controls the height of the $O_2$ molecule) is a linear combination of the coordinates of certain atoms. For both types of constraints, $|\mathbf{Z}|$ is constant [71].

Although VASP uses the general formula (5.10) anyway, it is helpful to know about the validity of (5.13), since the analysis of statistical errors is easier to handle for equation (5.13) than for equation (5.10), which is a combination of two statistical averages.

The question arises of how the boundaries $\xi_0$ and $\xi_1$ for the integration (5.5) should be chosen. To answer that question, we consider the free energy difference for a reaction which leads the system from one stable domain in configuration space, labeled state 0, to another stable domain, labeled state 1. This free energy difference can be written as

$$\Delta F_{0\to 1} = -\,k_B T \ln \frac{Q_1}{Q_0}, \tag{5.14}$$

where $Q_0$ and $Q_1$ are the partition functions of state 0 and state 1. Since the integrals over the momenta cancel, this expression reduces to

$$\Delta F_{0\to 1} = -\,k_B T \ln \frac{Z_1}{Z_0}, \tag{5.15}$$

with configuration integrals $Z_0$ and $Z_1$ of the form

$$Z = \int \mathrm{d}\mathbf{x} \exp[-\beta\, U(\mathbf{x})], \tag{5.16}$$

where $U(\mathbf{x})$ is the potential energy function.

Let the value of the reaction coordinate $\xi$ be increasing as the system moves from state 0 to state 1. We introduce the real number $\xi^*$ and define the system to be in state 0 if $\xi \le \xi^*$ and to be in state 1 if $\xi \ge \xi^*$. The ratio of configuration integrals can be written as

$$\frac{Z_1}{Z_0} = \frac{\int \mathrm{d}\mathbf{x}\ \exp[-\beta\, U(\mathbf{x})]\, \theta(\xi - \xi^*)}{\int \mathrm{d}\mathbf{x}\ \exp[-\beta\, U(\mathbf{x})]\, (1 - \theta(\xi - \xi^*))}, \tag{5.17}$$

where $\theta$ is the Heaviside step function. This equation can trivially be expanded to

$$\begin{aligned}\frac{Z_1}{Z_0} \;=\;& \frac{\int \mathrm{d}\mathbf{x}\ \exp[-\beta\, U(\mathbf{x})]\, \delta(\xi - \xi_0)}{\int \mathrm{d}\mathbf{x}\ \exp[-\beta\, U(\mathbf{x})]\, (1 - \theta(\xi - \xi^*))} \\ &\times \frac{\int \mathrm{d}\mathbf{x}\ \exp[-\beta\, U(\mathbf{x})]\, \delta(\xi - \xi_1)}{\int \mathrm{d}\mathbf{x}\ \exp[-\beta\, U(\mathbf{x})]\, \delta(\xi - \xi_0)} \\ &\times \frac{\int \mathrm{d}\mathbf{x}\ \exp[-\beta\, U(\mathbf{x})]\, \theta(\xi - \xi^*)}{\int \mathrm{d}\mathbf{x}\ \exp[-\beta\, U(\mathbf{x})]\, \delta(\xi - \xi_1)},\end{aligned} \tag{5.18}$$

where $\delta$ is the Dirac delta function. If we choose $\xi_0$ and $\xi_1$ to be typical values of the reaction coordinate in state 0 and state 1, respectively, we obtain $(1 - \theta(\xi_0 - \xi^*)) = 1$ and $\theta(\xi_1 - \xi^*) = 1$. Hence, (5.18) can be written as

$$\begin{aligned}\frac{Z_1}{Z_0} &= \frac{\int \mathrm{d}\mathbf{x}\,\exp[-\beta\,U(\mathbf{x})]\,\delta(\xi-\xi_0)\,(1-\theta(\xi-\xi^*))}{\int \mathrm{d}\mathbf{x}\,\exp[-\beta\,U(\mathbf{x})]\,(1-\theta(\xi-\xi^*))} \\ &\times \frac{\int \mathrm{d}\mathbf{x}\,\exp[-\beta\,U(\mathbf{x})]\,\delta(\xi-\xi_1)}{\int \mathrm{d}\mathbf{x}\,\exp[-\beta\,U(\mathbf{x})]\,\delta(\xi-\xi_0)} \\ &\times \frac{\int \mathrm{d}\mathbf{x}\,\exp[-\beta\,U(\mathbf{x})]\,\theta(\xi-\xi^*)}{\int \mathrm{d}\mathbf{x}\,\exp[-\beta\,U(\mathbf{x})]\,\delta(\xi-\xi_1)\,\theta(\xi-\xi^*)}. \end{aligned} \tag{5.19}$$

The first term on the right hand side of equation (5.19) is the conditional probability density of $\xi_0$ given the system to be in state 0,

$$\frac{\int \mathrm{d}\mathbf{x}\,\exp[-\beta\,U(\mathbf{x})]\,\delta(\xi-\xi_0)\,(1-\theta(\xi-\xi^*))}{\int \mathrm{d}\mathbf{x}\,\exp[-\beta\,U(\mathbf{x})]\,(1-\theta(\xi-\xi^*))} = \langle\delta(\xi-\xi_0)\rangle_{\xi\le\xi^*}\,, \tag{5.20}$$

where $\langle\,\rangle_{\xi\le\xi^*}$ denotes a conditional ensemble average. Similarly, the last term on the right hand side of equation (5.19) is the inverse of the conditional probability density of $\xi_1$ given the system to be in state 1:

$$\frac{\int \mathrm{d}\mathbf{x}\,\exp[-\beta\,U(\mathbf{x})]\,\theta(\xi-\xi^*)}{\int \mathrm{d}\mathbf{x}\,\exp[-\beta\,U(\mathbf{x})]\,\delta(\xi-\xi_1)\,\theta(\xi-\xi^*)} = \langle\delta(\xi-\xi_1)\rangle^{-1}_{\xi\ge\xi^*}. \tag{5.21}$$

For a good choice of $\xi_0$ and $\xi_1$, both quantities (5.20) and (5.21) can be computed as statistical averages from straightforward unconstrained MD simulations. It is reasonable to first calculate the probability distributions of $\xi$ in states 0 and 1 and only then choose the parameters $\xi_0$ and $\xi_1$. However, since the maxima of these distributions for any temperature are usually near the values obtained from zero Kelvin relaxations, one can also safely use these zero Kelvin values for $\xi_0$ and $\xi_1$. For the free energy difference (5.15) the probability densities (5.20) and (5.21) together yield the contribution

$$\Delta F_{0\to\xi_0,\,\xi_1\to 1} := -\,k_B T \ln \frac{\langle\delta(\xi-\xi_0)\rangle_{\xi\le\xi^*}}{\langle\delta(\xi-\xi_1)\rangle_{\xi\ge\xi^*}}. \tag{5.22}$$

The middle term on the right hand side of equation (5.19) is the ratio of configuration integrals, which are proportional to partition functions $Q(\xi_0)$ and $Q(\xi_1)$, respectively. The definition of $Q(\xi')$ differs from the familiar expression for the canonical partition function by a Dirac delta function,

$$Q(\xi') \propto \int \mathrm{d}\mathbf{x}\,\mathrm{d}\mathbf{p}\,\exp[-\beta\,\mathcal{H}(\mathbf{x},\mathbf{p})]\,\delta(\xi-\xi'). \tag{5.23}$$

Therefore, for the free energy difference (5.15) the middle term on the right hand side of equation (5.19) yields the contribution

$$-k_B T \ln \frac{\int \mathrm{d}\mathbf{x}\,\exp[-\beta\,U(\mathbf{x})]\,\delta(\xi-\xi_1)}{\int \mathrm{d}\mathbf{x}\,\exp[-\beta\,U(\mathbf{x})]\,\delta(\xi-\xi_0)} =: \Delta F_{\xi_0\to\xi_1}\,. \tag{5.24}$$

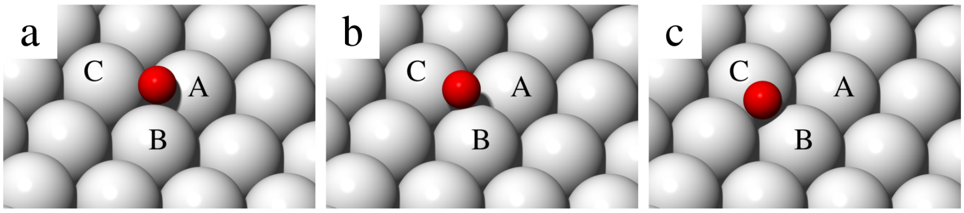

Figure 5.1: We have investigated a diffusion event where an oxygen atom (red ball) adsorbed in an hcp-hollow site (a) moves over a bridge site (b) into an fcc-hollow site (c). The distance between the oxygen atom and the rhodium atom labeled with 'A' is the variable $r$ over which the thermodynamic integration is carried out.

The free energy difference of the transition from state 0 to state 1 is computed from the contributions (5.22) and (5.24):

$$\Delta F_{0\rightarrow 1} = \Delta F_{0\rightarrow \xi_0,\, \xi_1 \rightarrow 1} + \Delta F_{\xi_0 \rightarrow \xi_1}. \tag{5.25}$$

The major contribution to $\Delta F_{0\rightarrow 1}$ is usually due to $\Delta F_{\xi_0\rightarrow\xi_1}$ which we calculate by applying thermodynamic integration (5.5).

## 5.3 Diffusion of Oxygen on Rh(111)

### 5.3.1 Free Energy Differences of Diffusion from Thermodynamic Integration

The diffusion event for which we have calculated free energies is sketched in Fig. 5.1. An oxygen atom adsorbed in an hcp-hollow site (Fig. 5.1 (a)) moves over a bridge site (b) into an fcc-hollow site (c).

We have modeled the system with a $(3\times3)$ surface cell and a slab of four rhodium layers. The calculations were carried out with a cutoff energy of 282.8 eV and the integration of the Brillouin zone was performed with a Gamma-centered $(3\times3\times1)$ k-point mesh. All calculations for this diffusion event were carried out as non spin polarized. We have tested for oxygen adsorption in the hcp-hollow site, in the fcc-hollow site, and in the bridge site, that spin polarized calculations did not yield any magnetic moment. Performing non spin polarized instead of spin polarized calculations saves about half the calculation time.

In order to calculate the free energy difference

$$\Delta F_{h\rightarrow f} = -\, k_B T \ln \frac{Z_f}{Z_h} \tag{5.26}$$

between oxygen adsorption in the hcp-hollow site (subscript '$h$') and in the fcc-hollow site (subscript '$f$') we have used only one geometric parameter $r$

in the integral (5.9), which now takes the form

$$\Delta F_{r_h \to r_f} = \int_{r_h}^{r_f} \left( \frac{\partial F}{\partial r} \right)_{r'} \mathrm{d}r'. \tag{5.27}$$

The parameter $r$ is defined as the distance between the oxygen atom and the rhodium atom which in Fig. 5.1 is labeled with 'A'. The values $r_h$ and $r_f$ were chosen to be the zero Kelvin values of the fully relaxed structures for the oxygen atom adsorbed in the hcp-hollow site and in the fcc-hollow site, respectively, for which we found $r_h = 2.016\,\text{Å}$ and $r_f = 3.463\,\text{Å}$.
The contribution (5.22) is now approximated by

$$\Delta F_{h \to r_h, r_f \to f} = -\, k_B T \ln \frac{\langle \delta(r - r_h) \rangle_{r \le r^*}}{\langle \delta(r - r_f) \rangle_{r \ge r^*}}, \tag{5.28}$$

with proper $r^*$. The exact value of $r^*$ is not needed in practical evaluation of (5.28). Instead we require that the conditions $r \le r^*$ and $r \ge r^*$ are fulfilled throughout if we start usual unconstrained MD simulations with oxygen adsorbed in the hcp-hollow site and in the fcc-hollow site, respectively. The free energy difference (5.26) is computed as

$$\Delta F_{h \to f} = \Delta F_{h \to r_h, r_f \to f} + \Delta F_{r_h \to r_f}. \tag{5.29}$$

The constrained Molecular Dynamics simulations for sampling the forces

$$\left( \frac{\partial F}{\partial r} \right)_{r'} = \langle \lambda_r \rangle_{r'}\,, \tag{5.30}$$

cf. (5.13), which are needed in order to calculate (5.27), were carried out with the Andersen thermostat [73]. Time steps of 2 fs at 10 K, 350 K, and 700 K, and of 1 fs at 1400 K were used. Equilibration runs comprised 2000 simulation steps at 10 K, 350 K, and 700 K, and 4000 steps at 1400 K, which is sufficient since we are concerned with a small system of only 38 atoms. These equilibration runs were followed by production runs of 6000 to 8000 steps at 10 K, 8000 to 12000 steps at 350 K, 10000 to 14000 steps at 700 K, and 24000 to 28000 steps at 1400 K. All 38 atoms were allowed to move in the MD simulations.
The forces (5.30) were determined at a discrete set of points $\{r_i\}$, $i = 0, 1, \ldots, n$, where $r_0 = r_h$ and $r_n = r_f$. For the purpose of comfortable notation, we define

$$g_r^{(i)} := \left( \frac{\partial F}{\partial r} \right)_{r_i}. \tag{5.31}$$

In order to compute (5.27), numerical integration was performed using the simple trapezoidal rule, which yields for the free energy difference at $r_k$

$$\Delta F_k = \frac{1}{2} \sum_{i=1}^{k} (g_r^{(i-1)} + g_r^{(i)})\,(r_i - r_{i-1}), \tag{5.32}$$

for $k = 1, 2, \dots, n$, and $\Delta F_0 = 0$.

### Statistical errors

The discrete function $\Delta F_k$ as computed by way of (5.32) depends on $(k+1)$ observables $g_r^{(0)}, \dots, g_r^{(k)}$ which are obtained from simulations and hence have statistical errors $\delta g_r^{(0)}, \dots, \delta g_r^{(k)}$. If these errors are independent and random, the error in $\Delta F_k$ is [74]

$$\delta F_k = \left( \sum_{i=1}^{k} \left( \frac{\partial(\Delta F_k)}{\partial g_r^{(i)}} \, \delta g_r^{(i)} \right)^2 \right)^{1/2} \tag{5.33}$$

for $k = 1, 2, \dots, n$, and $\delta F_0 = 0$. For the errors $\delta g_r^{(0)}, \dots, \delta g_r^{(k)}$ we take respectively the standard deviation of the mean (SDOM) which, however, needs some correction since successive system states in MD simulations are highly correlated. By dividing a sampling into blocks of length $b$, the 'statistical inefficiency' [75] is determined as

$$s = \lim_{b \to \infty} \frac{b \, \sigma_b^2}{\sigma^2}, \tag{5.34}$$

where $\sigma$ is the common standard deviation and $\sigma_b$ is the standard deviation of the mean values of the blocks of length $b$. For a sampling of $M$ values the statistical error is calculated as

$$\mathrm{SDOM} = \frac{\sigma}{\sqrt{M}} \sqrt{s}. \tag{5.35}$$

Another correction of the statistical error has to do with the Andersen thermostat. Analysis of our data clearly showed that the error could be reduced by correcting the data with respect to numerical noise caused by collisions with the thermostat. We have illustrated this for the sampling of $\lambda_r$ for a particular value of $r$ at 700 K. Let's assume that this sampling obeys the Gaussian distribution

$$\mathcal{N}(\lambda_r) = (\sigma \sqrt{2\pi})^{-1} \exp[-(\lambda_r - \bar{\lambda}_r)^2 \, (2\,\sigma^2)^{-1}], \tag{5.36}$$

with mean $\bar{\lambda}_r$ and standard deviation $\sigma$. Fig. 5.2 (a) shows that if we use the mean and the standard deviation of the sampled distribution (histogram) with (5.36), then the Gaussian distribution (red line) is not in agreement with the sampled distribution (note that Fig. 5.2 (a) does not show all of the sampled data: the minimum and maximum of the sampled data are $-13.91$ eV/Å and 12.40 eV/Å, respectively). This indicates that the statistical error is clearly overestimated when using the full data set. If however we discard data from MD steps in which collision events with the Andersen thermostat occurred, then the two distributions agree satisfactorily as shown in Fig. 5.2 (b).

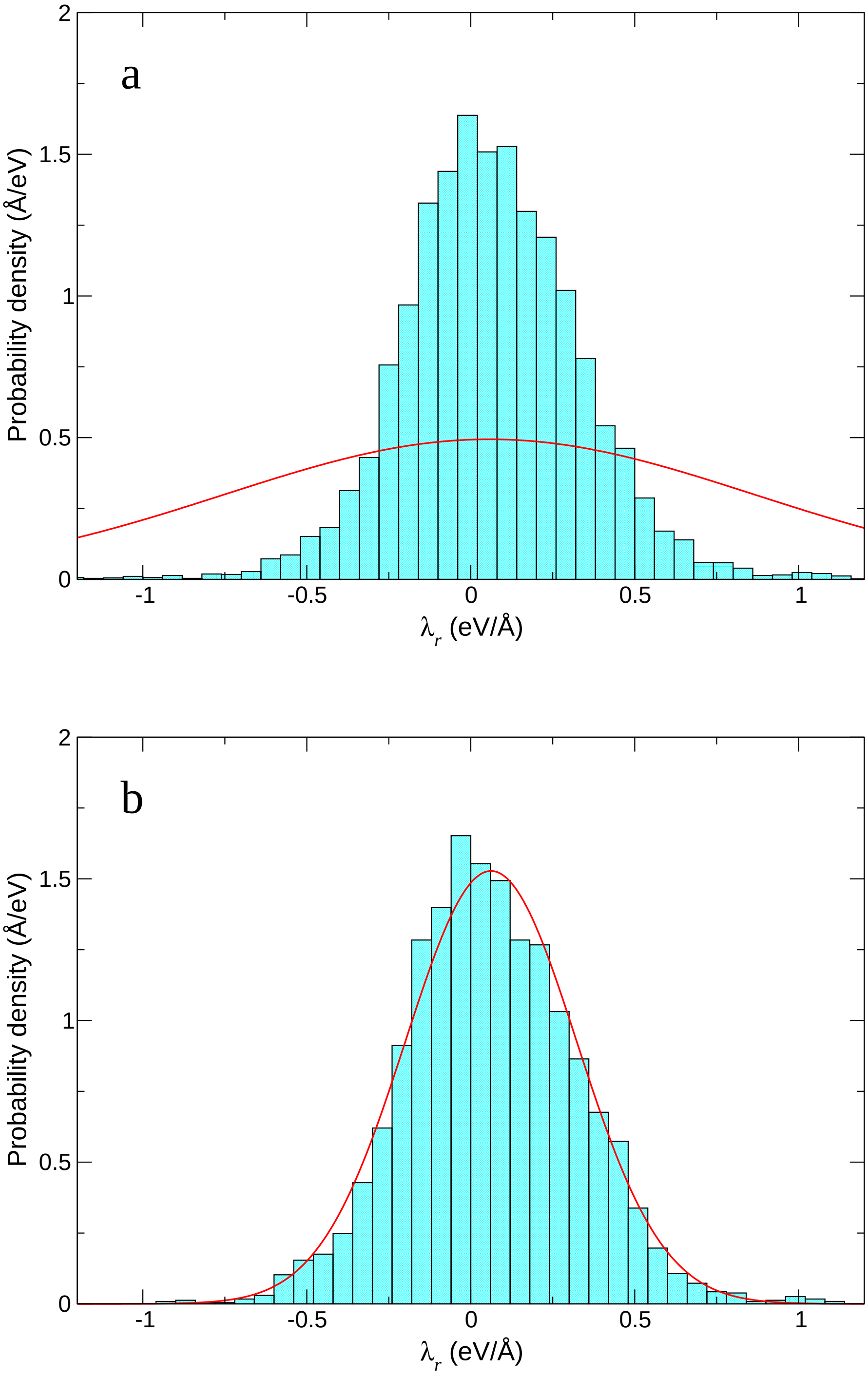

Figure 5.2: (a) Probability distribution in histogram form as obtained from sampling of $\lambda_r$ for a particular value of $r$ at 700 K, and the corresponding ideal Gaussian distribution (5.36) (red line). The minimum of the sampled data is $-13.91\,\mathrm{eV}/\mathrm{\AA}$ and the maximum is $12.40\,\mathrm{eV}/\mathrm{\AA}$. (b) The sampled data matches satisfactorily the Gaussian distribution $\mathcal{N}(\lambda_r)$ if data from collision steps is discarded. The minimum of the remaining data is $-0.91\,\mathrm{eV}/\mathrm{\AA}$ and the maximum is $1.12\,\mathrm{eV}/\mathrm{\AA}$.

It seems that only the constraint force is to such an extent sensitive to collisions of the system with the Andersen thermostat. For example, we did not find the same effect with the potential energy of the system. Neither did such effect occur with unconstrained MD simulations using the Andersen thermostat.

There are certainly collisions with several rhodium atoms which do hardly affect the value of the force to constrain the parameter $r$. Hence discarding all values from MD steps with collisions also omits desirable data. Furthermore, omitting all data from MD steps with at least one collision is not practicable if the collision probability for the Andersen thermostat has to be set to higher values such that there are virtually no MD steps without collisions. Hence it might be a good idea to detect exactly which atoms are included in collision events and to discard only MD steps where the oxygen atom and the nearest neighboring rhodium atoms are included. Since VASP currently does not tell which atom is hit by the thermostat, we chose to apply the following procedure. First, we omit all data from MD steps in which at least one collision with the Andersen thermostat occurred and find the minimum and the maximum value of the resulting distribution. Second, we take all data from the full data set which lies between those minimum and maximum values, irrespective of collisions. We found that this selection of data yields a statistical error which is smaller than if we take the full data set or only data from MD steps where no collisions occurred. This procedure was used with the constrained MD simulations for both the diffusion event and the desorption event (section 5.4).

### Results of the constrained MD simulations

A question that arises with the integration of any function for which no analytical form is known is how much integration points are needed in order to achieve a desired accuracy. To answer this question we performed the thermodynamic integration at a very low temperature, viz. 10 K, for which the contribution $TS$ to the Helmholtz free energy

$$F = E - TS \,, \tag{5.37}$$

with internal energy $E$ and entropy $S$, is very small and hence free energy and internal energy are approximately equal. Note that since the internal energy is the mean of kinetic plus potential energy, and the mean kinetic energy at constant temperature is equal for all points $\{r_i\}$, a difference of internal energies is equal to the difference of the corresponding potential energies. Fig. 5.3 (a) shows that if we use only nine integration points, the free energy difference and the internal energy difference differ by up to 48 meV, whereas (b) shows very good agreement with 45 integration points, where the deviation is merely up to 7 meV. Statistical errors of these samplings at 10 K are negligible (only about 1 meV) and hence not shown in the plots. It

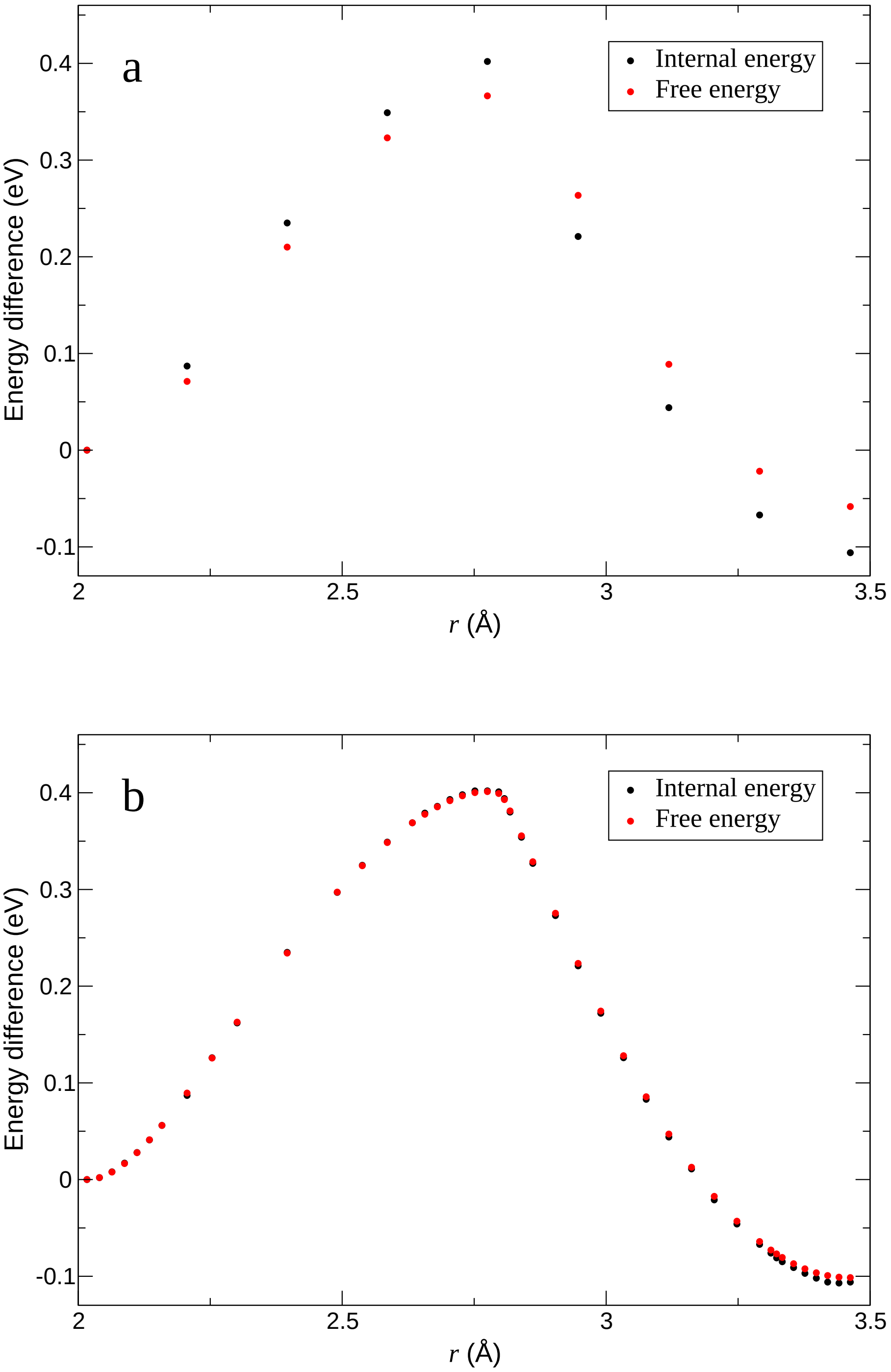

Figure 5.3: Internal energy difference (black) and free energy difference from thermodynamic integration (red, equation (5.32)) at 10 K with (a) 9 integration points and (b) 45 integration points. The deviation between the free energy difference and the internal energy difference is up to 48 meV with 9 integration points, whereas it is only up to 7 meV with 45 integration points.

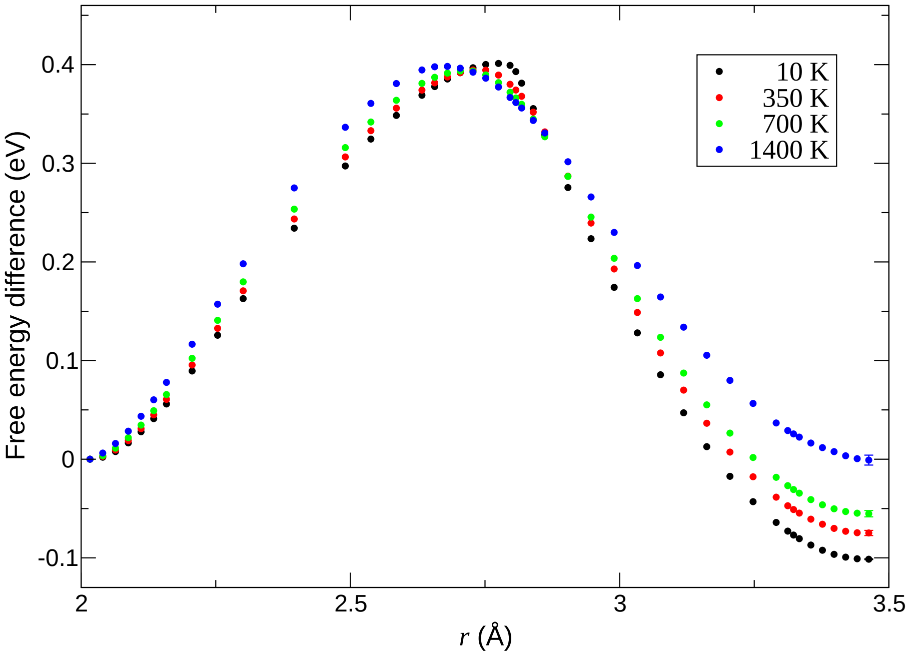

Figure 5.4: Free energy differences from thermodynamic integration from $r_h = 2.016$ Å to $r_f = 3.463$ Å via (5.32) at 10 K, 350 K, 700 K, and 1400 K. The free energy difference between the first point and the last point of one of the curves is $\Delta F_{r_h \to r_f}$. The statistical error (5.33) for this quantity is indicated with error bars.

should be emphasized that the black points in Fig. 5.3 are independent of one another, whereas the red points result from an integration and hence every red point depends on the preceding points. Consequently these results at 10 K are not only helpful in order to gauge the number of integration points, but they also show that the whole method of thermodynamic integration yields meaningful and robust results, if sufficient integration points are used.

The results of the integration for all four temperatures 10 K, 350 K, 700 K, and 1400 K are shown in Fig. 5.4. The curves show that the absolute value of the free energy difference $\Delta F_{r_h \to r_f}$ decreases with increasing temperature. Whereas this difference is about 0.1 eV at 10 K, it is virtually zero at 1400 K. However, note that $\Delta F_{r_h \to r_f}$ is not the only contribution to the free energy difference $\Delta F_{h \to f}$, which depends also on $\Delta F_{h \to r_h, r_f \to f}$. Interestingly, the maximum of the free energy shifts to smaller values of $r$ as the temperature increases. Table 5.1 displays the values of the interatomic distances between the oxygen atom and the rhodium atoms labeled 'A', 'B' and 'C' in Fig. 5.1

| | $\overline{\mathrm{AO}} = r$ | $\overline{\mathrm{BO}}$ | $\overline{\mathrm{CO}}$ |
|---|---|---|---|
| 0 K | 2.775 | 1.946 | 1.946 |
| 10 K | $2.774 \pm 0.001$ | $1.946 \pm 0.001$ | $1.946 \pm 0.001$ |
| 350 K | $2.740 \pm 0.004$ | $1.955 \pm 0.002$ | $1.952 \pm 0.002$ |
| 700 K | $2.723 \pm 0.004$ | $1.961 \pm 0.003$ | $1.962 \pm 0.003$ |
| 1400 K | $2.672 \pm 0.008$ | $1.975 \pm 0.006$ | $1.977 \pm 0.006$ |

Table 5.1: Values (in Å) of the most important interatomic distances at the maxima of the curves in Fig. 5.4. At these maxima the mean constraint force vanishes. The quantities $\overline{\mathrm{AO}}$, $\overline{\mathrm{BO}}$ and $\overline{\mathrm{CO}}$ are the distances between the oxygen atom and the rhodium atoms labeled 'A', 'B' and 'C' in Fig. 5.1.

| | 10 K | 350 K | 700 K | 1400 K |
|---|---|---|---|---|
| $\Delta F_{r_h \to r_f}$ | $-101.4 \pm 0.4$ | $-75 \pm 3$ | $-55 \pm 3$ | $-1 \pm 5$ |
| $\Delta F_{h \to r_h, r_f \to f}$ | $-0.4 \pm 0.2$ | $-18 \pm 3$ | $-25 \pm 4$ | $-74 \pm 6$ |
| $\Delta F_{h \to f}$ | $-101.8 \pm 0.4$ | $-93 \pm 4$ | $-80 \pm 5$ | $-75 \pm 8$ |

Table 5.2: Free energy difference $\Delta F_{h \to f}$ (in meV) between oxygen adsorption in the hcp-hollow site and in the fcc-hollow site.

for which the mean constraint force $\langle \partial F / \partial r \rangle$ vanishes (note that $\overline{\mathrm{AO}} = r$ was constrained in the MD simulations whereas the distances $\overline{\mathrm{BO}}$ and $\overline{\mathrm{CO}}$ were sampled as statistical averages). The value of $r$ for which $\langle \partial F / \partial r \rangle = 0$ is about 0.1 Å smaller at 1400 K than it is at 0 K. The distances $\overline{\mathrm{BO}}$ and $\overline{\mathrm{CO}}$ are equal within statistical errors, as is to be expected due to symmetry (see Fig. 5.1). The values of these distances for which $\langle \partial F / \partial r \rangle = 0$ are about 0.03 Å larger at 1400 K than they are at 0 K.

The numerical values of the contributions $\Delta F_{r_h \to r_f}$ and $\Delta F_{h \to r_h, r_f \to f}$ and of the resulting free energy difference $\Delta F_{h \to f}$ are given in Table 5.2. The absolute value of the quantity $\Delta F_{h \to f}$ seems to decrease with increasing temperature, but the statistical errors at 700 K and 1400 K are too large to make a definite assessment.

### 5.3.2 Free Energy Differences of Diffusion from a Harmonic Approximation

As discussed in section 3.2.6, in the harmonic approximation each vibrational mode is treated as a harmonic oscillator. With the vibrational frequencies $\{\nu_i\}$ the vibrational partition function is calculated as

$$Q_{\text{vib}} = \prod_i \frac{\exp[-\beta h \nu_i / 2]}{1 - \exp[-\beta h \nu_i]}. \tag{5.38}$$

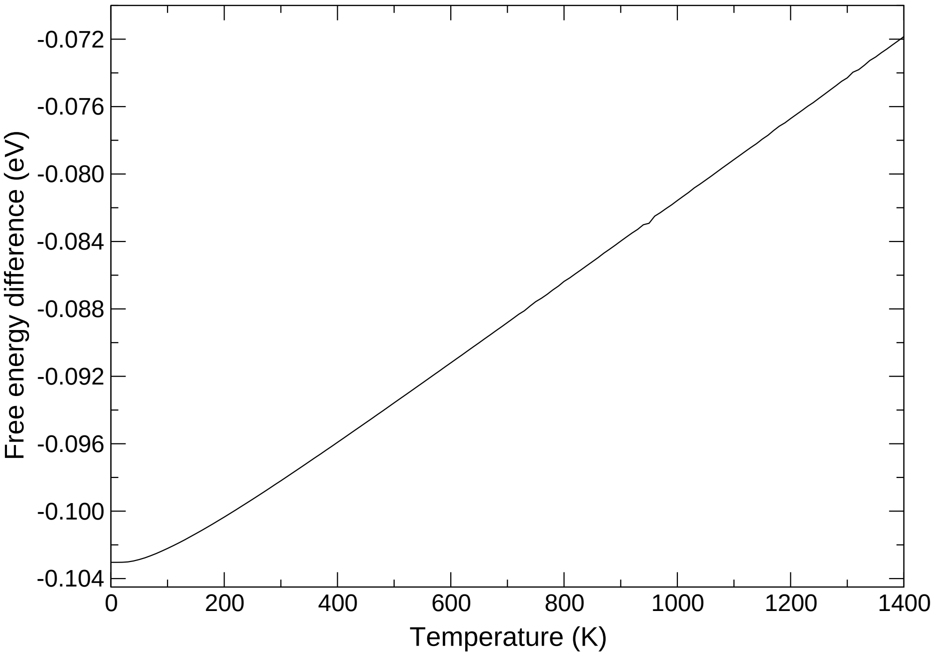

Figure 5.5: Free energy difference between the fcc-hollow site (Fig. 5.1 (c)) and the hcp-hollow site (Fig. 5.1 (a)) from the harmonic approximation (5.39) as a function of temperature.

In the case of oxygen adsorbed in an hcp-hollow site or in an fcc-hollow site on the Rh(111) surface, we are dealing with a chemisorbed system for which no translational or rotational contributions to the partition function need to be calculated. Hence we obtain the difference in free energy between the states $f$ and $h$ within the harmonic approximation as

$$F_f^{\mathrm{HA}} - F_h^{\mathrm{HA}} = U_f - U_h - k_B T \ln Q_{\mathrm{vib}}^f + k_B T \ln Q_{\mathrm{vib}}^h, \tag{5.39}$$

where $U_f$ and $U_h$ are the zero Kelvin potential energies of the system with oxygen adsorbed in the fcc-hollow site and in the hcp-hollow site, respectively. The free energy difference (5.39) as a function of temperature is shown in Fig. 5.5, and a comparison between the free energies resulting from thermodynamic integration and from the harmonic approximation is given in Table 5.3. Agreement between the approaches (5.29) and (5.39) is quite good for all temperatures, even for 1400 K.

| | 10 K | 350 K | 700 K | 1400 K |
|---|---|---|---|---|
| $\Delta F_{h \to f}$ | $-101.8 \pm 0.4$ | $-93 \pm 4$ | $-80 \pm 5$ | $-75 \pm 8$ |
| $F_f^{\mathrm{HA}} - F_h^{\mathrm{HA}}$ | $-103$ | $-97$ | $-89$ | $-72$ |

Table 5.3: Comparison of the free energy differences (in meV) resulting from thermodynamic integration (5.29) and from the harmonic approximation (5.39). The potential energy difference between oxygen adsorption in the fcc-hollow site and in the hcp-hollow site resulting from zero Kelvin relaxations is −106 meV.

## 5.4 Desorption of Oxygen from Rh(111)

### 5.4.1 Free Energy Differences of Desorption from Thermodynamic Integration

Compared with the diffusion event from the preceding section, thermodynamic integration for the desorption of oxygen from Rh(111) is much more involved. First, two geometric parameters are needed to describe the reaction coordinate, in contrast to only one parameter for the diffusion event. Second, close to the surface multiple stable domains in configuration space are compatible with the constraints and these domains can only be sampled in multiple independent simulations, especially at low temperatures. Third, these calculations need to be performed allowing for spin polarization because the $O_2$ molecule in its gas phase state has a large magnetic moment.

We calculated the free energy difference of desorption $\Delta F_{d \to g}$ between a dissociated state $d$, where the oxygens are found to be adsorbed in nearest neighboring fcc-hollow sites or in nearest neighboring hcp-hollow sites, and the gas phase state $g$, where interaction between the $O_2$ molecule and the rhodium slab is negligible. For a visualization of the reaction see the insets in Fig. 4.1.

An obvious choice for the geometric parameter over which the thermodynamic integration is performed for this process is the height of the $O_2$ molecule with respect to the rhodium surface. However, it turns out that this one parameter alone is not sufficient. We have carried out test simulations with the oxygen atoms in nearest neighboring fcc-hollow sites, where we have constrained the height of the center of mass of the two oxygen atoms with respect to the topmost rhodium layer, at a height of 1.57 Å, which is slightly more than the fully relaxed value of 1.31 Å. Whereas in simulations at 10 K the oxygen atoms stayed in the nearest neighboring fcc-hollow sites, a series of ten simulations at 1400 K showed that at this temperature the atoms leave these sites quickly and tend to maximize their distance from one another within the $(3 \times 3)$ surface cell. As a consequence we used the distance between the two oxygen atoms as a second geometric parameter for the thermodynamic integration. Let $z$ be the height of the center of mass of the oxygen atoms and $r$ their distance from one another. The thermodynamic integration is carried out from $\xi_d$ to $\xi_g$. For (5.7) we have

$$\begin{aligned} \xi(r_d, z_d) &= \xi_d, \\ \xi(r_g, z_g) &= \xi_g, \end{aligned} \tag{5.40}$$

and the integral (5.9) now takes the form

$$\Delta F_{\xi_d \to \xi_g} = \int\limits_{r_d,\,L}^{r_g} \left( \frac{\partial F}{\partial r} \right)_{r',\,z'} dr' + \int\limits_{z_d,\,L}^{z_g} \left( \frac{\partial F}{\partial z} \right)_{r',\,z'} dz'. \tag{5.41}$$

Here, the '$L$' indicates that the integrands are evaluated along a line in the coordinate system spanned by $r$ and $z$. Let the system be in state $d$ if $\xi \leq \xi^*$ and in state $g$ if $\xi \geq \xi^*$. The contribution (5.22) is for the desorption event approximated by

$$\Delta F_{d \to \xi_d,\, \xi_g \to g} = -\, k_B T \ln \frac{\langle \delta(r - r_d) \delta(z - z_d) \rangle_{\xi \leq \xi^*}}{\langle \delta(r - r_g) \delta(z - z_g) \rangle_{\xi \geq \xi^*}}. \tag{5.42}$$

The condition $\xi \leq \xi^*$ is accomplished simply by starting an unconstrained MD simulation in the dissociated state. Because of the large desorption barrier this condition is fulfilled throughout if it is fulfilled at the beginning of a simulation. On the other hand, in order to fulfill $\xi \geq \xi^*$ throughout a simulation, interaction between the $O_2$ molecule and the rhodium slab has to be avoided and any simulation showing adsorption has to be discarded. It is clear that the probability distribution of finding the $O_2$ at a particular $z$ is uniform in the space where the molecule can move freely without any interaction. The size of this space depends on the experimental conditions, which is not surprising because in the gas phase there are translational contributions to the partition function which depend on the volume accessible to the molecule. Since we do not compare our results with a particular experiment, we refer to the space between consecutive slabs in the simulations (with periodic boundary conditions) where there is virtually no interaction between the $O_2$ molecule and any of these slabs. This space is about 8.4 Å in length orthogonal to the surface, and hence the uniform probability distribution in the direction of $z$ is $(8.4\,\text{Å})^{-1}$. This means for the denominator in (5.42):

$$\langle \delta(r - r_g) \delta(z - z_g) \rangle_{\xi \geq \xi^*} = (8.4\,\text{Å})^{-1} \langle \delta(r - r_g) \rangle_{\xi \geq \xi^*}. \tag{5.43}$$

The probability density $\langle \delta(r - r_g) \rangle_{\xi \geq \xi^*}$ in (5.43) can best be computed simply by removing the rhodium slab from the simulation cell and subsequently simulating a freely vibrating $O_2$ molecule.

With (5.41) and (5.42) the free energy difference of desorption is calculated as

$$\Delta F_{d\to g} = \Delta F_{d\to \xi_d,\, \xi_g \to g} + \Delta F_{\xi_d \to \xi_g}. \tag{5.44}$$

The integrands in (5.41),

$$\left(\frac{\partial F}{\partial r}\right)_{r',\, z'} = \langle \lambda_r \rangle_{r',\, z'} \quad \text{and} \quad \left(\frac{\partial F}{\partial z}\right)_{r',\, z'} = \langle \lambda_z \rangle_{r',\, z'}, \tag{5.45}$$

are the components of the negative free energy gradient. In order to calculate (5.41), the forces (5.45) were determined at discrete points $\{(r_i,\, z_i)\}$, $i = 0, 1, \ldots, n$, in the two-dimensional coordinate system of constraints, where $(r_0,\, z_0) = (r_d,\, z_d)$ and $(r_n,\, z_n) = (r_g,\, z_g)$. We denote the components of the negative free energy gradient at $(r_i,\, z_i)$ as

$$g_r^{(i)} := \left(\frac{\partial F}{\partial r}\right)_{r_i,\, z_i}, \quad g_z^{(i)} := \left(\frac{\partial F}{\partial z}\right)_{r_i,\, z_i}. \tag{5.46}$$

Numerical integration with the trapezoidal rule yields for the free energy difference at $(r_k,\, z_k)$

$$\Delta F_k = \frac{1}{2} \sum_{i=1}^{k} \left\{ (g_r^{(i-1)} + g_r^{(i)})\,(r_i - r_{i-1}) + (g_z^{(i-1)} + g_z^{(i)})\,(z_i - z_{i-1}) \right\}, \tag{5.47}$$

for $k = 1, 2, \ldots, n$, and $\Delta F_0 = 0$. This can be written in recursion form as

$$\begin{aligned} \Delta F_0 &= 0 \\ \Delta F_k &= \Delta F_{k-1} + \frac{1}{2}\,(g_r^{(k-1)} + g_r^{(k)})\,(r_k - r_{k-1}) \\ &\quad + \frac{1}{2}\,(g_z^{(k-1)} + g_z^{(k)})\,(z_k - z_{k-1}). \end{aligned} \tag{5.48}$$

### Sampling different stable domains compatible with constraints

It turns out that for some values of the constraints $r$ and $z$, there were two or more stable regions in configuration space which are not passed by the system in one single simulation because of high energy barriers between these regions (ergodicity problem). Fig. 5.6 shows the path $\{(r_i,\, z_i)\}$ along which the integration (5.47) was carried out and an example for multiple stable regions in configuration space compatible with the same point in that path.

Since the free energy is a state function, the path in the coordinate system of constraints can be chosen arbitrarily. However, choosing a very unlikely path where 'unphysical' structures occur can result in a very bad description using DFT and cause numerical problems. We have chosen the points $\{(r_i,\, z_i)\}$ as to follow the minimum energy path obtained from a metadynamics [76] simulation (of low accuracy) at 1400 K. The first point is

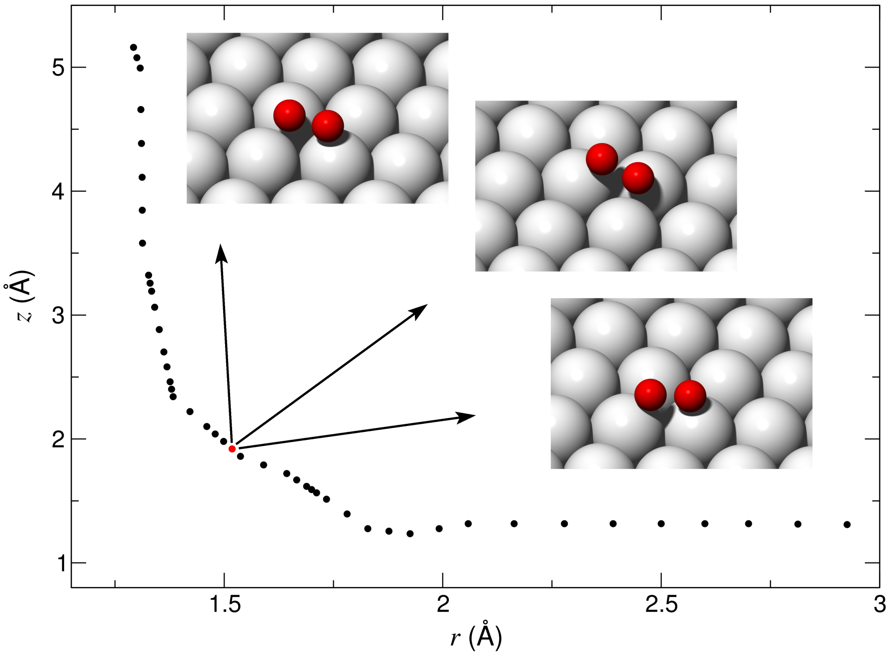

Figure 5.6: Visualization of the points $\{(r_i,\, z_i)\}$ used for the integration (5.47), and an example of multiple stable regions in configuration space (insets) compatible with the same values of the constraints (red point).

$(r_0,\, z_0) = (r_d,\, z_d) = (2.93\,\text{Å},\, 1.31\,\text{Å})$ in the lower right of the plot, and the last point is $(r_{44},\, z_{44}) = (r_g,\, z_g) = (1.29\,\text{Å},\, 5.16\,\text{Å})$ in the upper left of the plot.

The red point in Fig. 5.6 is compatible with three regions in configuration space which can only be sampled in separate MD simulations at 10 K because the separating energy barriers can not be overcome at this temperature. Yet these regions can be sampled together in a single simulation at elevated temperatures. Although we have used only 45 points for the integration (5.47), we had to perform separate constrained MD simulations in 88 stable regions of configuration space at 10 K, 71 regions at 350 K, 54 regions at 700 K, and 50 regions at 1400 K. Whereas at 10 K most of the 88 regions were sampled with production runs of only 8000 simulation steps, at 1400 K most of the 50 regions were sampled with production runs between 28000 and 36000 steps. The time step was 1 fs at 1400 K and 2 fs at lower temperatures. All atoms were allowed to move in the MD simulations.

Multiple stable regions of configuration space per point in the $(r,\, z)$ plane arise only if the oxygen atoms are very close to the surface, i.e. for low values of $z$. At a temperature of 10 K, we had to perform more than one separate constrained MD simulation per point for the first 24 points in Fig. 5.6 (starting with the point in the lower right of the plot). This number reduced to the first 22 points at 350 K, to the first 14 points at 700 K, and to the first 5 points at 1400 K. The fact that the problem of multiple stable regions of configuration space for certain values of the constraints hardly occurs at 1400 K motivates the choice of adjusting the points $\{(r_i,\, z_i)\}$ to the minimum energy path at 1400 K, and not to the minimum energy path at lower temperatures.

When there are multiple stable regions for particular values of the constraints, the question arises of how to compute the mean value of a constraint force from separate MD simulations in different regions. In a constrained MD simulation at a particular point $(r,\, z)$, the system is restricted to a subdomain $\mathbb{V}_{r,\,z}$ of configuration space. The ensemble average of an observable $O$, which is a function of only the atomic coordinates (not of the momenta), in this subdomain can be written as

$$\langle O\rangle_{r,\,z} = (Z_{r,\,z})^{-1} \int\limits_{\mathbb{V}_{r,\,z}} \mathrm{d}\mathbf{x}\, \exp[-\beta\, U(\mathbf{x})]\, O(\mathbf{x}), \tag{5.49}$$

with the potential energy function $U(\mathbf{x})$ and the configuration integral

$$Z_{r,\,z} = \int\limits_{\mathbb{V}_{r,\,z}} \mathrm{d}\mathbf{x} \exp[-\beta\, U(\mathbf{x})]. \tag{5.50}$$

Let us assume that $\mathbb{V}_{r,\,z}$ comprises $m$ regions separated by barriers, which can not be overcome in constrained MD simulations at a certain temperature in finite simulation time. We can divide $\mathbb{V}_{r,\,z}$ into non overlapping subdomains $\mathbb{V}^1_{r,\,z}$, $\mathbb{V}^2_{r,\,z}$, $\ldots$, $\mathbb{V}^m_{r,\,z}$, so that different regions to be sampled in the constrained MD simulations are found in different subdomains. In practice, if there is no switching between any of the $m$ regions in the simulations at a certain temperature, then there are areas in $\mathbb{V}_{r,\,z}$ which are never visited by the system. The 'boundaries' of the subdomains $\{\mathbb{V}^j_{r,\,z}\}$ can be drawn somewhere in these non visited areas and their exact course is not important. According to this splitting of $\mathbb{V}_{r,\,z}$, the integrals in (5.49) can be written as:

$$Z_{r,\,z} = \sum_{i=1}^{m} \int\limits_{\mathbb{V}^i_{r,\,z}} \mathrm{d}\mathbf{x}\, \exp[-\beta\, U(\mathbf{x})] =: \sum_{i=1}^{m} Z^i_{r,\,z}\,, \tag{5.51}$$

$$\langle O\rangle_{r,\,z} = \Big(\sum_{i=1}^{m} Z^i_{r,\,z}\Big)^{-1} \sum_{j=1}^{m} \int\limits_{\mathbb{V}^j_{r,\,z}} \mathrm{d}\mathbf{x}\, \exp[-\beta\, U(\mathbf{x})]\, O(\mathbf{x}). \tag{5.52}$$

If we start constrained MD simulations in the various subdomains $\mathbb{V}^1_{r,\,z}$, $\mathbb{V}^2_{r,\,z}$, $\ldots$, $\mathbb{V}^m_{r,\,z}$ at a temperature low enough as to avoid crossings of the subdomain boundaries in finite simulation time, then what we actually obtain from these separate simulations are estimates of the quantities

$$\langle O\rangle^{j}_{r,\,z} \;:=\; (Z^{j}_{r,\,z})^{-1} \int\limits_{\mathbb{V}^{j}_{r,\,z}} \mathrm{d}\mathbf{x}\, \exp[-\beta\, U(\mathbf{x})]\, O(\mathbf{x}), \quad j = 1, 2\,\ldots, m. \tag{5.53}$$

The problem is, how can the mean values $\{\langle O\rangle^{j}_{r,\,z}\}$, as obtained from separate constrained MD simulations in different subdomains of $\mathbb{V}_{r,\,z}$, be combined to get the desired ensemble average $\langle O\rangle_{r,\,z}$.
With (5.53), the overall mean value (5.52) can be rewritten as

$$\langle O\rangle_{r,\,z} \;=\; \frac{\sum_{j=1}^{m} Z^{j}_{r,\,z}\,\langle O\rangle^{j}_{r,\,z}}{\sum_{i=1}^{m} Z^{i}_{r,\,z}} \;=:\; \sum_{j=1}^{m} p^{j}_{r,\,z}\langle O\rangle^{j}_{r,\,z}\,, \tag{5.54}$$

with the probabilities

$$p^{j}_{r,\,z} \;=\; \frac{Z^{j}_{r,\,z}}{\sum_{i=1}^{m} Z^{i}_{r,\,z}}. \tag{5.55}$$

The canonical partition function $Q_{NVT}$ and the Helmholtz free energy $F = E - TS$, with internal energy $E$ and entropy $S$, are related via

$$F = -k_B T \ln Q_{NVT} \quad \Longleftrightarrow \quad Q_{NVT} = \exp[-\beta\, F], \tag{5.56}$$

which implies for the configuration integral

$$Z \;=\; \mathrm{C}\exp[-\beta\, F], \tag{5.57}$$

with a constant C of no importance, since we always use $Z$ in expressions where it appears in both nominator and denominator of a fraction and therefore C is canceled. Equation (5.57) is also valid for every arbitrary subdomain $\mathbb{V}^{i}_{r,\,z}$,

$$Z^{i}_{r,\,z} \;=\; \int\limits_{\mathbb{V}^{i}_{r,\,z}} \mathrm{d}\mathbf{x}\, \exp[-\beta\, U(\mathbf{x})] \;\propto\; \exp[-\beta\, F^{i}_{r,\,z}], \tag{5.58}$$

where $F^{i}_{r,\,z} = E^{i}_{r,\,z} - TS^{i}_{r,\,z}$ is the "free energy of subdomain $i$" and $S^{i}_{r,\,z}$ is the "entropy of subdomain $i$". Using (5.58) with (5.55) yields

$$p^{j}_{r,\,z} \;=\; \frac{\exp[-\beta\, F^{j}_{r,\,z}]}{\sum_{i=1}^{m} \exp[-\beta\, F^{i}_{r,\,z}]} \;=\; \frac{\exp[-\beta\, E^{j}_{r,\,z}]\, \exp[S^{j}_{r,\,z}/k]}{\sum_{i=1}^{m} \exp[-\beta\, E^{i}_{r,\,z}]\, \exp[S^{i}_{r,\,z}/k]}\,. \tag{5.59}$$

The internal energies $\{E^{i}_{r,\,z}\}$ can easily be obtained from the constrained MD simulations, whereas the entropies $\{S^{i}_{r,\,z}\}$ can not. Therefore we introduce the approximation of equal entropies $S^{1}_{r,\,z} = S^{2}_{r,\,z} = \ldots = S^{m}_{r,\,z}$ of the subdomains $\mathbb{V}^{1}_{r,\,z}$, $\mathbb{V}^{2}_{r,\,z}$, …, $\mathbb{V}^{m}_{r,\,z}$. Applying this approximation means that the accessible phase space volumes of simulations in different subdomains are considered to be of equal size. With this assumption (5.59) becomes

$$p^j_{r,\,z} \approx \frac{\exp[-\beta\, E^j_{r,\,z}]}{\sum_{i=1}^m \exp[-\beta\, E^i_{r,\,z}]}\,. \tag{5.60}$$

The internal energy is the expectation value of the Hamiltonian $\mathcal{H} = E_{kin}(\mathbf{p}) + U(\mathbf{x})$, i.e. the mean of kinetic plus potential energy:

$$E^i_{r,\,z} = \langle \mathcal{H} \rangle^i_{r,\,z} = \langle E_{kin} + U \rangle^i_{r,\,z} = \langle E_{kin} \rangle^i_{r,\,z} + \langle U \rangle^i_{r,\,z}. \tag{5.61}$$

Hence the probabilities (5.60) become

$$p^j_{r,\,z} \approx \frac{\exp[-\beta\, \langle E_{kin} \rangle^j_{r,\,z}]\ \exp[-\beta\, \langle U \rangle^j_{r,\,z}]}{\sum_{i=1}^m \exp[-\beta\, \langle E_{kin} \rangle^i_{r,\,z}]\ \exp[-\beta\, \langle U \rangle^i_{r,\,z}]}\,. \tag{5.62}$$

Since we perform constrained MD simulations at constant temperature, the mean kinetic energies of all subdomains are equal, $\langle E_{kin} \rangle^1_{r,\,z} = \langle E_{kin} \rangle^2_{r,\,z} = \cdots = \langle E_{kin} \rangle^m_{r,\,z}$, and the corresponding exponential terms in (5.62) cancel, leaving

$$p^j_{r,\,z} \approx \frac{\exp[-\beta\, \langle U \rangle^j_{r,\,z}]}{\sum_{i=1}^m \exp[-\beta\, \langle U \rangle^i_{r,\,z}]}\,. \tag{5.63}$$

In summary, we calculate the probabilities (5.63) to obtain the ensemble average $\langle O \rangle_{r,\,z}$ from the means $\{\langle O \rangle^j_{r,\,z}\}$ by way of (5.54) as

$$\langle O \rangle_{r,\,z} \approx \left( \sum_{i=1}^m \exp[-\beta\, \langle U \rangle^i_{r,\,z}] \right)^{-1} \sum_{j=1}^m \exp[-\beta\, \langle U \rangle^j_{r,\,z}]\, \langle O \rangle^j_{r,\,z}. \tag{5.64}$$

Whenever there were multiple stable regions of configuration space compatible with the constraints, we used this formula for $O = \lambda_r$ and $O = \lambda_z$.
We want to emphasize that by using (5.64) we assume equal entropies only for subdomains of $\mathbb{V}_{r,\,z}$, which is related to fixed values of the constraints $r$ and $z$. We do not assume equal entropies for subdomains of the full configuration space. The entire derivation from (5.49) to (5.64) could also be made without the subscript '$r$, $z$' for an ensemble average $\langle O \rangle$ over the full configuration space, but assuming equal entropies in subdomains of the full configuration space would in general be a very bad approximation. Furthermore it would make the use of thermodynamic integration absurd since in this case free energy differences would be equal to internal energy differences which could be calculated very easily. Nevertheless, in one specific case we have used an approximation analogous to (5.64) for two subdomains of the full configuration space. For $\xi = \xi_d$ the oxygen atoms can be adsorbed in nearest neighboring fcc-hollow sites or in nearest neighboring hcp-hollow sites. Using ordinary unconstrained MD simulations we have calculated the

probability density $\langle \delta(r - r_d)\delta(z - z_d)\rangle_{\xi \leq \xi^*}$ analogous to (5.64) in order to compute $\Delta F_{d \to \xi_d, \xi_g \to g}$ via (5.42).

In order to find the stable regions in $\mathbb{V}_{r,z}$ we have visually inspected constrained MD simulations at rather high temperatures, where switches between these regions do occur, and we have taken symmetries of the Rh(111) surface into account. We are therefore confident that we have succeeded in finding the most relevant subdomains of $\mathbb{V}_{r,z}$. Omitting energetically very unfavorable subdomains does have little effect on the results, as can be seen from (5.63) and (5.54).

### Statistical errors

Analogous to (5.33), the statistical error in $\Delta F_k$ ((5.47) and (5.48)) is

$$\begin{aligned} \delta F_k &= \left( \sum_{i=1}^{k} \left\{ \left( \frac{\partial(\Delta F_k)}{\partial g_r^{(i)}} \, \delta g_r^{(i)} \right)^2 + \left( \frac{\partial(\Delta F_k)}{\partial g_z^{(i)}} \, \delta g_z^{(i)} \right)^2 \right\} \right)^{1/2} \\ &= \Big( (\delta F_{k-1})^2 + \frac{1}{4} (r_k - r_{k-1})^2 \left[ (\delta g_r^{(k-1)})^2 + (\delta g_r^{(k)})^2 \right] \\ &\qquad + \frac{1}{4} (z_k - z_{k-1})^2 \left[ (\delta g_z^{(k-1)})^2 + (\delta g_z^{(k)})^2 \right] \Big)^{1/2}, \end{aligned} \tag{5.65}$$

for $k = 1, 2, \ldots, n$, and $\delta F_0 = 0$. The errors $\delta g_r^{(0)}, \ldots, \delta g_r^{(k)}, \delta g_z^{(0)}, \ldots, \delta g_z^{(k)}$ are respectively the standard deviation of the mean (5.35). However, some of these errors must be determined for mean values according to (5.64) (with $O = \lambda_r$ or $O = \lambda_z$ and hence $\langle O \rangle_{r,z} = g_r$ or $\langle O \rangle_{r,z} = g_z$, respectively) obtained from separate constrained MD simulations in multiple stable regions of configuration space. These simulations yield independent statistical errors $\{\delta\langle O \rangle_{r,z}^j\}$, and by means of (5.64) the statistical average $\langle O \rangle_{r,z}$ is calculated not only from the quantities $\{\langle O \rangle_{r,z}^j\}$, but the potential energies $\{\langle U \rangle_{r,z}^j\}$ are introduced as additional observables with statistical errors $\{\delta\langle U \rangle_{r,z}^j\}$. Hence, to estimate the error $\delta\langle O \rangle_{r,z}$ in $\langle O \rangle_{r,z}$, error propagation of $\{\delta\langle O \rangle_{r,z}^j\}$ as well as of $\{\delta\langle U \rangle_{r,z}^j\}$ needs to be taken into account. For independent and random errors $\{\delta\langle O \rangle_{r,z}^j\}$ and $\{\delta\langle U \rangle_{r,z}^j\}$, the error in $\langle O \rangle_{r,z}$ is [74]

$$\delta\langle O \rangle_{r,z} = \left( \sum_{j=1}^{m} \left\{ \left( \frac{\partial\langle O \rangle_{r,z}}{\partial\langle O \rangle_{r,z}^j} \, \delta\langle O \rangle_{r,z}^j \right)^2 + \left( \frac{\partial\langle O \rangle_{r,z}}{\partial\langle U \rangle_{r,z}^j} \, \delta\langle U \rangle_{r,z}^j \right)^2 \right\} \right)^{1/2}, \tag{5.66}$$

where $O \neq U$. Using (5.66) with (5.64) yields

$$\begin{aligned}
\delta\langle O\rangle_{r,\,z} \;&=\; \left(\sum_{i=1}^{m}\exp[-\beta\,\langle U\rangle_{r,\,z}^{i}]\right)^{-1}\left(\sum_{j=1}^{m}\exp[-2\beta\,\langle U\rangle_{r,\,z}^{j}]\,\Big\{(\delta\langle O\rangle_{r,\,z}^{j})^2\right.\\
&\qquad\left.+\,\beta^2\,(\langle O\rangle_{r,\,z}-\langle O\rangle_{r,\,z}^{j})^2\,(\delta\langle U\rangle_{r,\,z}^{j})^2\Big\}\right)^{1/2}. \qquad (5.67)
\end{aligned}$$

Equations (5.66) and (5.67) are not valid for $O = U$. Applying (5.64) for the potential energy $O = U$, the error is

$$\begin{aligned}
\delta\langle U\rangle_{r,\,z} \;&=\; \left(\sum_{j=1}^{m}\left(\frac{\partial\langle U\rangle_{r,\,z}}{\partial\langle U\rangle_{r,\,z}^{j}}\,\delta\langle U\rangle_{r,\,z}^{j}\right)^2\right)^{1/2}\\
&=\; \left(\sum_{i=1}^{m}\exp[-\beta\,\langle U\rangle_{r,\,z}^{i}]\right)^{-1}\left(\sum_{j=1}^{m}\exp[-2\beta\,\langle U\rangle_{r,\,z}^{j}]\right.\\
&\qquad\left.\times\,[1+\beta\,(\langle U\rangle_{r,\,z}-\langle U\rangle_{r,\,z}^{j})]^2\,(\delta\langle U\rangle_{r,\,z}^{j})^2\right)^{1/2}. \qquad (5.68)
\end{aligned}$$

**Results of the constrained MD simulations**

Fig. 5.7 shows that we obtained good agreement between the internal energy difference and the free energy difference at 10 K using 45 integration points for the numerical integration (5.47).

The results of the integration for all four temperatures 10 K, 350 K, 700 K, and 1400 K are shown in Fig. 5.8. However, whereas the curve in Fig. 5.7 was calculated with a rhodium slab of four layers and the same numerical setting as the curves for the diffusion event, due to the tremendous costs in computation time the four curves of Fig. 5.8 were calculated with a rhodium slab of only three layers and a 'cheaper' numerical setting. By changing the 'PREC' tag (standing for 'precision') in VASP from 'Normal' to 'Low', the cutoff energy was decreased from 282.8 eV to 212.1 eV, and the number of grid points in the FFT mesh was reduced. It will be shown in the next subsection how a correction term can be obtained from *free energy perturbation* which compensates the usage of 'PREC = Low'.

As shown by the curves in Fig. 5.8, the free energy difference $\Delta F_{\xi_d \rightarrow \xi_g}$ decreases with increasing temperature, namely from approximately 4.27 eV at 10 K to 3.97 eV at 350 K, 3.81 eV at 700 K, and 3.46 eV at 1400 K. The statistical error (5.65) in $\Delta F_{\xi_d \rightarrow \xi_g}$ is indicated for each curve, but even at 1400 K the statistical error interval of ±22 meV is smaller than the diameter of the points which we have chosen for the illustration of the curves.

All four curves exhibit a small decrease at the last three points. A comparison with the free energy curve in Fig. 5.7, which was calculated with

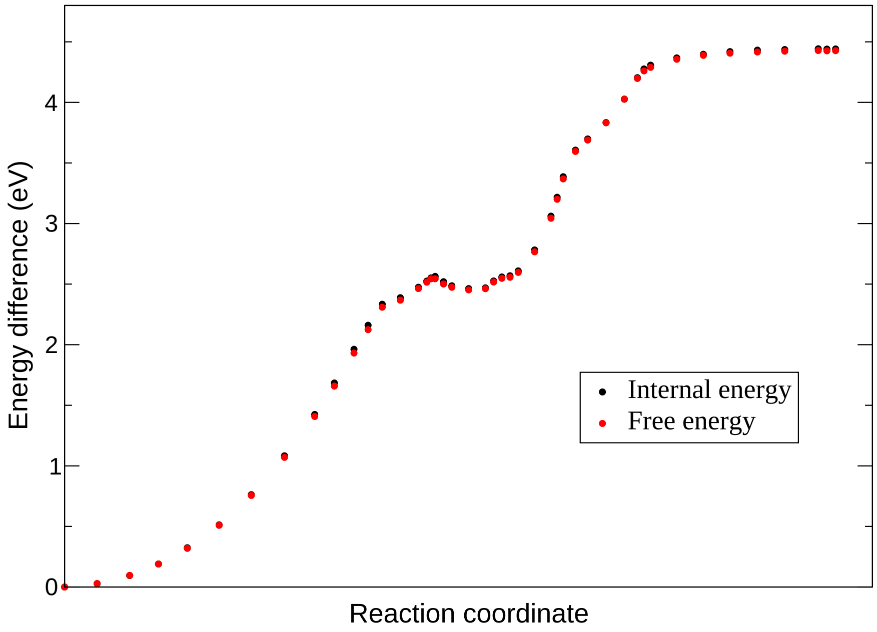

Figure 5.7: Internal energy difference (black) and free energy difference from thermodynamic integration (red, equation (5.47)) at 10 K with 45 integration points, calculated with a rhodium slab of four layers.

four layers of rhodium and the setting 'PREC = Normal', shows that this is due to the use of only three layers of rhodium or the less accurate numerical setting 'PREC = Low' (or both). As will be shown below, it turns out that the use of 'PREC = Normal' with only three layers of rhodium almost completely restores the right behavior of the curves at the last three points.

### 5.4.2 Corrections from Free Energy Perturbation

In order to add a correction which compensates the use of less accurate numerical parameters in the constrained MD simulations for the desorption event, we applied free energy perturbation (FEP) [77, 78]. If we perform MD simulations in a particular stable region of configuration space with a less accurate setting (subscript 'PL' for 'PREC = Low' used by VASP) and with a more accurate setting (subscript 'PN' for 'PREC = Normal'), we find

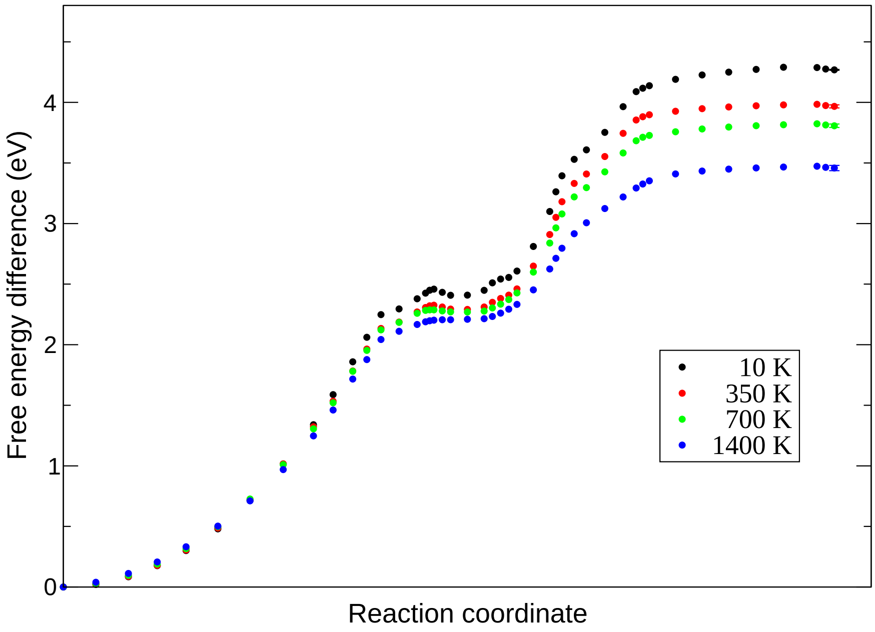

Figure 5.8: Free energy differences from thermodynamic integration from $(r_d,\, z_d)$ to $(r_g,\, z_g)$ via (5.47) at 10 K, 350 K, 700 K, and 1400 K, calculated with a rhodium slab of three layers and the numerical setting 'PREC = Low' used by VASP. The free energy difference between the first point and the last point of one of the curves is $\Delta F_{\xi_d \to \xi_g}$ (see equation (5.41)). The statistical error (5.65) for this quantity is indicated with error bars.

a change in the free energy according to

$$\begin{aligned} F_{\rm PN} - F_{\rm PL} &= -k_B T \ln \frac{Z_{\rm PN}}{Z_{\rm PL}} \\ &= -k_B T \ln \frac{\int \mathrm{d}\mathbf{x}\, \exp[-\beta\, U_{\rm PN}(\mathbf{x})]}{\int \mathrm{d}\mathbf{x}\, \exp[-\beta\, U_{\rm PL}(\mathbf{x})]} \\ &= -k_B T \ln \frac{\int \mathrm{d}\mathbf{x}\, \exp[-\beta\, (U_{\rm PN}(\mathbf{x}) - U_{\rm PL}(\mathbf{x}))]\, \exp[-\beta\, U_{\rm PL}(\mathbf{x})]}{\int \mathrm{d}\mathbf{x}\, \exp[-\beta\, U_{\rm PL}(\mathbf{x})]} \\ &= -k_B T \ln \left\langle \exp[-\beta\, (U_{\rm PN}(\mathbf{x}) - U_{\rm PL}(\mathbf{x}))] \right\rangle_{\rm PL}. \end{aligned} \tag{5.69}$$

Hence the ratio $Z_{\rm PN}/Z_{\rm PL}$ can be obtained by calculating the thermal average of $\exp[-\beta\, (U_{\rm PN}(\mathbf{x}) - U_{\rm PL}(\mathbf{x}))]$ from the probability distribution given by $\exp[-\beta\, U_{\rm PL}(\mathbf{x})]/Z_{\rm PL}$ which results from the less accurate numerical setting 'PREC = Low'. In practice, we take a sufficiently large number of configurations out of a trajectory generated with the potential $U_{\mathrm{PL}}$ and recalculate their energies with both potentials $U_{\mathrm{PL}}$ and $U_{\mathrm{PN}}$.

The method only yields reliable results if the trajectory in configuration space generated with the potential $U_{\mathrm{PL}}$ is also a typical trajectory for potential $U_{\mathrm{PN}}$. That is, the more the probability distribution $\exp[-\beta\, U_{\mathrm{PN}}(\mathbf{x})]/Z_{\mathrm{PN}}$ differs from the probability distribution $\exp[-\beta\, U_{\mathrm{PL}}(\mathbf{x})]/Z_{\mathrm{PL}}$, the worse the result obtained from (5.69).

In order to obtain a correction for the free energy differences resulting from the setting 'PREC = Low', FEP according to (5.69) needs to be applied for $\xi = \xi_g$ as well as for $\xi = \xi_d$. The contribution that needs to be added to the free energy difference $\Delta F_{\xi_d \to \xi_g}$ obtained from thermodynamic integration with the setting 'PREC = Low' is

$$\Delta F_{\mathrm{PL}\to\mathrm{PN}} := (F_{\mathrm{PN}}(\xi_g) - F_{\mathrm{PL}}(\xi_g)) - (F_{\mathrm{PN}}(\xi_d) - F_{\mathrm{PL}}(\xi_d)) = -k_B T \ln \frac{\big\langle \exp[-\beta\,(U_{\mathrm{PN}}(\mathbf{x}) - U_{\mathrm{PL}}(\mathbf{x}))]\,\delta(\xi - \xi_g)\big\rangle_{\mathrm{PL}}}{\big\langle \exp[-\beta\,(U_{\mathrm{PN}}(\mathbf{x}) - U_{\mathrm{PL}}(\mathbf{x}))]\,\delta(\xi - \xi_d)\big\rangle_{\mathrm{PL}}}. \tag{5.70}$$

Note that, since for $\xi = \xi_d$ there are two stable domains in configuration space which can only be sampled separately even at 1400 K, the statistical average in the denominator of (5.70) was calculated according to (5.64).

Since at a temperature of 10 K thermodynamic integration with both settings 'PREC = Low' and 'PREC = Normal' is feasible, the reliability of the results from FEP can be tested. Fig. 5.9 shows a comparison between free energy differences obtained from FEP with those obtained from thermodynamic integration (TI) for three different values of the constraints. If FEP and TI are in perfect agreement, then the green and the red points coincide. The deviation between the green and the red points is only 0.017 eV, 0.025 eV, and 0.023 eV, respectively, i.e. we have found very good agreement between FEP and TI at 10 K.

The contribution (5.70) turns out to be quite similar for all four temperatures, namely −0.188 eV at 10 K, −0.205 eV at 350 K, −0.204 eV at 700 K, and −0.194 eV at 1400 K, where the statistical error is merely about 1 meV for each of the four results.

Table 5.4 gives the free energy difference of desorption (5.44) including the correction from FEP (5.70) for the quantity $\Delta F_{\xi_d \to \xi_g}$. The contribution $\Delta F_{d \to \xi_d, \xi_g \to g}$ was calculated with unconstrained MD simulations using three layers of rhodium and the setting 'PREC = Normal'. Unfortunately, the numbers in Table 5.4 are not converged with respect to the thickness of the rhodium slab. Using three layers of rhodium and the numerical setting 'PREC = Normal' with thermodynamic integration at 10 K, the free energy difference $\Delta F_{\xi_d \to \xi_g}$ is predicted to be about 4.06 eV (red curve in Fig. 5.9). Using four layers of rhodium with the same numerical setting, it is predicted to be 4.43 eV (red curve in Fig. 5.7). We must therefore conclude that our

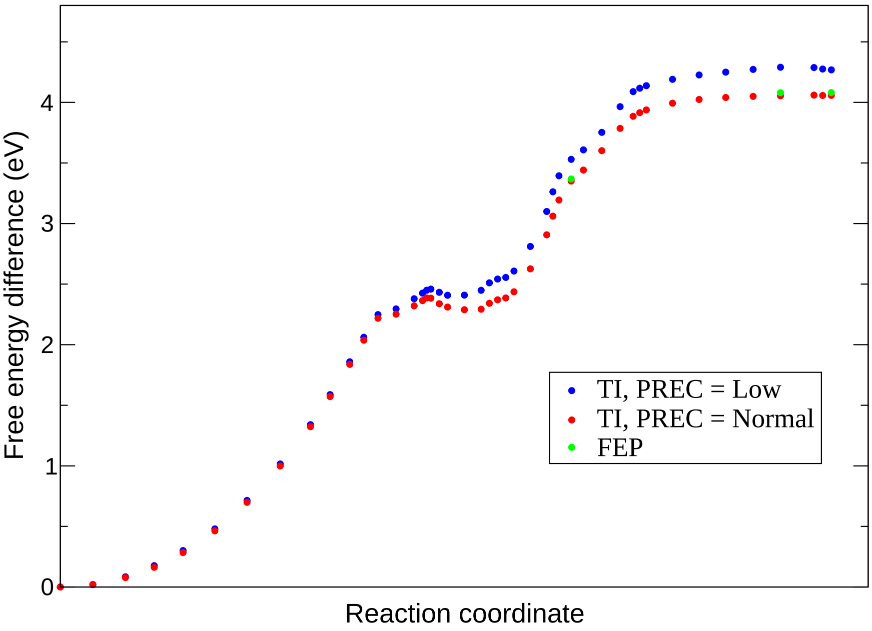

Figure 5.9: Comparison between free energy perturbation (FEP) and thermodynamic integration (TI) at 10 K (using three layers of rhodium). The blue curve was obtained from TI with the less accurate numerical setting 'PREC = Low', whereas the red curve was obtained with the more accurate setting 'PREC = Normal'. The green points give respectively the difference between the two curves according to FEP, i.e. for perfect agreement between FEP and TI the green points and the red points would coincide.

| | 10 K | 350 K | 700 K | 1400 K |
|---|---|---|---|---|
| $\Delta F_{\xi_d \to \xi_g}$ | $4269 \pm 4$ | $3967 \pm 13$ | $3807 \pm 14$ | $3458 \pm 22$ |
| $\Delta F_{d \to \xi_d,\, \xi_g \to g}$ | $-3 \pm 1$ | $-66 \pm 7$ | $-100 \pm 12$ | $-129 \pm 31$ |
| $\Delta F_{\mathrm{PL} \to \mathrm{PN}}$ | $-188 \pm 1$ | $-205 \pm 1$ | $-204 \pm 1$ | $-194 \pm 1$ |
| $\Delta F_{d \to g}$ | $4078 \pm 4$ | $3696 \pm 15$ | $3503 \pm 18$ | $3135 \pm 38$ |

Table 5.4: Free energy difference of desorption $\Delta F_{d \to g}$ (in meV) including the correction from free energy perturbation (equations (5.44) and (5.70)).

results in Table 5.4 are not converged with respect to the number of rhodium layers.

### 5.4.3 Free Energy Differences of Desorption from a Harmonic Approximation

The free energy difference of desorption obtained from thermodynamic integration can be compared with the free energy difference of desorption obtained from a harmonic approximation. The translational partition function for the free $O_2$ molecule depends on the accessible volume and is calculated as

$$Q^{\mathrm{tr}}_{\mathrm{O}_2}(T, V) = \left(\frac{2\pi m k_B T}{h^2}\right)^{3/2} V, \tag{5.71}$$

where $m$ is the mass of $O_2$. Since we want to compare this approach with the thermodynamic integration, we have to use the same volume $V$ as for the calculation of the probability density $\langle \delta(r - r_g)\delta(z - z_g)\rangle_{\xi \geq \xi^*}$ in (5.42), where we allowed the molecule to move freely in the space between consecutive slabs in which it does not interact with any of the slabs. We determined this space to be 8.4 Å in length orthogonal to the surface. This length multiplied by the surface area in the simulation cell (57.5 $\text{Å}^2$) yields the volume $V$ in (5.71). The rotational partition function for the free $O_2$ molecule is

$$Q^{\mathrm{rot}}_{\mathrm{O}_2}(T) = T(2\theta)^{-1}, \tag{5.72}$$

where $\theta$ is the *characteristic rotational temperature* (value $\theta = 2.08\,\mathrm{K}$ taken from [20], p. 933). As already discussed in Chapter 3, in the harmonic approximation for each vibrational mode the partition function of the harmonic oscillator (3.17) is used. With the vibrational partition functions $Q^{\mathrm{vib}}_{\mathrm{O}_2}(T)$ for the free $O_2$ and $Q^{\mathrm{vib}}_{\mathrm{slab}}(T)$ for the clean rhodium slab, the free energy of the system with the oxygen molecule in the gas state is, in harmonic approximation (HA), calculated as

$$F^{\mathrm{HA}}_g = U_{\mathrm{slab}} + U_{\mathrm{O}_2} - k_B T \ln(Q^{\mathrm{tr}}_{\mathrm{O}_2} Q^{\mathrm{rot}}_{\mathrm{O}_2} Q^{\mathrm{vib}}_{\mathrm{O}_2} Q^{\mathrm{vib}}_{\mathrm{slab}}), \tag{5.73}$$

where $U_{\mathrm{slab}}$ and $U_{\mathrm{O}_2}$ are the zero Kelvin potential energies of the fully relaxed clean rhodium slab and $O_2$ molecule, respectively. Note that we have performed the calculations for the free $O_2$ molecule (in order to determine the potential energy and the vibrational frequency) with a numerical setting consistent with the setting for the thermodynamic integration, whereas calculations for isolated $O_2$ are usually carried out with a more accurate numerical setting, among other things with a significantly larger cutoff energy. We have computed the free energy for the dissociated state, where the two oxygen atoms are adsorbed in neighboring fcc-hollow sites, with the potential energy $U_{\mathrm{slab+2O}}$ and the vibrational partition function $Q^{\mathrm{vib}}_{\mathrm{slab+2O}}$ as

$$F^{\mathrm{HA}}_d = U_{\mathrm{slab+2O}} - k_B T \ln(Q^{\mathrm{vib}}_{\mathrm{slab+2O}}). \tag{5.74}$$

The free energy difference between the dissociated state and the gas phase state is then calculated as the difference between (5.73) and (5.74).

| | 10 K | 350 K | 700 K | 1400 K |
|---|---|---|---|---|
| $\Delta F_{d\rightarrow g}$ | $4078 \pm 4$ | $3696 \pm 15$ | $3503 \pm 18$ | $3135 \pm 38$ |
| $F_g^{\mathrm{HA}} - F_d^{\mathrm{HA}}$ | 4073 | 3614 | 3163 | 2372 |
| Deviation | $-5 \pm 4$ | $-82 \pm 15$ | $-340 \pm 18$ | $-763 \pm 38$ |

Table 5.5: Free energy differences (in meV) between the gas phase state (state g) and the dissociated state (state d). $\Delta F_{d\rightarrow g}$ is the energy resulting from thermodynamic integration (cf. Table 5.4) and $F_g^{\mathrm{HA}} - F_d^{\mathrm{HA}}$ is the energy from the harmonic approximation. The zero Kelvin potential energy difference between state g and state d is 4145 meV.

Table 5.5 shows the free energy differences $F_g^{\mathrm{HA}} - F_d^{\mathrm{HA}}$ resulting from the harmonic approximation and a comparison with the free energy differences $\Delta F_{d\rightarrow g}$ from the thermodynamic integration. The agreement between the two approaches is very good at 10 K, where the deviation is only a few meV. Although the temperature of 10 K is very low, the good agreement between thermodynamic integration and harmonic approximation is not to be taken for granted, as is indicated by the fact that both values at 10 K (4.078 eV and 4.073 eV) differ significantly more from the zero Kelvin potential energy difference of 4.145 eV than they differ from each other. The agreement between the two approaches is also satisfactory at 350 K, where the deviation is between 2 and 3 percent. At 700 K the deviation is already about 10 percent, and for 1400 K thermodynamic integration and the harmonic approximation predict quite different energies.

## 5.5 Summary

We have calculated free energy differences using thermodynamic integration for diffusion of oxygen on Rh(111) and for the associative desorption of oxygen from the Rh(111) surface. In case of diffusion the integration could be carried out over one geometric parameter, whereas for the desorption event two parameters were necessary, namely the bondlength between the two oxygen atoms and the height of the center of mass of the oxygens with respect to the topmost rhodium layer.

The calculations were carried out at 10 K, 350 K, 700 K, and 1400 K since experimental TPD spectra show desorption at temperatures up to approximately 1400 K. Performing calculations at the very low temperature of 10 K was very helpful for gauging the reliability of the methods. In order to determine the number of integration points we have compared the free energy differences at 10 K with the internal energy differences. The very good agreement between these differences showed that the results obtained from thermodynamic integration are meaningful.

Statistical errors taking error propagation and correlation into account were computed. Numerical noise in the distributions of the constraint forces caused by collisions with the Andersen thermostat was removed.

In case of desorption, for particular values of the constraints multiple stable regions in configuration space were found which could only be sampled in separate constrained MD simulations, especially at low temperatures. In order to calculate the overall ensemble average from these separate simulations, we have introduced the approximation of equal entropies of the subdomains for fixed values of the constraints.

Thermodynamic integration for desorption was performed with a numerical setting of low accuracy. Applying free energy perturbation we could determine correction terms compensating the low accuracy of the numerical setting.

We have compared the free energies obtained from thermodynamic integration with free energies obtained from a harmonic approximation. In case of the diffusion event, agreement between these approaches is satisfactory at all four temperatures and in particular very good at 1400 K. Consequently it is sufficient for this kind of reaction to use the computationally much less demanding approach of the harmonic approximation. In case of the desorption event, the agreement between the approaches is only satisfactory at 10 K and 350 K. For 1400 K the two methods predict quite different free energy differences.

The calculations for the desorption process were carried out with a slab of three rhodium layers. Unfortunately, free energy curves of desorption for 10 K with three layers and with four layers show that our results are not converged with respect to the number of rhodium layers. This matter requires further investigation before final conclusions on the free energy differences of desorption can be made.

# Chapter 6

# Summary

We have investigated static and dynamic aspects of the interaction of rhodium surfaces with simple adsorbates using various computational approaches. The simulations were performed on the basis of density functional theory calculations with the PBE functional.

In the first example, we have used simulated annealing approaches in order to determine the complex structure of a NiO surface oxide formed on Rh(111). The stoichiometry of this structure was found to be $Ni_5O_5$. STM simulations performed in the Tersoff-Hamann approximation showed good agreement with experimental STM images. Further verification for the $Ni_5O_5$ phase was obtained by the calculation of the infrared intensities of the vibrational eigenmodes via Born effective charges. The resulting vibrational spectrum is in very good agreement with the experimental phonon loss structure. The thermodynamic stability of the $Ni_5O_5$ structure was evaluated by calculating the Gibbs free energies of several competing phases. The phase diagram confirms the pronounced stability of the $Ni_5O_5$ surface oxide in a wide temperature and pressure range.

In the following part of the present thesis, we investigated the oxidation of carbon monoxide and the subsequent desorption of carbon dioxide on rhodium surfaces, namely on Rh(111), Rh(553), and $NiO_2$/Rh(553). The latter exhibits quasi-one-dimensional nickel oxide nanowires (of formal $NiO_2$ stoichiometry) grown at the step edges of the Rh(553) surface. We have applied the nudged elastic band method, the dimer method, and quasi-Newton algorithms to identify multiple reaction paths and energy barriers. Transition states were carefully tested by the calculation of vibrational modes and subsequent structure relaxation along minimum energy paths. Reaction rate constants were computed in the framework of transition state theory. In agreement with the experimental observation of a strongly reduced offset temperature for the reactions, the calculations predict a significantly enhanced catalytic activity of the nickel oxide stripes for CO oxidation and subsequent $CO_2$ desorption. Furthermore it was shown that if, in a reaction sequence of oxidation and desorption processes, the desorption barrier is rate determining, the prefactor can be of the order of $10^{15}\,\mathrm{s}^{-1}$, in contrast to the value of $10^{13}\,\mathrm{s}^{-1}$ that is frequently used in literature.

In the subsequent example, we applied a kinetic Monte Carlo algorithm in order to simulate temperature programed desorption spectra of O/Rh(111). A multi-site model allowing for adsorption of atomic oxygen in fcc-hollow sites and in hcp-hollow sites was used, where the energy of the system was described by a lattice gas Hamiltonian. To determine the optimal set of effective interaction parameters in this Hamiltonian, we applied the procedure of cross validation, where the inclusion of unoccupied sites allowed to efficiently reduce the error in the predicted energy of the experimentally observed high-coverage $(2\sqrt{3} \times 2\sqrt{3})R30^\circ$ structure. In order to calculate TPD spectra, desorption events were simulated in the framework of kinetic Monte Carlo, whereas diffusion events following each desorption event were simulated using the Metropolis algorithm.

In the last part of this thesis, we calculated free energy differences for diffusion and desorption events of oxygen on Rh(111) at 10 K, 350 K, 700 K, and 1400 K. We applied the method of thermodynamic integration of free energy gradients, where the reaction coordinate was described with one geometric parameter for the diffusion event, and with two geometric parameters for the desorption event. In the latter case, for fixed values of these parameters we have introduced the approximation of equal entropies of the subdomains of configuration space, which allowed us to compute a free energy gradient from separate constrained MD simulations in different subdomains. The numerical accuracy of the free energy differences of desorption was improved by applying free energy perturbation. For both the diffusion event and the desorption event we have compared the free energy differences obtained from thermodynamic integration with free energy differences obtained from a harmonic approximation. The agreement between the two approaches is satisfactory for the diffusion event, but only acceptable at low temperatures for the desorption event.

# Appendix A

# Proofs of Density Functional Theory

## A.1 Hohenberg-Kohn Theorem

In order to proof the Hohenberg-Kohn theorem, first of all it must be shown that the external potential $V_{\text{ext}}(\mathbf{r})$ is uniquely determined by a given many-electron wave function $\psi$.
With the Hamiltonian $H$ we write for the ground state

$$H\,\psi \,=\, E\,\psi\,. \tag{A.1}$$

Defining $H' := H - V_{\text{ext}}(\mathbf{r})$ this becomes

$$\begin{aligned} H\,\psi &= H'\,\psi + V_{\text{ext}}(\mathbf{r})\,\psi \quad = \quad E\,\psi \\ V_{\text{ext}}(\mathbf{r})\,\psi &= E\,\psi \,-\, H'\,\psi \\ V_{\text{ext}}(\mathbf{r}) &= E \,-\, \frac{H'\,\psi}{\psi}\,. \end{aligned} \tag{A.2}$$

Hence the external potential is, except for a constant $E$, uniquely determined by $\psi$ and $H'$. For two wave functions $\psi_1$ and $\psi_2$ satisfying

$$\begin{aligned} H_1\,\psi_1 &= E_1\,\psi_1 \quad \text{and} \\ H_2\,\psi_2 &= E_2\,\psi_2\,, \end{aligned}$$

where

$$\begin{aligned} H_1 &= H' + V_{\text{ext},\,1}(\mathbf{r}) \quad \text{and} \\ H_2 &= H' + V_{\text{ext},\,2}(\mathbf{r})\,, \end{aligned}$$

(A.2) implies

$$V_{\text{ext},\,1}(\mathbf{r}) \,\neq\, V_{\text{ext},\,2}(\mathbf{r}) \quad \Rightarrow \quad \psi_1 \,\neq\, \psi_2. \tag{A.3}$$

What follows is a proof by contradiction for the Hohenberg-Kohn theorem. Let $\psi_1$ be the ground state of the Hamiltonian $H_1$ satisfying $H_1\,\psi_1 = (H' + V_{\text{ext},1}(\mathbf{r}))\,\psi_1 = E_1\,\psi_1$. The assumption of the proof is that there exists an external potential $V_{\text{ext},2}(\mathbf{r}) \neq V_{\text{ext},1}(\mathbf{r})$ generating the same electron density $n(\mathbf{r})$.

Let $\psi_2$ be the ground state that is related to the potential $V_{\text{ext},2}(\mathbf{r})$ via $H_2\,\psi_2 = (H' + V_{\text{ext},2}(\mathbf{r}))\,\psi_2 = E_2\,\psi_2$. For the present proof to work we have to restrict our considerations to non degenerate energies $E_1$ and $E_2$. For $E_1$ we have

$$\begin{aligned} E_1 &= \langle\psi_1|H_1|\psi_1\rangle \\ &= \langle\psi_1|H' + V_{\text{ext},1}(\mathbf{r})|\psi_1\rangle \\ &= \langle\psi_1|H'|\psi_1\rangle + \langle\psi_1|V_{\text{ext},1}(\mathbf{r})|\psi_1\rangle \\ &= \langle\psi_1|H'|\psi_1\rangle + \int V_{\text{ext},1}(\mathbf{r})\; n(\mathbf{r})\; \mathrm{d}\mathbf{r}. \end{aligned} \tag{A.4}$$

Analogously we find

$$E_2 = \langle\psi_2|H'|\psi_2\rangle + \int V_{\text{ext},2}(\mathbf{r})\; n(\mathbf{r})\; \mathrm{d}\mathbf{r}\,. \tag{A.5}$$

Here the assumption of the proof was used that both potentials $V_{\text{ext},1}(\mathbf{r})$ and $V_{\text{ext},2}(\mathbf{r})$ generate the same electron density $n(\mathbf{r})$. From (A.3) and the requirement that $E_1$ is non degenerate it follows that

$$\begin{aligned} E_1 &< \langle\psi_2|H_1|\psi_2\rangle \\ &= \langle\psi_2|H_2|\psi_2\rangle + \langle\psi_2|(H_1 - H_2)|\psi_2\rangle \\ &= E_2 + \int (V_{\text{ext},1}(\mathbf{r}) - V_{\text{ext},2}(\mathbf{r}))\; n(\mathbf{r})\; \mathrm{d}\mathbf{r}. \end{aligned} \tag{A.6}$$

Analogously we obtain

$$E_2 < E_1 + \int (V_{\text{ext},2}(\mathbf{r}) - V_{\text{ext},1}(\mathbf{r}))\; n(\mathbf{r})\; \mathrm{d}\mathbf{r}. \tag{A.7}$$

Addition of the inequalities (A.6) and (A.7) yields the contradiction

$$E_1 + E_2 < E_1 + E_2.$$

Consequently there can be no different external potentials which in the ground state generate the same electron density $n(\mathbf{r})$.

## A.2 Derivation of the Kohn-Sham Equations

The energy $E$ of a system with Hamiltonian $H$ is calculated from the normalized wave function $\psi$ as

$$E = \langle\psi|H|\psi\rangle. \tag{A.8}$$

First we show that minimization of $\langle\psi|H|\psi\rangle$ with respect to $\langle\psi|$ with the constraint $\langle\psi|\psi\rangle = 1$ yields the correct Schrödinger equation. Let $L := \langle\psi|H|\psi\rangle - \lambda\left(\langle\psi|\psi\rangle - 1\right)$ with the Lagrange multiplier $\lambda$. Since we want to minimize with respect to $\langle\psi|$, the variation of $L$ with respect to $\langle\psi|$ has to vanish:

$$\frac{\delta L}{\delta\langle\psi|} = H|\psi\rangle - \lambda\,|\psi\rangle \overset{!}{=} 0$$

$$\Rightarrow H|\psi\rangle = \lambda\,|\psi\rangle. \tag{A.9}$$

The minimization thus gives the Schrödinger equation. Minimization with respect to $|\psi\rangle$ yields the same result, although in adjoint form:

$$\frac{\delta L}{\delta|\psi\rangle} = \langle\psi|H - \langle\psi|\lambda \overset{!}{=} 0$$

$$\Rightarrow \langle\psi|H = \langle\psi|\lambda. \tag{A.10}$$

Due to $H^\dagger = H$ the adjoint form of (A.10) is the Schrödinger equation (A.9). In the following this method is used in order to derive the Kohn-Sham equations from the Kohn-Sham energy functional.

For the ground state energy of an interacting inhomogeneous electron gas in an external potential $V_{\text{ext}}(\mathbf{r})$, Hohenberg and Kohn have suggested the functional [3]

$$E[n] = \int V_{\text{ext}}(\mathbf{r})\, n(\mathbf{r})\, \mathrm{d}\mathbf{r} + \frac{1}{2}\int\int \frac{n(\mathbf{r})\, n(\mathbf{r}')}{|\mathbf{r}-\mathbf{r}'|}\, \mathrm{d}\mathbf{r}\, \mathrm{d}\mathbf{r}' + G[n]. \tag{A.11}$$

Here, $n(\mathbf{r})$ is the electron density and $G[n]$ is a universal functional in the sense that it is independent of the number of electrons and independent of the external potential. For $G[n]$ Kohn and Sham have presented the form [4]

$$G[n] = T_s[n] + E_{xc}[n]\,, \tag{A.12}$$

where $T_s[n]$ is the kinetic energy of a system of non interacting electrons with density $n(\mathbf{r})$. The electrons are described by one-electron wave functions $\{\phi_i\}$. For non interacting particles the total kinetic energy is simply the sum of the individual kinetic energies:

$$T_s[n] = T_s[\{\phi_i[n]\}] = -\sum_i \int \phi_i^*(\mathbf{r})\ \frac{1}{2}\Delta\ \phi_i(\mathbf{r})\ \mathrm{d}\mathbf{r}. \tag{A.13}$$

The notation $T_s[\{\phi_i[n]\}]$ indicates that $T_s$ is a functional of the one-electron wave functions $\{\phi_i\}$ which themselves are functionals of the electron density $n(\mathbf{r})$. The sum is taken over all occupied states. $E_{xc}[n]$ in (A.12) is the exchange-correlation energy of a system of interacting electrons with density $n(\mathbf{r})$. The energy functional thus becomes

$$\begin{aligned} E[\{\phi_i\}] &= -\sum_i \int \phi_i^*(\mathbf{r})\ \frac{1}{2}\Delta\ \phi_i(\mathbf{r})\ \mathrm{d}\mathbf{r} + \int V_{\text{ext}}(\mathbf{r})\, n(\mathbf{r})\, \mathrm{d}\mathbf{r} \\ &\quad + \frac{1}{2}\int\int \frac{n(\mathbf{r})\, n(\mathbf{r}')}{|\mathbf{r}-\mathbf{r}'|}\, \mathrm{d}\mathbf{r}\, \mathrm{d}\mathbf{r}' + E_{xc}[n]\,. \end{aligned} \tag{A.14}$$

This form of the energy functional is minimized with respect to the $N$ one-electron wave functions $\phi_i^*$ with the constraints $\langle\phi_i|\phi_i\rangle = 1$ with Lagrange multipliers $\varepsilon_i$, i.e. for $j = 1, \ldots, N$ let

$$\frac{\delta\{E - \sum_i \varepsilon_i\,(\langle\phi_i|\phi_i\rangle - 1)\}}{\delta\langle\phi_j|} = 0. \tag{A.15}$$

For the separate terms in (A.14) we have

$$\frac{\delta}{\delta\,\phi_j^*(\mathbf{r})}\left\{-\sum_i \int \phi_i^*(\mathbf{r})\ \frac{1}{2}\Delta\ \phi_i(\mathbf{r})\ \mathrm{d}\mathbf{r}\right\} = -\frac{1}{2}\Delta\,\phi_j(\mathbf{r}),$$

$$\frac{\delta}{\delta\,\phi_j^*(\mathbf{r})}\left\{\int V_{\text{ext}}(\mathbf{r})\, n(\mathbf{r})\, \mathrm{d}\mathbf{r}\right\} = V_{\text{ext}}(\mathbf{r})\,\phi_j(\mathbf{r}),$$

$$\begin{aligned} &\frac{\delta}{\delta\,\phi_j^*(\mathbf{r})}\left\{\frac{1}{2}\int\int \frac{n(\mathbf{r})\, n(\mathbf{r}')}{|\mathbf{r}-\mathbf{r}'|}\, \mathrm{d}\mathbf{r}\, \mathrm{d}\mathbf{r}'\right\} \\ &= \frac{\delta}{\delta\, n(\mathbf{r})}\left\{\frac{1}{2}\int\int \frac{n(\mathbf{r}'')\, n(\mathbf{r}')}{|\mathbf{r}''-\mathbf{r}'|}\, \mathrm{d}\mathbf{r}''\, \mathrm{d}\mathbf{r}'\right\} \frac{\delta\, n(\mathbf{r})}{\delta\,\phi_j^*(\mathbf{r})} \\ &= \left\{\int \frac{n(\mathbf{r}')}{|\mathbf{r}-\mathbf{r}'|}\, \mathrm{d}\mathbf{r}'\right\}\ \phi_j(\mathbf{r}), \end{aligned}$$

$$\frac{\delta}{\delta\,\phi_j^*(\mathbf{r})}\, E_{xc}[n] \ = \ \frac{\delta}{\delta\, n(\mathbf{r})}\, E_{xc}[n]\ \frac{\delta\, n(\mathbf{r})}{\delta\,\phi_j^*(\mathbf{r})} \ =:\ V_{xc}(\mathbf{r})\ \phi_j(\mathbf{r}).$$

Hence (A.15) yields, with the variation of the constraints

$$\frac{\delta}{\delta\langle\phi_j|}\left\{-\sum_i \varepsilon_i\,(\langle\phi_i|\phi_i\rangle - 1)\right\} \ = \ -\varepsilon_j\,|\phi_j\rangle,$$

the Kohn-Sham equations

$$\left\{-\frac{1}{2}\Delta + V_{\text{ext}}(\mathbf{r}) + \int \frac{n(\mathbf{r}')}{|\mathbf{r}-\mathbf{r}'|}\, \mathrm{d}\mathbf{r}' + V_{xc}(\mathbf{r})\right\}\ \phi_j(\mathbf{r}) \ = \ \varepsilon_j\,\phi_j(\mathbf{r}).$$

## A.3 Total Energy in DFT

We want to show that the sum of the Kohn-Sham eigenvalues is not equal to the total energy of the many-electron system. The total energy of a system with electron density

$$n(\mathbf{r}) = \sum_i \phi_i^*(\mathbf{r})\, \phi_i(\mathbf{r})\,,$$

where $\{\phi_i\}$ are the solutions of the Kohn-Sham equations, and ions at coordinates $\{R_I\}$ is given by the Kohn-Sham energy functional

$$E[\{\phi_i\}] \;=\; T[\{\phi_i\}]+E_{\text{ext}}[n(\mathbf{r})]+E_H[n(\mathbf{r})]+E_{xc}[n(\mathbf{r})]+E_{\text{ion}}(\{R_I\})\,, \tag{A.16}$$

with

$$\begin{aligned} T[\{\phi_i\}] &= -\sum_i \int \phi_i^*(\mathbf{r})\; \frac{1}{2}\Delta\; \phi_i(\mathbf{r})\; \mathrm{d}\mathbf{r}, && \text{(A.17)}\\ E_{\text{ext}}[n(\mathbf{r})] &= \int V_{\text{ext}}(\mathbf{r})\; n(\mathbf{r})\; \mathrm{d}\mathbf{r}, && \text{(A.18)}\\ E_H[n(\mathbf{r})] &= \frac{1}{2}\int\int \frac{n(\mathbf{r})\, n(\mathbf{r}')}{|\mathbf{r}-\mathbf{r}'|}\; \mathrm{d}\mathbf{r}\; \mathrm{d}\mathbf{r}', && \text{(A.19)}\\ E_{xc}[n(\mathbf{r})] &= \int \varepsilon_{xc}(n(\mathbf{r}))\; n(\mathbf{r})\; \mathrm{d}\mathbf{r}. && \text{(A.20)} \end{aligned}$$

Below we will compare the sum of the Kohn-Sham eigenvalues with (A.16)-(A.20).
The Kohn-Sham equations are

$$\left\{-\frac{1}{2}\Delta + V_{\text{ext}}(\mathbf{r}) + V_H(\mathbf{r}) + V_{xc}(\mathbf{r})\right\}\, \phi_i(\mathbf{r}) = \varepsilon_i\, \phi_i(\mathbf{r}), \tag{A.21}$$

or, in Dirac notation,

$$H\,|\phi_i\rangle \;=\; \varepsilon_i\,|\phi_i\rangle, \qquad i = 1, \ldots, N, \tag{A.22}$$

where $H$ is the Hamiltonian and $N$ is the number of electrons. Because of $\langle\phi_i|\phi_j\rangle = \delta_{ij}$ we have

$$\varepsilon_i \;=\; \langle\phi_i|\, H\,|\phi_i\rangle, \tag{A.23}$$

respectively

$$\varepsilon_i \;=\; \int \phi_i^*(\mathbf{r})\, \left\{-\frac{1}{2}\Delta + V_{\text{ext}}(\mathbf{r}) + V_H(\mathbf{r}) + V_{xc}(\mathbf{r})\right\}\, \phi_i(\mathbf{r})\; \mathrm{d}\mathbf{r}. \tag{A.24}$$

The sum of the Kohn-Sham eigenvalues is therefore

$$\begin{aligned}\sum_{i=1}^{N} \varepsilon_i &= -\sum_i \int \phi_i^*(\mathbf{r})\ \frac{1}{2}\Delta\ \phi_i(\mathbf{r})\ \mathrm{d}\mathbf{r} \\ &\quad +\sum_i \int \phi_i^*(\mathbf{r})\ V_{\mathrm{ext}}(\mathbf{r})\ \phi_i(\mathbf{r})\ \mathrm{d}\mathbf{r} \\ &\quad +\sum_i \int \phi_i^*(\mathbf{r})\ V_H(\mathbf{r})\ \phi_i(\mathbf{r})\ \mathrm{d}\mathbf{r} \\ &\quad +\sum_i \int \phi_i^*(\mathbf{r})\ V_{xc}(\mathbf{r})\ \phi_i(\mathbf{r})\ \mathrm{d}\mathbf{r}. \end{aligned} \tag{A.25}$$

The first term on the right hand side is the kinetic energy of the electrons and is equal to (A.17). The second term is

$$\begin{aligned} &\sum_i \int \phi_i^*(\mathbf{r})\ V_{\mathrm{ext}}(\mathbf{r})\ \phi_i(\mathbf{r})\ \mathrm{d}\mathbf{r} \\ &= \int V_{\mathrm{ext}}(\mathbf{r})\ \sum_i \phi_i^*(\mathbf{r})\ \phi_i(\mathbf{r})\ \mathrm{d}\mathbf{r} \\ &= \int V_{\mathrm{ext}}(\mathbf{r})\ n(\mathbf{r})\ \mathrm{d}\mathbf{r}, \end{aligned} \tag{A.26}$$

in agreement with (A.18). With the Hartree potential

$$V_H(\mathbf{r}) = \int \frac{n(\mathbf{r}')}{|\mathbf{r}-\mathbf{r}'|}\ \mathrm{d}\mathbf{r}', \tag{A.27}$$

we get for the third term in (A.25)

$$\begin{aligned} &\sum_i \int \phi_i^*(\mathbf{r})\ V_H(\mathbf{r})\ \phi_i(\mathbf{r})\ \mathrm{d}\mathbf{r} \\ &= \int V_H(\mathbf{r})\ \sum_i \phi_i^*(\mathbf{r})\ \phi_i(\mathbf{r})\ \mathrm{d}\mathbf{r} \\ &= \int V_H(\mathbf{r})\ n(\mathbf{r})\ \mathrm{d}\mathbf{r} \\ &= \int\int \frac{n(\mathbf{r})\, n(\mathbf{r}')}{|\mathbf{r}-\mathbf{r}'|}\ \mathrm{d}\mathbf{r}\ \mathrm{d}\mathbf{r}'. \end{aligned} \tag{A.28}$$

A comparison with (A.19) shows that (A.28) is too large by a factor of 2. Consequently half of (A.28) has to be subtracted from the sum of the Kohn-Sham eigenvalues in order to obtain the total energy of the system. For the fourth term in (A.25) we obtain

$$\begin{aligned} &\sum_i \int \phi_i^*(\mathbf{r})\ V_{xc}(\mathbf{r})\ \phi_i(\mathbf{r})\ \mathrm{d}\mathbf{r} \\ &= \int V_{xc}(\mathbf{r})\ n(\mathbf{r})\ \mathrm{d}\mathbf{r}, \end{aligned} \tag{A.29}$$

which is not in agreement with (A.20). Hence (A.29) has to be subtracted from the sum of the Kohn-Sham eigenvalues and (A.20) has to be added. In summary the total energy can be calculated as

$$\begin{aligned} E_{\mathrm{DFT}} &= \sum_{i=1}^{N} \varepsilon_i - \frac{1}{2} \int\!\!\int \frac{n(\mathbf{r})\, n(\mathbf{r}')}{|\mathbf{r}-\mathbf{r}'|}\, \mathrm{d}\mathbf{r}\, \mathrm{d}\mathbf{r}' \\ &\quad - \int V_{xc}(\mathbf{r})\; n(\mathbf{r})\; \mathrm{d}\mathbf{r} + \int \varepsilon_{xc}(n(\mathbf{r}))\; n(\mathbf{r})\; \mathrm{d}\mathbf{r}. \end{aligned}$$

## A.4 Hellmann-Feynman Theorem

Let $E = E[\{\phi_i\}, \{\mathbf{R}_k\}]$ be the total energy of a system composed of ions and electrons. This functional depends on the Kohn-Sham wave functions $\{\phi_i\}$ and the coordinates $\{\mathbf{R}_k\}$ of the ions. The force $\mathbf{F}_I$ acting on ion $I$ is

$$\mathbf{F}_I = -\frac{\mathrm{d}E}{\mathrm{d}\mathbf{R}_I}, \tag{A.30}$$

which is the total derivative of the energy with respect to the coordinates of ion $I$. In full form this derivative is

$$-\frac{\mathrm{d}E}{\mathrm{d}\mathbf{R}_I} = -\frac{\partial E}{\partial \mathbf{R}_I} - \sum_i \frac{\delta E}{\delta|\phi_i\rangle} \frac{\mathrm{d}|\phi_i\rangle}{\mathrm{d}\mathbf{R}_I} - \sum_i \frac{\delta E}{\delta\langle\phi_i|} \frac{\mathrm{d}\langle\phi_i|}{\mathrm{d}\mathbf{R}_I}. \tag{A.31}$$

For the derivatives of the energy with respect to the orbitals we have (see section A.2)

$$\frac{\delta E}{\delta\langle\phi_i|} = H\,|\phi_i\rangle = |H\phi_i\rangle \quad \text{and} \quad \frac{\delta E}{\delta|\phi_i\rangle} = \langle\phi_i|\,H = \langle\phi_i\,H|\,. \tag{A.32}$$

Using the notation

$$\frac{\mathrm{d}|\phi_i\rangle}{\mathrm{d}\mathbf{R}_I} = \left|\frac{\mathrm{d}\phi_i}{\mathrm{d}\mathbf{R}_I}\right\rangle \quad \text{and} \quad \frac{\mathrm{d}\langle\phi_i|}{\mathrm{d}\mathbf{R}_I} = \left\langle\frac{\mathrm{d}\phi_i}{\mathrm{d}\mathbf{R}_I}\right| \tag{A.33}$$

we can write

$$\mathbf{F}_I = -\frac{\partial E}{\partial \mathbf{R}_I} - \sum_i \left( \left\langle \phi_i\, H \middle| \frac{\mathrm{d}\phi_i}{\mathrm{d}\mathbf{R}_I} \right\rangle + \left\langle \frac{\mathrm{d}\phi_i}{\mathrm{d}\mathbf{R}_I} \middle| H\phi_i \right\rangle \right). \tag{A.34}$$

If the wave functions are eigenstates of the Hamiltonian, this is

$$\begin{aligned} \mathbf{F}_I &= -\frac{\partial E}{\partial \mathbf{R}_I} - \sum_i \varepsilon_i \left( \left\langle \phi_i \middle| \frac{\mathrm{d}\phi_i}{\mathrm{d}\mathbf{R}_I} \right\rangle + \left\langle \frac{\mathrm{d}\phi_i}{\mathrm{d}\mathbf{R}_I} \middle| \phi_i \right\rangle \right) \\ &= -\frac{\partial E}{\partial \mathbf{R}_I} - \sum_i \varepsilon_i \frac{\mathrm{d}}{\mathrm{d}\mathbf{R}_I} \langle\phi_i|\phi_i\rangle. \end{aligned} \tag{A.35}$$

Since $\langle \phi_i | \phi_i \rangle$ is constant, we get

$$\forall i : \quad \frac{\mathrm{d}}{\mathrm{d}\mathbf{R}_I} \langle \phi_i | \phi_i \rangle \;=\; 0. \tag{A.36}$$

Consequently only the partial derivative of the total energy with respect to the coordinates of ion $I$ remains as the force acting on the ion:

$$\mathbf{F}_I \;=\; -\frac{\partial E}{\partial \mathbf{R}_I}. \tag{A.37}$$

This result is the Hellmann-Feynman theorem.

# Appendix B

# Cross Validation: Input and Output

## B.1 Input Configurations

In the following we show the input configurations calculated with DFT for the cross validation scheme in Chapter 4. The structures are ordered according to the size of the surface cell that was used for the DFT calculation. The unit vectors with respect to which the surface cells are specified are depicted in the first picture. Red balls indicate oxygen atoms in fcc-hollow sites, yellow balls in hcp-hollow sites.

### B.1.1 $(1 \times 1)$ Surface Cells

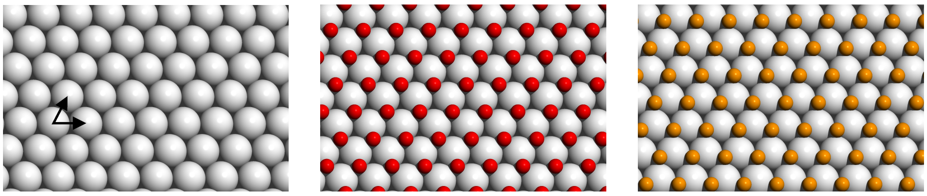

### B.1.2 $(2 \times 2)$ Surface Cells

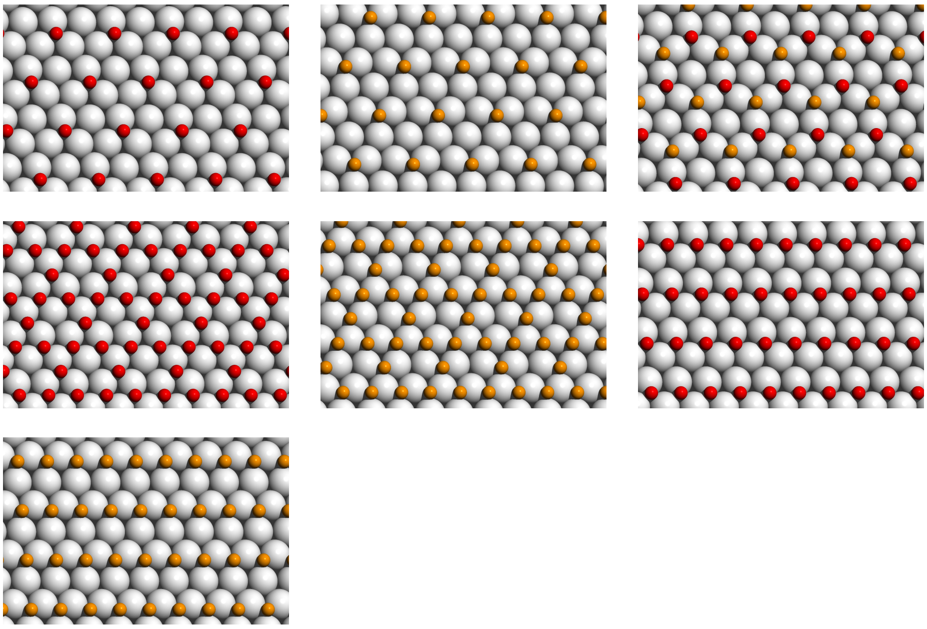

### B.1.3 $(3 \times 3)$ Surface Cells

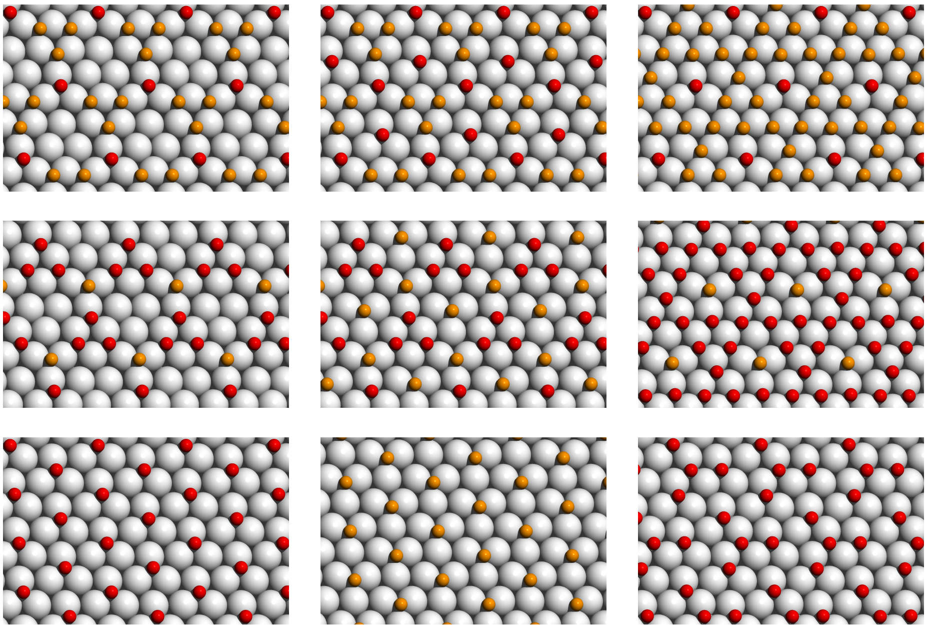

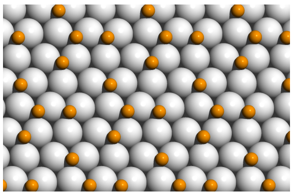
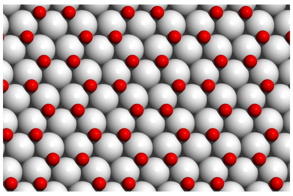
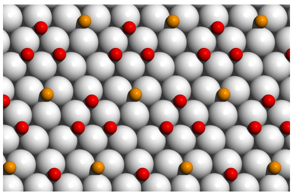
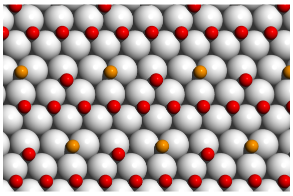
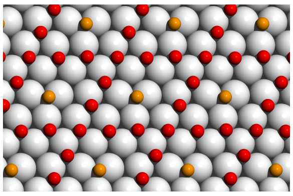
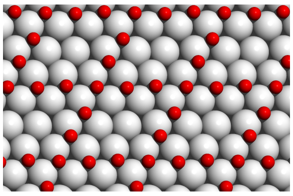
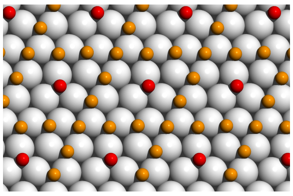
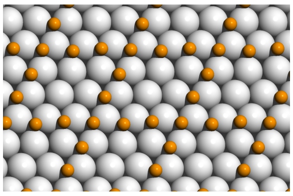
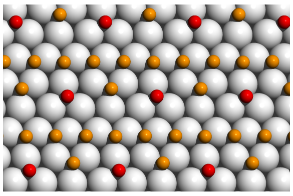
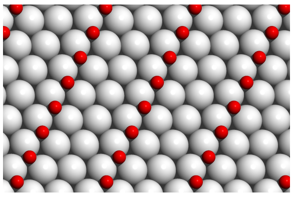
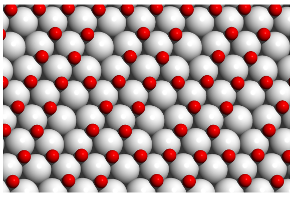

### B.1.4 (4 × 4) Surface Cells

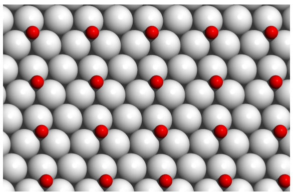
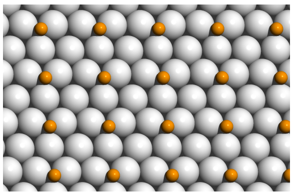
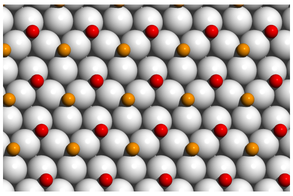
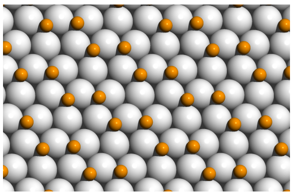
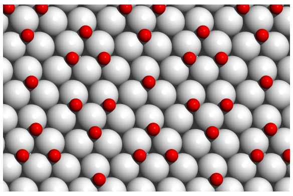
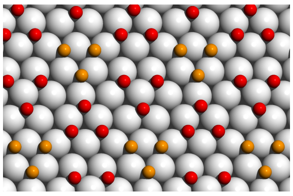

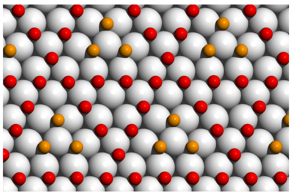
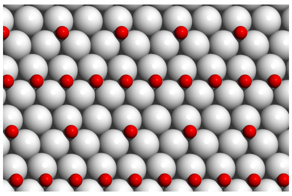
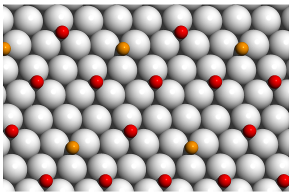
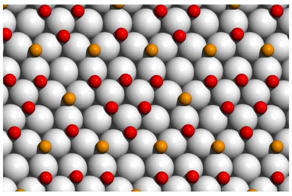
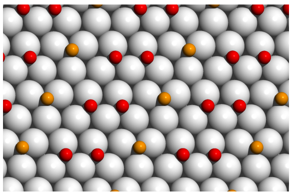
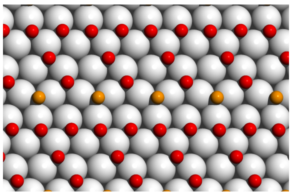
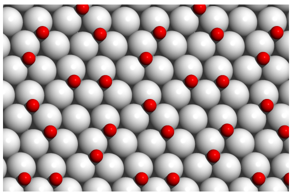

### B.1.5 $(6 \times 6)$ Surface Cells

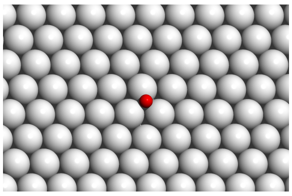
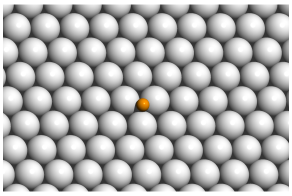
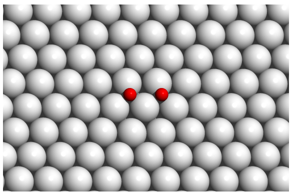
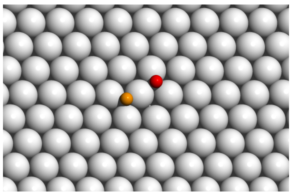
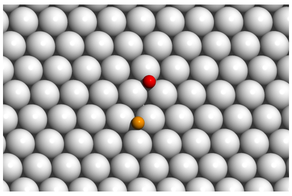
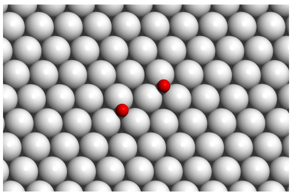
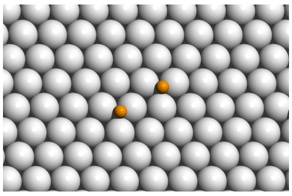
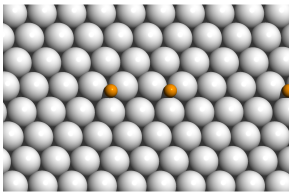
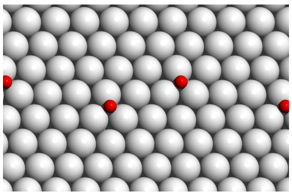

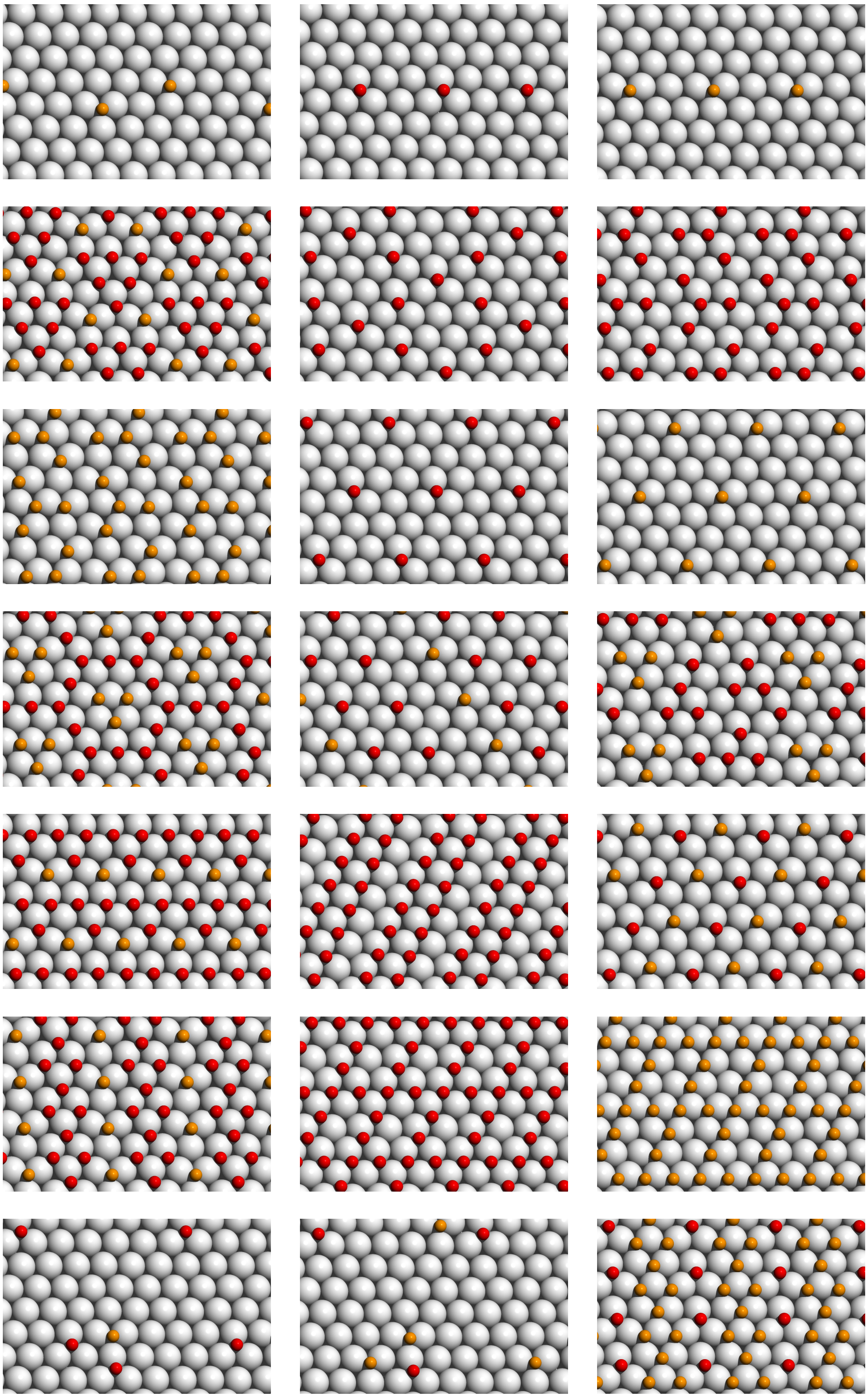

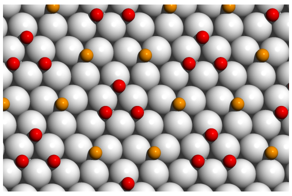
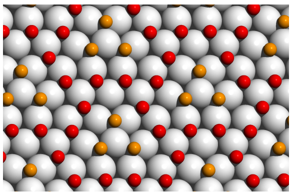
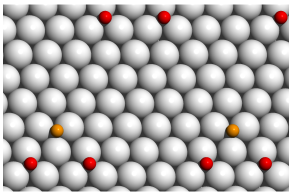
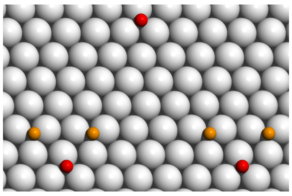
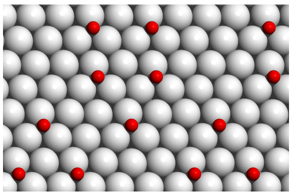
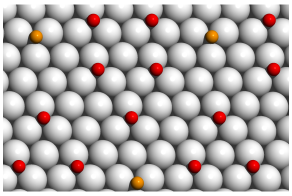
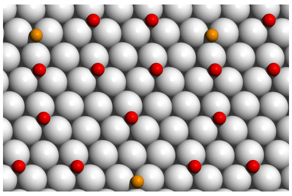
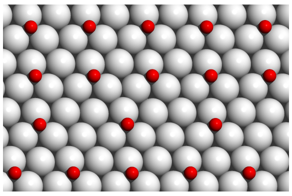
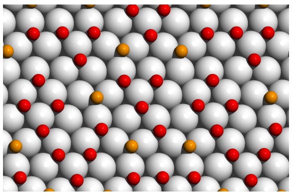
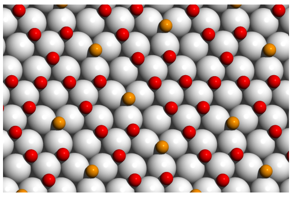
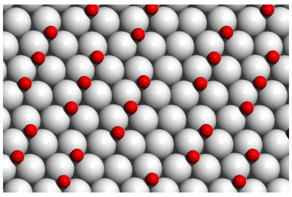
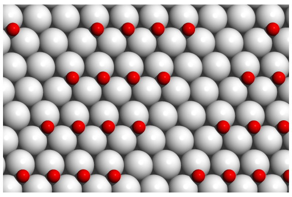
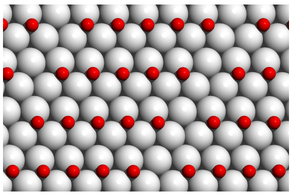
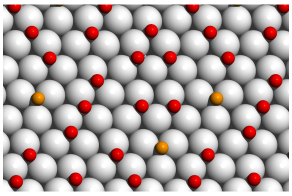

### B.1.6 $(8 \times 8)$ Surface Cells

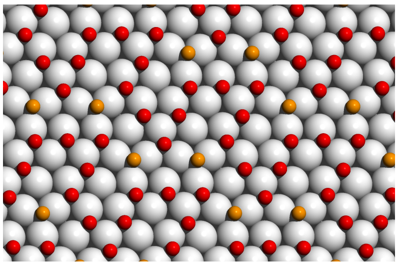

## B.2 Output: Effective Interaction Parameters

Here we give an overview of the set of figures and the corresponding effective interaction parameters for which the lowest cross validation score was found (parametrization (a) of Table 4.2). The insets in the pictures give the values of the effective interaction parameters (in meV) as obtained by the cross validation scheme.

### B.2.1 Two-body Figures

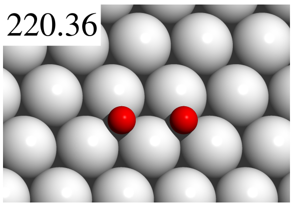

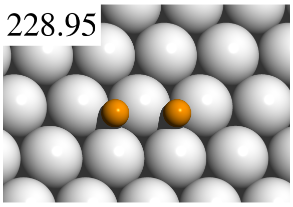

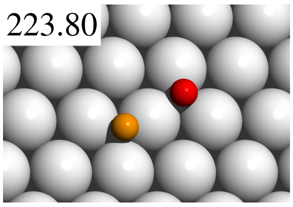

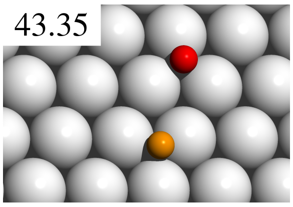

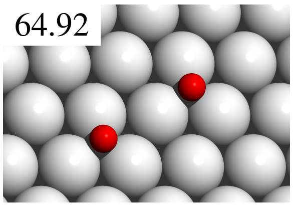

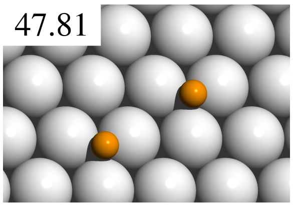

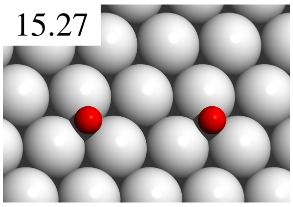

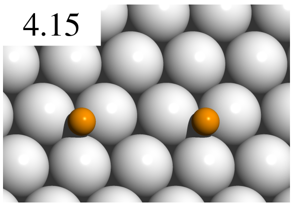

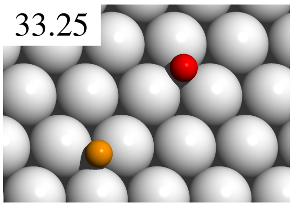

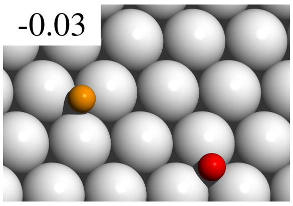

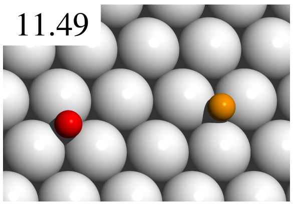

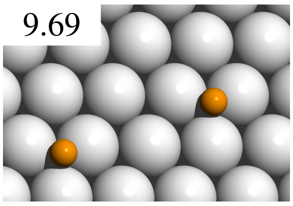

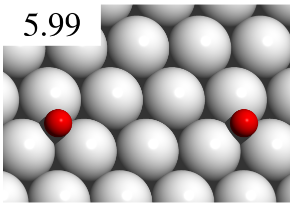

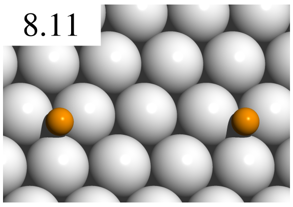

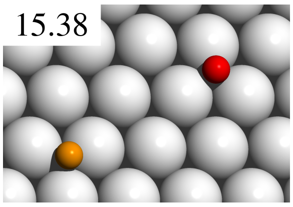

### B.2.2 Three-body Figures

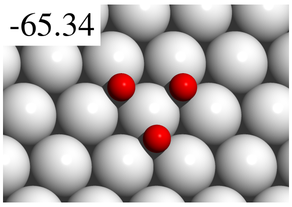
-65.34

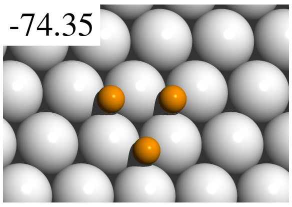
-74.35

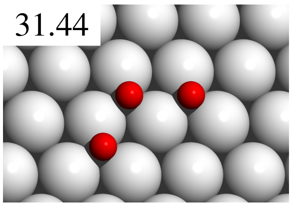
31.44

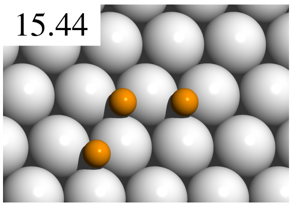
15.44

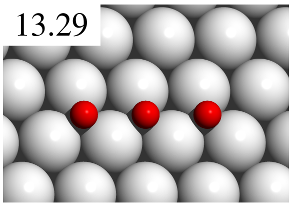
13.29

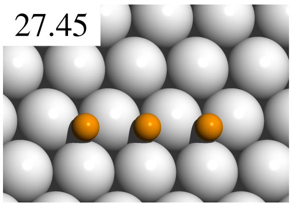
27.45

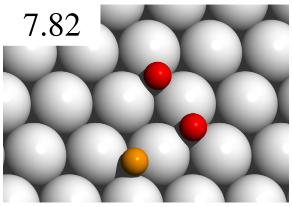
7.82

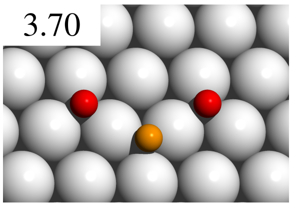
3.70

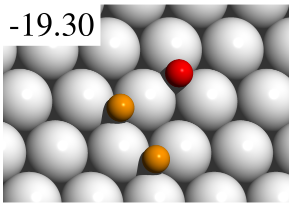
-19.30

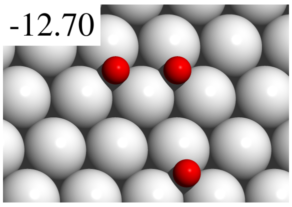
-12.70

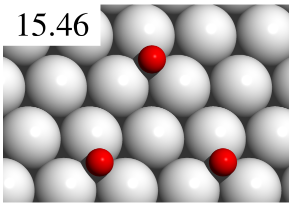
15.46

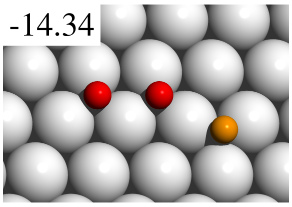
-14.34

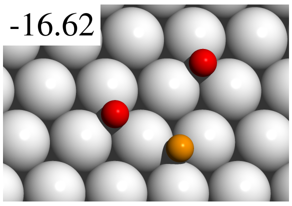
-16.62

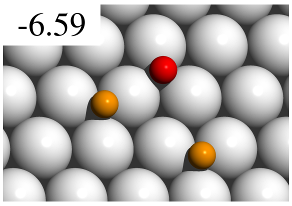
-6.59

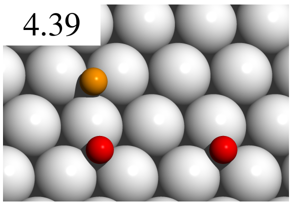
4.39

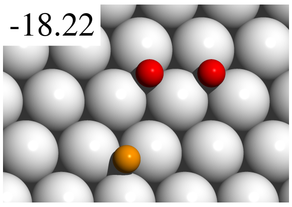
-18.22

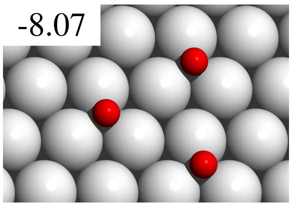
-8.07

### B.2.3 Four-body Figures

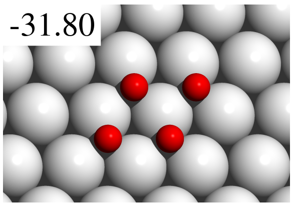

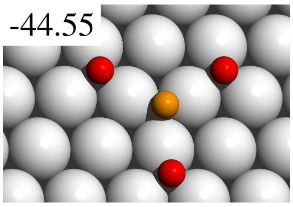

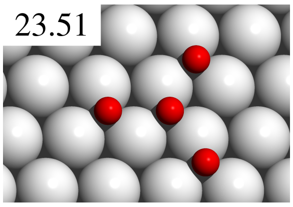

### B.2.4 Figures including Unoccupied Sites

Balls in black indicate that the corresponding adsorption sites are unoccupied.

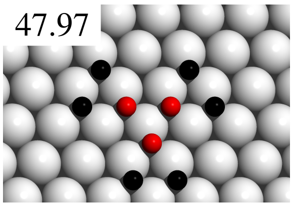

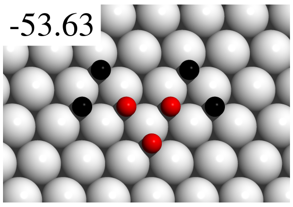

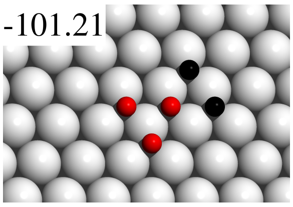

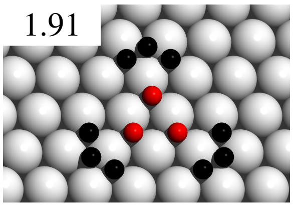

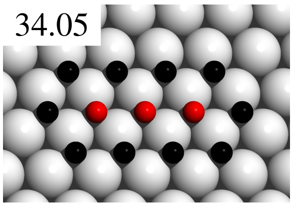

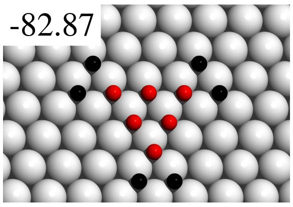

# Bibliography

[1] G. Kresse, J. Furthmüller, *Efficient iterative schemes for ab initio total-energy calculations using a plane-wave basis set*, Phys. Rev. B 54, 11169 (1996)

[2] G. Kresse, J. Furthmüller, *Efficiency of ab-initio total energy calculations for metals and semiconductors using a plane-wave basis set*, Comput. Mater. Sci. 6, 15 (1996)

[3] P. Hohenberg, W. Kohn, *Inhomogeneous electron gas*, Phys. Rev. 136, B864 (1964)

[4] W. Kohn, L. J. Sham, *Self-consistent equations including exchange and correlation effects*, Phys. Rev. 140, A1133 (1965)

[5] M. C. Payne, M. P. Teter, D. C. Allan, T. A. Arias, J. D. Joannopoulos, *Iterative minimization techniques for ab initio total-energy calculations: molecular dynamics and conjugate gradients*, Rev. Mod. Phys. 64, 1045 (1992)

[6] M. J. Gillan, *The virtual matter laboratory*, Contemporary Physics 38, 115 (1997)

[7] Klaus Capelle, *A bird's-eye view of density-functional theory*, arXiv:cond-mat/0211443v5

[8] J. P. Perdew, K. Burke, M. Ernzerhof, *Generalized gradient approximation made simple*, Phys. Rev. Lett. 77, 3865 (1996)

[9] J. Goniakowski, F. Finocchi, C. Noguera, *Polarity of oxide surfaces and nanostructures*, Rep. Prog. Phys. 71, 016501 (2008)

[10] A. Barbier, C. Mocuta, H. Kuhlenbeck, K. F. Peters, B. Richter, G. Renaud, *Atomic structure of the polar NiO(111)-p(2×2) surface*, Phys. Rev. Lett. 84, 2897 (2000)

[11] A. Barbier, C. Mocuta, W. Neubeck, M. Mulazzi, F. Yakhou, K. Chesnei, A. Sollier, C. Vettier, F. de Bergevin, *Surface and bulk spin ordering*

*of antiferromagnetic materials: NiO(111)*, Phys. Rev. Lett. 93, 257208 (2004)

[12] J. Schoiswohl, F. Mittendorfer, S. Surnev, M. G. Ramsey, J. N. Andersen, F. P. Netzer, *Chemical reactivity of Ni-Rh nanowires*, Phys. Rev. Lett 97, 126102 (2006)

[13] S. Surnev, F. Allegretti, G. Parteder, T. Franz, F. Mittendorfer, J. N. Andersen, F. P. Netzer, *One-Dimensional Oxide-Metal Hybrid Structures: Site-Specific Enhanced Reactivity for CO Oxidation*, ChemPhysChem 11, 2506 (2010)

[14] G. Parteder, F. Allegretti, M. Wagner, M. G. Ramsey, S. Surnev, F. P. Netzer, *Growth and oxidation of Ni nanostructures on stepped Rh surfaces*, J. Phys. Chem. C 112, 19272 (2008)

[15] Ch. Hagendorf, R. Shantyr, H. Neddermeyer, W. Widdra, *Pressure dependent NiO phase transitions and Ni oxide formation on Pt(111): an in situ STM study at elevated temperatures*, Phys. Chem. Chem. Phys. 8, 1575 (2006)

[16] G. Kresse, W. Bergermayer, R. Podloucky, E. Lundgren, R. Koller, M. Schmid, P. Varga, *Complex surface reconstructions solved by ab initio molecular dynamics*, Appl. Phys. A 76, 701 (2003)

[17] J. Tersoff, D. R. Hamann, *Theory of the scanning tunneling microscope*, Phys. Rev. B 31, 805 (1985)

[18] L. Gragnaniello, G. Barcaro, L. Sementa, F. Allegretti, G. Parteder, S. Surnev, W. Steurer, A. Fortunelli, F. P. Netzer, *The two-dimensional cobalt oxide (9×2) phase on Pd(100)*, J. Chem. Phys 134, 184706 (2011)

[19] K. Reuter, M. Scheffler, *Composition, structure, and stability of* $RuO_2$*(110) as a function of oxygen pressure*, Phys. Rev. B 65, 035406 (2001)

[20] Peter Atkins, Julio de Paula, *Physical Chemistry*, ninth edition, Chapters 15 and 16; Oxford University Press, Oxford, 2010

[21] A. R. Kortan, R. L. Park, *Phase diagram of oxygen chemisorbed on Ni(111)*, Phys. Rev. B 23, 6340 (1981)

[22] F. Mittendorfer, *Low-dimensional surface oxides in the oxidation of Rh particles*, J. Phys.: Condens. Matter 22, 393001 (2010)

[23] J. Schoiswohl, F. Mittendorfer, S. Surnev, M. G. Ramsey, J. N. Andersen, F. P. Netzer, *Chemical reactivity of Ni-Rh Nanowires*, Phys. Rev. Lett. 97, 126102 (2006)

[24] G. Mills, H. Jónsson, *Quantum and thermal effects in $H_2$ dissociative adsorption: evaluation of free energy barriers in multidimensional quantum systems*, Phys. Rev. Lett. 72, 1124 (1994)

[25] G. Mills, H. Jónsson, G. K. Schenter, *Reversible work transition state theory: application to dissociative adsorption of hydrogen*, Surf. Sci. 324, 305 (1995)

[26] H. Jónsson, G. Mills, K. W. Jacobsen, *Nudged elastic band method for finding minimum energy paths of transitions*, in B. J. Berne, G. Ciccotti, D. F. Coker, *Classical and Quantum Dynamics in Condensed Phase Simulations*, Chapter 16; World Scientific, 1998

[27] G. Henkelman, B. P. Uberuaga, H. Jónsson, *A climbing image nudged elastic band method for finding saddle points and minimum energy paths*, J. Chem. Phys. 113, 9901 (2000)

[28] G. Henkelman, H. Jónsson, *Improved tangent estimate in the nudged elastic band method for finding minimum energy paths and saddle points*, J. Chem. Phys. 113, 9978 (2000)

[29] G. Henkelman, H. Jónsson, *A dimer method for finding saddle points on high dimensional potential surfaces using only first derivatives*, J. Chem. Phys. 111, 7010 (1999)

[30] A. Heyden, A. T. Bell, F. J. Keil, *Efficient methods for finding transition states in chemical reactions: Comparison of improved dimer method and partitioned rational function optimization method*, J. Chem. Phys. 123, 224101 (2005)

[31] William H. Press, Saul A. Teukolsky, William T. Vetterling, Brian P. Flannery, *Numerical Recipes in C*, 2nd edition, Chapters 9 and 10; Cambridge University Press, 2002

[32] P. Pulay, *Convergence acceleration of iterative sequences. The case of SCF iteration*, Chem. Phys. Lett. 73, 393 (1980)

[33] H. Eyring, *The Activated Complex in Chemical Reactions*, J. Chem. Phys. 3, 107 (1935)

[34] M. G. Evans, M. Polanyi, *Some applications of the transition state method to the calculation of reaction velocities, especially in solution*, Trans. Faraday Soc. 31, 875 (1935)

[35] R. A. van Santen, J. W. Niemantsverdriet, *Chemical Kinetics and Catalysis*, Chapter 4; Plenum Press, 1995

[36] G. H. Vineyard, *Frequency factors and isotope effects in solid state rate processes*, J. Phys. Chem. Solids 3, 121 (1957)

[37] P. Pechukas, *Statistical Approximations in Collision Theory*, in W. H. Miller, *Dynamics of Molecular Collisions*, Chapter 6; Plenum Press, 1976

[38] P. Hänggi, P. Talkner, M. Borkovec, *Reaction-rate theory: fifty years after Kramers*, Rev. Mod. Phys. 62, 251 (1990)

[39] L. H. Dubois, G. A. Somorjai, *The chemisorption of CO and $CO_2$ on Rh(111) studied by high resolution electron energy loss spectroscopy*, Surf. Sci. 91, 514 (1980)

[40] A. Beutler, E. Lundgren, R. Nyholm, J. N. Andersen, B. Setlik, D. Heskett, *On the adsorption sites for CO on the Rh(111) single crystal surface*, Surf. Sci. 371, 381 (1997)

[41] A. Beutler, E. Lundgren, R. Nyholm, J. N. Andersen, B. J. Setlik, D. Heskett, *Coverage- and temperature-dependent site occupancy of carbon monoxide on Rh(111) studied by high-resolution core-level photoemission*, Surf. Sci. 396, 117 (1998)

[42] P. J. Feibelman, B. Hammer, J. K. Nørskov, F. Wagner, M. Scheffler, R. Stumpf, R. Watwe, J. Dumesic, *The CO/Pt(111) Puzzle*, J. Phys. Chem. B 105, 4018 (2001)

[43] A. Stroppa, G. Kresse, *The shortcomings of semi-local and hybrid functionals: what we can learn from surface science studies*, New J. Phys. 10, 063020 (2008)

[44] L. Schimka, J. Harl, A. Stroppa, A. Grüneis, M. Marsman, F. Mittendorfer, G. Kresse, *Accurate surface and adsorption energies from many-body perturbation theory*, Nature Materials 9, 741 (2010)

[45] J. Gustafson, A. Resta, A. Mikkelsen, R. Westerström, J. N. Andersen, E. Lundgren, J. Weissenrieder, M. Schmid, P. Varga, N. Kasper, X. Torrelles, S. Ferrer, F. Mittendorfer, G. Kresse, *Oxygen-induced step bunching and faceting of Rh(553): Experiment and ab initio calculations*, Phys. Rev. B 74, 035401 (2006)

[46] K. A. Fichthorn, W. H. Weinberg, *Theoretical foundations of dynamical Monte Carlo simulations*, J. Chem. Phys. 95, 1090 (1991)

[47] A. F. Voter, *Introduction to the Kinetic Monte Carlo method*, in K. E. Sickafus, E. A. Kotomin, B. P. Uberuaga, *Radiation Effects in Solids*, Springer, 2007

[48] B. Meng, W. H. Weinberg, *Monte Carlo simulations of temperature programmed desorption spectra*, J. Chem. Phys. 100, 5280 (1994)

[49] B. Meng, W. H. Weinberg, *Non-equilibrium effects on thermal desorption spectra*, Surf. Sci. 374, 443 (1997)

[50] N. Metropolis, A. W. Rosenbluth, M. N. Rosenbluth, A. H. Teller, *Equation of state calculations by fast computing machines*, J. Chem. Phys. 21, 1087 (1953)

[51] S. Schwegmann, H. Over, V. De Renzi, G. Ertl, *The atomic geometry of the O and CO + O phases on Rh(111)*, Surf. Sci. 375, 91 (1997)

[52] M. V. Ganduglia-Pirovano, M. Scheffler, *Structural and electronic properties of chemisorbed oxygen on Rh(111)*, Phys. Rev. B 59, 15533 (1999)

[53] L. Köhler, G. Kresse, M. Schmid, E. Lundgren, J. Gustafson, A. Mikkelsen, M. Borg, J. Yuhara, J. N. Andersen, M. Marsman, P. Varga, *High-coverage oxygen structures on Rh(111): adsorbate repulsion and site preference is not enough*, Phys. Rev. Lett. 93, 266103 (2004)

[54] J. Gustafson, A. Mikkelsen, M. Borg, E. Lundgren, L. Köhler, G. Kresse, M. Schmid, P. Varga, J. Yuhara, X. Torrelles, C. Quirós, J. N. Andersen, *Self-limited growth of a thin oxide layer on Rh(111)*, Phys. Rev. Lett. 92, 126102 (2004)

[55] C. Stampfl, H. J. Kreuzer, S. H. Payne, H. Pfnür, M. Scheffler, *First-principles theory of surface thermodynamics and kinetics*, Phys. Rev. Lett. 83, 2993 (1999)

[56] A. van de Walle, G. Ceder, *Automating first-principles phase diagram calculations*, J. Phase Equilib. 23, 348 (2002)

[57] Y. Zhang, V. Blum, K. Reuter, *Accuracy of first-principles lateral interactions: oxygen at Pd(100)*, Phys. Rev. B 75, 235406 (2007)

[58] M. Stöhr, R. Podloucky, S. Müller, *Ab initio phase diagram of oxygen adsorption on W(110)*, J. Phys.: Condens. Matter 21, 134017 (2009)

[59] X. Xu, C. M. Friend, *Partial oxidation without allylic C-H bond activation: The conversion of propene to acetone on Rh(111)-p(2×1)-O*, J. Am. Chem. Soc. 113, 6779 (1991)

[60] T. W. Root, L. D. Schmidt, G. B. Fisher, *Adsorption and reaction of nitric oxide and oxygen on Rh(111)*, Surf. Sci. 134, 30 (1983)

[61] K. D. Gibson, M. Viste, E. C. Sanchez, S. J. Sibener, *High density adsorbed oxygen on Rh(111) and enhanced routes to metallic oxidation using atomic oxygen*, J. Chem. Phys. 110, 2757 (1999)

[62] K. D. Gibson, M. Viste, E. Sanchez, S. J. Sibener, *Physical and chemical properties of high density atomic oxygen overlayers under ultrahigh vacuum conditions: (1×1)-O/Rh(111)*, J. Chem. Phys. 112, 2470 (2000)

[63] K. D. Gibson, J. I. Colonell, S. J. Sibener, *Velocity distributions of recombinatively desorbed* $O_2$ *originating from surface and sub-surface oxygen/Rh(111)*, Surf. Sci. 343, L1151 (1995)

[64] D. Alfè, M. J. Gillan, *Absolute rate of thermal desorption from first-principles simulation*, J. Phys.: Condens. Matter 18, L451 (2006)

[65] D. Alfè, M. J. Gillan, *Ab initio statistical mechanics of surface adsorption and desorption.* $H_2O$ *on MgO(001) at low coverage*, J. Chem. Phys. 127, 114709 (2007)

[66] D. Frenkel, B. Smit, *Understanding Molecular Simulation*, Chapter 7; Academic Press, 2002

[67] Ch. Chipot, A. Pohorille, *Free Energy Calculations*, Chapter 4; Springer, 2007

[68] E. A. Carter, G. Ciccotti, J. T. Hynes, R. Kapral, *Constrained reaction coordinate dynamics for the simulation of rare events*, Chem. Phys. Lett. 156, 472 (1989)

[69] W. K. Den Otter, W. J. Briels, *Free energy from molecular dynamics with multiple constraints*, Mol. Phys. 98, 773 (2000)

[70] E. Darve, M. A. Wilson, A. Pohorille, *Calculating free energies using a scaled-force molecular dynamics algorithm*, Mol. Simul. 28, 113 (2002)

[71] P. Fleurat-Lessard, T. Ziegler, *Tracing the minimum-energy path on the free-energy surface*, J. Chem. Phys. 123, 084101 (2005)

[72] J. P. Ryckaert, G. Ciccotti, H. J. C. Berendsen, *Numerical integration of the Cartesian equations of motion of a system with constraints: molecular dynamics of n-alkanes*, J. Comp. Phys. 23, 327 (1977)

[73] H. C. Andersen, *Molecular dynamics simulations at constant pressure and/or temperature*, J. Chem. Phys. 72, 2384 (1980)

[74] John R. Taylor, *An Introduction to Error Analysis*, 2nd edition, Chapter 3; University Science Books, 1997

[75] M. P. Allen, D. J. Tildesley, *Computer Simulation of Liquids*, Chapter 6; Oxford University Press, 1987

[76] A. Laio, M. Parrinello, *Escaping free-energy minima*, PNAS 99, 12562 (2002)

[77] Ch. Chipot, A. Pohorille, *Free Energy Calculations*, Chapter 2; Springer, 2007

[78] M. E. Tuckerman, *Statistical Mechanics: Theory and Molecular Simulation*, Chapter 8; Oxford University Press, 2010

# List of publications

T. Franz, J. Zabloudil, F. Mittendorfer, L. Gragnaniello, G. Parteder, F. Allegretti, S. Surnev, F. P. Netzer, *Deformed Surface Oxides: Uncommon Structure of a (6×1) NiO Surface Oxide on Rh(111)*, J. Phys. Chem. Lett. 3, 186 (2012),

F. Mittendorfer, T. Franz, J. Klikovits, M. Schmid, L. R. Merte, S. S. Zaman, P. Varga, R. Westerström, A. Resta, J. N. Andersen, J. Gustafson, E. Lundgren, *Oxygen-Stabilized Rh Adatoms: 0D Oxides on a Vicinal Surface*, J. Phys. Chem. Lett. 2, 2747 (2011)

S. Surnev, F. Allegretti, G. Parteder, T. Franz, F. Mittendorfer, J. N. Andersen, F. P. Netzer, *One-Dimensional Oxide-Metal Hybrid Structures: Site-Specific Enhanced Reactivity for CO Oxidation*, ChemPhysChem 11, 2506 (2010)

T. Franz, F. Mittendorfer, *Kinetic Monte Carlo simulations of temperature programed desorption of O/Rh(111), J. Chem. Phys. 132, 194701 (2010).*

# Talks

*Ab-initio free energy calculations for the desorption of oxygen from Rh(111)*, European Conference on Surface Science, August 29 - September 3, 2010, Groningen, Netherlands

*Ab-initio free energy calculations for the desorption of oxygen from Rh(111)*, 10th NFN Workshop ”Nanoscience on Surfaces”, November 14 - November 16, 2010, Stadtschlaining, Austria

*Kinetic Monte Carlo simulations of temperature programmed desorption*, European Conference on Surface Science, August 30 - September 4, 2009, Parma, Italy

*The oxidation of CO on* $NiO_2$*-Rh(553): DFT results*, 8th NFN Workshop ”Nanoscience on Surfaces”, May 10 - May 12, 2009, Seggauberg, Austria

*Kinetic Monte Carlo simulations of temperature programmed desorption*, Spring meeting of the German Physical Society, March 22 - March 27, 2009, Dresden, Germany

*Kinetic Monte Carlo simulations of desorption spectra*, 56th IUVSTA NFN Workshop on Template mediated growth of nanostructures, November 3 - November 6, 2008, Stadtschlaining, Austria

# Poster presentations

*Ab-initio free energy calculations for the desorption of oxygen from Rh(111)*, Psi-k Conference, September 12 - September 16, 2010, Berlin, Germany

*Kinetic Monte Carlo simulations of temperature programmed desorption*, Workshop "Catalysis from first principles", May 25 - May 28, 2009, Vienna, Austria

# Curriculum vitae

## Personal information:

| | |
|---|---|
| Name: | Mag. Thomas Franz |
| Date of birth: | February 20, 1981 |
| Place of birth: | St. Pölten |
| Citizenship: | Austrian |

## Education:

October 2008 - Present:
Doctoral programme in Physics, University of Vienna;
Thesis title: *Dynamic Processes on Rhodium Surfaces*;
Doctoral advisors: Dr. Florian Mittendorfer and Univ.-Prof. Dr. Georg Kresse

October 2002 - April 2008:
Diploma programme in Physics, University of Vienna;
Thesis title: *Kinetische Monte Carlo-Simulation auf Oberflächen*;
Thesis advisors: Dr. Florian Mittendorfer and Univ.-Prof. Dr. Georg Kresse

June 1999:
Matura, BORG St. Pölten